GEOCHEMISTRY OF DEEP-SEA HYDROTHERMAL VENT FLUIDS FROM BROKEN SPUR, RAINBOW AND LOST CITY HYDROTHERMAL VENT FIELDS, MID-ATLANTIC RIDGE

A THESIS SUBMITTED TO
THE INSTITUTE OF MARINE SCIENCES
OF
MIDDLE EAST TECHNICAL UNIVERSITY

BY

SERHAT SEVGEN

IN PARTIAL FULFILLMENT OF THE REQUIREMENTS
FOR
THE DEGREE OF MASTER OF SCIENCE
IN
OCEANOGRAPHY

MAY 2021

Approval of the thesis:

GEOCHEMISTRY OF DEEP-SEA HYDROTHERMAL VENT FLUIDS FROM BROKEN SPUR, RAINBOW AND LOST CITY HYDROTHERMAL VENT FIELDS, MID-ATLANTIC RIDGE

submitted by **SERHAT SEVGEN** in partial fulfillment of the requirements for the degree of **Master of Science** i**n Oceanography, Institute of Marine Sciences, Middle East Technical University** by,

Prof. Dr. Barış Salihoğlu
Director, **Institute of Marine Sciences, METU** _____

Assoc. Dr. Bettina Fach-Salihoğlu
Head of the Department, **Oceanography, METU** _____

Assoc. Prof. Dr. Mustafa Yücel
Supervisor, **Oceanography, METU** _____

Examining Committee Members:

Prof. Dr. Nadine Le Bris
LECOB, Université Pierre et Marie Curie _____

Assoc. Prof. Dr. Mustafa Yücel
Oceanography, METU _____

Assist. Prof. Dr. Koray Özhan
Oceanography, METU _____

Date: 21.05.2021

I hereby declare that all information in this document has been obtained and presented in accordance with academic rules and ethical conduct. I also declare that, as required by these rules and conduct, I have fully cited and referenced all material and results that are not original to this work.

Name Last name : Serhat Sevgen

Signature :

ABSTRACT

GEOCHEMISTRY OF DEEP-SEA HYDROTHERMAL VENT FLUIDS FROM BROKEN SPUR, RAINBOW AND LOST CITY HYDROTHERMAL VENT FIELDS, MID-ATLANTIC RIDGE

Sevgen, Serhat
Master of Science, Oceanography
Supervisor: Assoc. Prof. Dr. Mustafa Yücel

May 2021, 146 pages

Mid- Atlantic Ridge (MAR) is a very special tectonic environment which contains compositioanlly distinct hydrothermal vent fields as a result of its slow spreading character. Considering the increasing efforts on understanding the role of hydrothermal vents in both local and global ocean system, MAR enables to develop a wholistic approach to study formation, evolution and near field transportation of hydrothermal vent products in different vent fields at the same time. Here we present our results obtained from one of each representative vent settings that exists on the MAR (Type 1: Broken Spur, Type 2: Rainbow and Type 3: Lost City) during a research expedition with N/O L'Atalante and ROV Victor 6000 in 2018. ROV-assisted hydrothermal fluid sampling was conducted and samples were taken from the orifice as well as different heights of the hydrothermal plumes of corresponding vents. Upon the sample collection, both on-board and on-shore measurements for major ions, hydrogen sulfide and transition metals were performed by using ion chromatography, colorimetric methods, and ICP-MS. Our results, in support of previous reports for endmember fluid compositions, show that interplay of temperature, pH, Cl and H_2S concentrations control the formation and transportation of dissolved species in Rainbow, Broken Spur and Lost City hydrothermal fluids.

On the other hand, Rainbow and Lost City fields show high temporal stability over ~20 years' time span however substantial changes were observed in Broken Spur fluids in ~25 years, which contrasts with previous findings describing high temporal stability of MAR hydrothermal vents. Considering intense cooling (~100 °C) upon the fluid rise to seafloor in Broken Spur hydrothermal field, we are proposing Broken Spur experiences extensive Si (up to 50%) and Fe precipitation in the subseafloor as Fe-silicate and Fe-sulfide minerals. Furthermore, plume geochemistry results indicate metal oxide and silicate phases are important fraction of Rainbow (nano)particle pool while low Fe:H_2S dynamics in Broken Spur plume result in formation and domination of metal sulfide phases. Considering high removal trends and high correlations observed in metals, silica and cations, we are proposing reverse weathering reactions might be responsible in formation of metal silicate phases especially in Rainbow and possibly in Broken Spur plumes. Finally, our findings in conjunction with previous studies show that hydrothermal vents are factories for biologically important (nano)particles regardless of the setting. Hence, considering the possible global scale effects of such hydrothermal vent products, we are suggesting hydrothermal (nano)particles might have played much more important roles in major geological events in the Earth's history than previously thought.

Keywords: Mid-Atlantic Ridge, Hydrothermal Vents, Rainbow, Broken Spur, Lost City

ÖZ

ORTA ATLANTİK SIRTINDA BULUNAN BROKEN SPUR, RAINBOW VE LOST CITY DERİN DENİZ HİDROTERMAL BACALARININ AKIŞKANLAR JEOKİMYASI

Sevgen, Serhat
Yüksek Lisans, Oşinografi
Tez Yöneticisi: Doç. Dr. Mustafa Yücel

Mayıs 2021, 146 sayfa

Orta Atlantik Sırtı (MAR), yavaş açılım karakterinin bir sonucu olarak kompozisyonel açıdan farklı hidrotermal bacalar içeren çok özel bir tektonik ortamdır. Hem yerel hem de küresel okyanus sistemindeki hidrotermal bacaların rolünü anlamaya yönelik artan çabaları göz önünde bulundurarak, Orta Atlantik Sırtı, hidrotermal baca ürünlerinin oluşumunu, gelişimi ve taşınımını aynı anda farklı alanlarda çalışmak için bütünsel bir yaklaşım sunmaktadır. Burada, 2018 yılında N / O L'Atalante ve ROV Victor 6000 ile yapılan bir araştırma gezisi sırasında MAR'da bulunan her temsili hidrotermal baca örneğinin birinden elde ettiğimiz sonuçları sunuyoruz (Tip 1: Broken Spur, Tip 2: Rainbow ve Tip 3: Lost City). ROV destekli hidrotermal sıvı örneklemesi gerçekleştirilerek ilgili bacaların hidrotermal püskürtülerinin farklı yüksekliklerinden örnekler alındı. Örneklemeyi takiben hem gemide hem de karada iyonların, hidrojen sülfürün ve geçiş metallerinin ölçümleri iyon kromatografisi, kolorimetrik yöntemler ve ICP-MS kullanılarak gerçekleştirildi. Hidrotermal sıvı bileşimleri konusunda önceki raporları destekleyen sonuçlarımız, sıcaklık, pH, Cl ve H_2S konsantrasyonlarının karşılıklı etkileşiminin Rainbow, Broken Spur ve Lost City hidrotermal sıvılarında çözünmüş türlerin oluşumunu ve taşınmasını kontrol ettiğini göstermektedir. Öte yandan, Rainbow ve

Lost City sahaları, ~20 yıllık bir zaman diliminde yüksek zamansal kararlılık sergilerken Broken Spur sıvılarında, MAR hidrotermal bacalarının yüksek zamansal kararlılığını tanımlayan önceki bulgulara aykırı olarak, ~25 yıl içinde önemli değişiklikler gözlenmiştir. Broken Spur alanında hidrotermal sıvıların derinlerden deniz tabanına taşınması sırasında meydana gelen yoğun sıcaklık kaybını (~100 ° C) göz önünde bulundurarak, bu alanda deniz tabanının altında aşırı miktarda silika (50% kadar) ve demirin Fe-silikat ve Fe-sülfit mineralleri olarak çökeldiğini öngörüyoruz. Ayrıca, püskürtü jeokimyası sonuçları, metal oksit ve silikat fazlarının Rainbow (nano)parçacık havuzunun önemli bir parçası olduğunu, Broken Spur sistemindeki düşük Fe:H_2S dinamiklerinin ise metal sülfit fazlarının oluşumuna ve hakimiyetine neden olduğunu göstermektedir. Metal, silika ve katyon konsantrasyonlarında gözlemlenen azalım eğilimleri ve yüksek korelasyonlar göz önüne alındığında, özellikle Rainbow ve muhtemelen Broken Spur püskürtülerinde metal silikat fazlarının oluşumunda "reverse weathering" reaksiyonlarının sorumlu olabileceğini öneriyoruz. Son olarak, önceki çalışmalarla bağlantılı olarak bulgularımız, hidrotermal bacaların, ortam ne olursa olsun biyolojik olarak önemli (nano)parçacık fabrikaları olduğunu göstermektedir. Bu nedenle, bu tür hidrotermal baca ürünlerinin olası küresel ölçekli etkilerini göz önünde bulundurarak, hidrotermal (nano)parçacıkların Dünya tarihindeki önemli jeolojik olaylarda daha önce düşünülenden çok daha önemli roller oynamış olabileceğini öne sürüyoruz.

Anahtar Kelimeler: Orta Atlantik Sırtı, Hidrotermal Bacalar, Rainbow, Broken Spur, Lost City

‘To infinity and beyond!’ Buzz Lightyear

ACKNOWLEDGMENTS

I am deeply thankful to my supervisor Assoc. Prof. Dr. Mustafa Yücel for his valuable guidance, support and patience throughout this study.

I am also thankful to Prof. Dr. Nadine Le Bris for providing me the cruise opportunity in 2018 and all the supports during and after the cruise.

I also thank to Xavier Placaud, Dr. Ashley Grosche, Dr. Marica Mezzelani and Dr. Francesco Smedile, without their continued support and friendship, the research expedition would not be this efficient and enjoyable for me.

I also thank to Şehmuz Başduvar and Pınar Kalegeri for assisting with ICP-MS and ion chromatography measurements.

I would like to thank also to Dr. Sanjoy Som for contributing greatly to my development as a good person and scientist with his mentorship, friendship, and guidance.

I am also deeply thankful to all LUNATICS, Ellen Costa-Almeida, Fatima Li-Hau, Paula Prondzinsky and Alexandra Zetterlind for providing me great motivation with their friendship and support in completing this thesis.

I would like to thank to my friends Nimet Alımlı, İsmail Akçay, Berfin Dağ and Murat Aru, without their friendship and support, this thesis would not be completed.

I am also thankful to Büşra Çelikbaş, this thesis is a product of a dream we had many years ago.

Last but not least, I am deeply grateful to my family, Ömrüye, Raif, Sıla, Hava, Orion the Flying Cat and rest of my family, without their continued encouragement and support, I would not reach the place where I am today.

The TRANSECT cruise was funded by the French Oceanographic Fleet and CNRS-INEE to LECOB. I would like to thank to Master and crew of the R/V L'Atalante and team of ROV Victor 6000 for a very successful cruise. I also acknowledge DEKOSIM project of METU-IMS, Mustafa Yücel's Turkish Academy of Sciences, Young Investigator Grant (TÜBA-GEBIP) as well as The Science Academy-BAGEP award which supported traveling and enabling to complete the analyses of this work.

TABLE OF CONTENTS

ABSTRACT v

ÖZ vii

ACKNOWLEDGMENTS x

TABLE OF CONTENTS xii

LIST OF TABLES xiv

LIST OF FIGURES xv

1 INTRODUCTION 1

1.1 History of Hydrothermal Vent Research 2

1.2 Formation and Evolution of Hydrothermal Vent Fluids 4

1.2.1 Mid-Ocean Ridge Morphology and Spreading Rate 5

1.2.2 Subseafloor Water/Rock Reactions and Phase Separation 7

1.2.3 Hydrothermal Plume Processes 12

1.3 General Characteristics of Slow Spreading Mid-Atlantic Ridge System 16

1.4 Study Sites: Broken Spur, Rainbow and Lost City Vent Fields 19

1.5 Aims of This Study 26

2 MATERIALS AND METHODS 29

2.1 Sample Collection 29

2.2 Colorimetric Iron and Hydrogen Sulfide Measurements 32

2.3 Analytical Methods for Major Ions and Metals 33

2.4 Calculation of Endmember Fluid Compositions 34

2.5 Generation of Mixing Lines for Hydrothermal Plumes 35

3 RESULTS 37

3.1 General Observations 37

3.2 End-member Fluid Geochemistry 39
3.2.1 Temperature and pH 39
3.2.2 Mg and SO_4 40
3.2.3 Other Non-Volatile Dissolved Species 44
3.2.3.1 Rainbow Hydrothermal Vent Field 44
3.2.3.2 Broken Spur Hydrothermal Vent Field 48
3.2.3.3 Lost City Hydrothermal Vent Field 51
3.2.4 Transition Metals and $\sum H_2S$ 52
3.3 Geochemistry of Rainbow and Broken Spur Hydrothermal Plumes 56
4 DISCUSSION 67
4.1 Processes Controlling Formation of Endmember Fluid Geochemistry 67
4.1.1 Phase separation and Cl variability 67
4.1.2 Geochemical Evolution of Other Non-Volatile Dissolved Species 71
4.1.3 Lithium Concentration and Water/Rock Ratios 79
4.1.4 Effects of Fluid/Rock Reactions on Metal Mobility and H_2S Composition 83
4.2 Spatial and Temporal Variations of Broken Spur, Rainbow and Lost City Fluids 88
4.3 Factors Controlling the Near-Field Export of Vent Products in the Rainbow and Broken Spur Rising Plumes 94
4.4 Possible Major Implications of Hydrothermal Vent Products in Major Geological Events in the Earth's History 107
4.4.1 Last Glacial Maximum (LGM) 108
4.4.2 The Cenomanian- Turonian Anoxic Event 110
5 CONCLUSION 113
REFERENCEs 117

LIST OF TABLES

TABLES

Table 2.1 Coordinates and depths of visited individual vents in Rainbow, Broken Spur and Lost City hydrothermal fields 30

Table 3.1 Table representing maximum temperature measured at the vent orifice, minimum pH at 25 °C, 1 atm, measured minimum Mg concentrations and sampling procedure in different heights from the orifice for individual vents fluids in Rainbow, Broken Spur and Lost City hydrothermal fields (FTD: Fumeur Tres Dense; FN: Fumeur Nouveau) 40

Table 3.2 Measured concentrations of dissolved species for Rainbow, Broken Spur and Lost City hydrothermal vent fluids (FTD: Fumeur Tres Dense; FN: Fumeur Nouveau) 42

Table 3.3 Calculated endmember compositions for Rainbow, Broken Spur and Lost City hydrothermal vent fluids 47

Table 3.4 Cl normalized elemental ratios calculated from endmember fluid composition at Rainbow, Broken Spur and Lost City hydrothermal fields. Indicated units are as follows mM: mmol/kg and μM: μmol/kg 50

Table 3.5 Calculated endmember compositions of Fe, Mn, Si and H_2S for Rainbow, Broken Spur and Lost City hydrothermal vent fluids 52

Table 3.6 Table showing standart error values of slope and Y-intercepts for each endmember chemical species obtained by using regression plots in Figure 3.2 and Figure 3.3 for Rainbow (Fumeur Tres Dense, Fumeur Nouveau, Magali), Broken Spur (Spire, Dragon, Chandelier) and Lost City (Marker B) vent fluids (units are same as the regression plots) 55

Table 4.1 Correlation matrix representing R^2 values for some non-volatile dissolved species in Rainbow and Broken Spur hydrothermal plumes (FTD: Fumeur Tres Dense and FN: Fumeur Nouveau) 99

LIST OF FIGURES

FIGURES

Figure 1.1. World map showing hydrothermal vent fields discovered to date (Beaulieu et al., 2020). Red dots show confirmed vent areas while yellow dots represent inferred vent areas 3
Figure 1.2. Profiles of EPR 3º S (fast spreading ridge), EPR 21º N (intermediate spreading ridge) and MAR 37º N (slow spreading ridge) (Kelley et al., 2002). Magmatic activity is decreasing and faulting intensity is increasing toward slow spreading MAR 6
Figure 1.3. General schematic view of hydrothermal vent fluid formation and evolution in the subseafloor (Tivey, 2007) 8
Figure 1.4. Phase separation diagram in the given temperature and pressure conditions (German and Von Damm, 2003). CP indicates critical point of seawater (407 °C and 298 bars) 9
Figure 1.5. Schematic view of hydrothermal plume development (Credit: NOAA) 13
Figure 1.6. Bar chart showing Fe^{2+} oxidation half-lives in background deep seawater conditions for different basins and there is a solid decreasing trend in Fe^{2+} oxidation rate from Atlantic (e.g. MAR: TAG, Rainbow) to Pacific (e.g. Juan de Fuca Ridge) settings (Field and Sherrell, 2000) 15
Figure 1.7. Zonal concentration plot of Fe shows that hydrothermal iron was traced 4300 kilometers along Eastern Pacific transect (Resing et al., 2015)..... 16
Figure 1.8. Diagram showing mode of formation of three main types of vent field present in slow spreading Mid-Atlantic Ridge system (Kelley and Shank, 2010) . 17
Figure 1.9. Map showing some of the active vent locations up to date in the North Atlantic Ocean. Visited hydrothermal vent fields in this study is marked in red. Map courtesy of http://www.geomapapp.org..... 19
Figure 1.10. A sketch showing general distribution of vents and fractures in Broken Spur vent field (Murton et al., 1995) 20

Figure 1.11. Map showing location of Rainbow hydrothermal vent field on a nonvolcanic ridge between the South AMAR and AMAR segments in Mid-Atlantic Ridge (Charlou et al., 2010) 21
Figure 1.12. Geological map of Rainbow massif. Colors are representing exposures of different geological materials. White star indicates active Rainbow hydrothermal vent field (Eason et al., 2016)..... 22
Figure 1.13. Bathymetric map of Atlantis Massif (Kelley et al., 2007) 24
Figure 1.14. Geological map of Atlantis massif and Lost City hydrothermal vent field. Colors are representing exposure of different geological materials including serpentinite, gabbro and carbonates (see Denny et al., 2015 for further details) 25
Figure 2.1. (A) N/O L'Atalante, (B) ROV Victor 6000, (C) Titanium syringes (major samplers) for high temperature fluid sampling (Credit: IFREMER) 29
Figure 2.2. (A) Underwater hydrothermal fluid sampling with titanium samplers and (B) temperature measurements with high temperature probe (Credit: Mission TRANSECT/ Le Bris et al. (2018))..... 31
Figure 3.1. Representative field images of Broken Spur (A), Rainbow (B) and Lost City (C) hydrothermal vents (Credit: Mission TRANSECT/ Le Bris et al. (2018))38
Figure 3.2. Measured Mg versus SO_4 (A), Na (B), Li (C), Cl (D), K (E), Br (F), Ca (G) for all high temperature fluid samples from Rainbow, Broken Spur and Lost City vent fields. Endmember concentrations are calculated by using least-squares regression method. Endmember concentrations are represented as solid lines. Black filled symbols are for Rainbow, open symbols are for Broken Spur and half filled symbol is for Lost City 45
Figure 3.3. Measured Mg versus Fe (A, B), $\sum H_2S$ (C), Mn (D), Si (E, F) plots for all high temperature fluid samples where appropriate from Rainbow, Broken Spur and Lost City vent fields. Endmember concentrations are calculated by using least-squares regression method and represented as solid lines. Black filled symbols are for Rainbow (Circle: Fumeur Tres Dense, Square: Fumeur Nouveau, Triangle: Magali), open symbols are for Broken Spur (Inverted Triangle: Spire, Diamond: Dragon, Circle: Chandelier) and half-filled square is for Marker B, Lost City 54

Figure 3.4. Evolution of temperature, Mg, Fe, Mn, Si, Al, Br, Cd, K, Ca, SO_4, Li, Cu, Zn, Ni, and Co in Magali rising plume, Rainbow hydrothermal vent field. Vertical axes represent distance from the orifice in meter..... 58
Figure 3.5. Evolution of temperature, Mg, Fe, Mn, Si, Al, Br, Cd, K, Ca, SO_4, Li, Cu, Zn, Ni, and Co in Fumeur Nouveau rising plume, Rainbow hydrothermal vent field. Vertical axes represent distance from the orifice in meter 59
Figure 3.6. Evolution of temperature, Mg, Fe, Mn, Si, Al, Br, Cd, K, Ca, SO_4, Li, Cu, Zn, Ni, and Co in Fumeur Tres Dense rising plume, Rainbow hydrothermal vent field. Vertical axes represent distance from the orifice in meter 60
Figure 3.7. Evolution of temperature, Mg, Fe, Mn, Si, Al, Br, Cd, K, Ca, SO_4, Li, Cu, Zn, Ni, and Co in Spire rising plume, Broken Spur hydrothermal vent field. Vertical axes represent distance from the orifice in meter..... 61
Figure 3.8. Evolution of Mg, Fe, Mn, Si, Al, Br, Cd, K, Ca, SO_4, Li, Cu, Zn, Ni, and Co in Chandelier rising plume, Broken Spur hydrothermal vent field. Vertical axes represent distance from the orifice in meter..... 62
Figure 3.9. Evolution of Mg, Fe, Mn, Si, Al, Br, Cd, K, Ca, SO_4, Li, Cu, Zn, Ni, and Co in Dragon rising plume, Broken Spur hydrothermal vent field. Vertical axes represent distance from the orifice in meter..... 63
Figure 4.1. Temperature and Pressure properties of seawater with two-phase curve (solid line) (from Bischoff and Rosenbauer, 1985). CP indicates critical point of seawater at 407 °C and 298 bars. Seafloor P-T conditions for each individual Rainbow and Broken Spur vents are represented in the plot as well..... 68
Figure 4.2. Isotherms of the vapor-liquid region and two-phase curve (red) of NaCl-H_2O from 390 °C to 475°C (modified from Bischoff and Pitzer (1989)). CP indicates critical point of 3.2 wt % seawater at 298 bars. Individual vent fields in Rainbow and Broken Spur are represented in the plot as well..... 69
Figure 4.3. High positive correlation between Mg and SO_4 for samples from each individual vent in Rainbow, Broken Spur and Lost City hydrothermal fields. Statistical parameters are represented on the plot..... 71

Figure 4.4. Cl versus Ca (A), K (B), Li (C), K/Cl (D), Na/Cl (E), Ca/Cl (G), Fe (I), Mn (K), H_2S (L); Na/Cl versus Ca/Cl (F), K/Na (H); pH versus Temperature (J) for different vent fields around world's oceans. Rainbow, Broken Spur and Lost City hydrothermal fields are indicated in each plot. Rainbow and Logatchev are ultramafic hosted systems in MAR. Vent fluid geochemistry database are used from Diehl and Bach (2020). (Right y-axes are for Okinawa vents when appropriate) ..75
Figure 4.5. Plot of dissolved SiO_2 concentration as a function of temperature and pressure (Von Damm et al., 1991). Pressure values are as noted on the plot and increases incrementally between 150- 1000 bar. Broken Spur vent fluids (inverted triangle: Spire; diamond: Dragon) are indicated on the plot. Star denotes inferred Broken Spur silica concentration based on subsurface phase separation conditions 78
Figure 4.6. Negative correlation between pH and endmember Fe concentrations for both Rainbow (left y-axis) and Broken Spur (right y-axis) hydrothermal fluids. R-squared and p-value for Rainbow are calculated as 0.98 and <0.0001, respectively while R-squared is 0.64 and p-value is 0.0055 for Broken Spur fluids.....84
Figure 4.7. Temporal variations of Broken Spur (A), Rainbow (B) and Lost City (C) hydrothermal fields. Y-axes representing concentrations in mmol/kg and temperature in °C. Values have been multiplied as noted on the plot to have a plotting with a single y-axis. (Broken Spur: James et al. (1995); Rainbow: Douville et al. (2002); Seyfried et al. (2011); Lost City: Kelley et al. (2001); Seyfried et al. (2015)) 90
Figure 4.8. Spatial variations of different geochemical species in Broken Spur (A, B) and Rainbow (C, D) hydrothermal vent fields. Y-axes representing concentrations in mmol/kg. Values have been multiplied as noted on the plot to have a plotting with a single y-axis.....91
Figure 4.9. Nanoparticle iron (cFe-N) profiles for Magali (A), Fumeur Nouveau (B) and Fumeur Tres Dense (C) plumes in Rainbow and Spire (D), Chandelier (E) and Dragon (F) plumes in Broken Spur (regenerated from Yucel et al. (2021)) 95

Figure 4.10. Relationship between measured concentration of Fe, Ca, Si, K, Li, Al and Mn in Rainbow hydrothermal plume (Green: Magali; Blue: Fumeur Tres Dense; Orange: Fumeur Nouveau; Triangle: Fe; Circle: Si; Square: Mn)..... 97
Figure 4.11. Relationship between measured concentration of Fe, Ca, Si, K, Li, Al and Mn in Broken Spur hydrothermal plume (Green: Dragon; Blue: Spire; Orange: Chandelier; Triangle: Fe; Circle: Si; Square: Mn)..... 98
Figure 4.12. Removal plots for Rainbow hydrothermal plume. For each species, the range in extrapolated zero-Mg high temperature endmember composition is shown with the red bar, and the average is shown with a black line projected from seawater composition. Species that exhibit conservative behavior during mixing plot on the line while species that behave non-conservatively plot above or below the line . 104
Figure 4.13. Removal plots for Broken Spur plume. For each species, the range in extrapolated zero-Mg high temperature endmember composition is shown with the red bar, and the average is shown with a black line projected from seawater composition. Species that exhibit conservative behavior during mixing plot on the line while species that behave non-conservatively plot above or below the line . 105
Figure 4.14. Hydrothermal iron flux change across the last glacial maximum (for further details check Costa et al. (2017) and references therein)..... 109
Figure 4.15. Paleogeographic map of Earth ~90 million years ago. Areas representing anoxic conditions were indicated in shaded gray color (Sinton and Duncan, 1997)..... 111

CHAPTER 1

INTRODUCTION

Hydrothermal vents mainly form due to circulation of seawater in the subseafloor along tectonically and magmaticaly active places (e.g. convergent and divergent plate boundaries etc.) in the world's oceans. They are important actors in deep-sea environments and their fluid compositions can be used as tracers to understand ocean floor crustal processes. In other words, hydrothermal vent fluids is one of the most well establish tool to obtain geo-bio-chemical information about subseafloor processes by considering the difficulties in obtaining data from subsurface (i.e. several km below the ocean floor) with other methods (German and Von Damm, 2003). For example, depth of fluid circulation and heat source can directly be obtained by using the vent fluid composition since certain geochemical indicators provide an integrated record for temperature and pressure conditions of the subsurface (e.g. Bischoff and Pitzer, 1989; Von Damm et al., 1991; Charlou et al., 2002; Gallant and Von Damm, 2006; Charlou et al., 2010). Beyond that, hydrothermal vent fluids may cause formation of economically important mineral deposits. These deposits provide valuable information on how redox reactions control transportation of metals in the hydrothermal fluids (e.g. Tivey, 2007). Additionally, hydrothermal deposits and sediments are natural archives and can be used to understand the dynamics of ancient hydrothermal activities and their possible major implications in the Earth's history (e.g. Lund et al, 2016; Middleton et al, 2016; Costa et al, 2017). Hydrothermal activity and vent fluid compositions can also provide some insights on biological activities in the subseafloor and near vent environments by considering the amount of biomass flourishing in these environments (e.g. Le Bris et al., 2019).

Furthermore, different studies (e.g. Resing et al., 2015; Fitzsimmons et al., 2017; Ardyna et al., 2019) indicated that hydrothermal vents are not only local actors in deep-sea environments but also their products are an important part of the global ocean biogeochemical system. However, still an integrative understanding of different mechanisms controlling hydrothermal vent fluid formation and evolution is needed with further studies to emplace hydrothermal vents into a correct location in global ocean system. Therefore, discoveries of new vent sites and examining temporal and spatial variations of geochemical composition of hydrothermal vent fluids are crucial.

In that respect, this thesis is planned to focus hydrothermal vents in Mid- Atlantic Ridge (MAR) system since MAR contains the most diversified hydrothermal vents in close proximities due to its slow spreading character. Within the objectives of this thesis, geochemical characteristics of hydrothermal fluids from geologically diversed Broken Spur, Rainbow and Lost City hydrothermal vent fields are examined by considering both their subsurface water-rock reaction stage and hydrothermal plume development stage. It was aimed to develop an up to date dataset for these corresponding vent fields and understand their spatial and temporal variations in time by comparing existing knowledge from the literature. Below, I first introduce historical background in hydrothermal vent research, main mechanisms controlling hydrothermal fluid formation and evolution, characteristics of slow spreading MAR environment and description of study sites. In the following chapters, methodology of sample collection and processing, measurement results and accordingly a comprehensive discussion are presented.

1.1 History of Hydrothermal Vent Research

One of the first evidences on the presence of hydrothermal venting received in the 1960s after the investigation of hot (40-60 °C), salty water and metal rich sediments on the Red Sea ocean basin (Bischoff, 1969). Since the Red Sea is a place where

active tectonic rifting occurs between African and Arabian plates, it represents a very good example of young divergent plate boundary. Therefore, it was thought that similar set of geochemical features might be present in other mid-ocean spreading centers in the world's oceans as well. Indeed, analysis on sediment core samples by Bostrom et al. (1969) showed that global ridge crest is dominated by metalliferous sediments. Additionally, detection of ^{3}He anomalies in Pacific Ocean basin used as a supporting evidence for presence of hydrothermal activity since the only source for ^{3}He present in the ocean water column was thought to be earth's interior, hence hydrothermalism (Clarke et al., 1969). Then, the problems encountering in balancing heat budget of the Earth arose after the plate tectonic theory and seafloor spreading had started to take credits by scientific community in the years 1960-70's and convective processes in the oceanic crust, i.e. circulation of seawater with gradual temperature increase and its release into seafloor, was considered to be a good way to balance the heat budget of the Earth system.

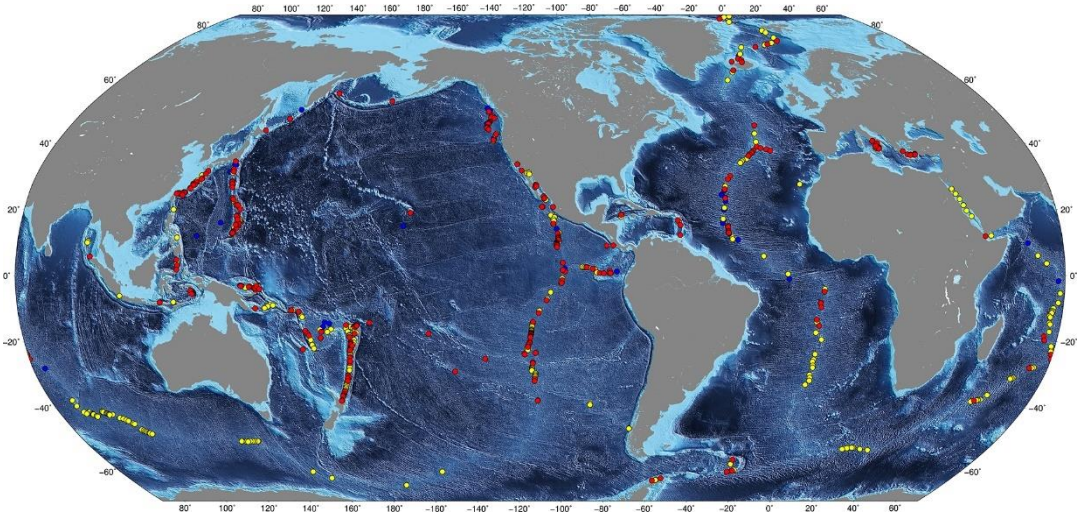

Figure 1.1. World map showing hydrothermal vent fields discovered to date (Beaulieu et al., 2020). Red dots show confirmed vent areas while yellow dots represent inferred vent areas

In the lights of all these progressions, in 1977, the first hydrothermal vent discharging geochemically modified fluids with elevated temperatures (~17 °C) compared to seawater was discovered along the Galapagos spreading center in the

Eastern Equatorial Pacific Ocean during a research expedition with DSV Alvin (Corliss et al., 1979). These fluids had very cooler temperature than previously assumed and there should be hydrothermal fluids with temperatures as high as 350 °C as Edmonds et al. (1979) predicted. It was not too long to take to discover the first "black smoker" type high temperature hydrothermal venting, and hydrothermal fluids having temperatures 380±30 °C was reported at 21 °N East Pacific Rise (EPR) within two years after the first discovery (Ballard and Grassle, 1979).

Since that time, new hydrothermal vent fields have been discovered in all ocean basins including the Pacific, Atlantic, Indian, Artic and Southern Oceans (Rona et al., 1986; Campbell et al. 1988; Murton et al., 1994; Fouquet et al., 1997; German et al., 1998; German et al., 2000; Kelley et al., 2001; Klinkhammer et al., 2001; Baker and German, 2004; Baker et al., 2006; German et al., 2010; Pedersen et al., 2010; Rogers et al., 2012; Tao et al., 2012) (Figure 1.1). Despite of their widespread appearance, a very small number of hydrothermal vent locations have been known today considering the size of the ocean basins, however, with the new advancements in deep-sea technologies such as autonomous underwater vehicles (AUVs), remotely operated vehicles (ROVs), and research submersibles, and with increased interest and efforts to deep-sea researches, new vents sites will continue to be discovered.

1.2 Formation and Evolution of Hydrothermal Vent Fluids

During the hydrothermal fluid circulation down through oceanic crust, seawater first gets heated and its initial chemical composition starts to change due to reactions with surrounding rocks. After reaching an appropriate reaction temperature, buoyancy of modified seawater increases and it starts to rise rapidly back to seafloor by channelizing through main fractures. Then, hot (350-400 °C), buoyant and chemically modified hydrothermal fluids releases into cold (2-4°C) and denser deep-water column and forming hydrothermal vents. Both depletions and enrichments of different elements occur relative to initial seawater composition throughout all these processes, and examining main mechanisms of hydrothermal fluid generation is

crucial to understand the ultimate fate of hydrothermal products. The factors controlling fluid formation and evolution can mainly be summarized as (1) mid-ocean ridge morphology and spreading rate, (2) subseafloor water/rock reactions and phase separation, and (3) hydrothermal plume processes.

1.2.1 Mid-Ocean Ridge Morphology and Spreading Rate

Interplay of tectonic and magmatic processes in mid-ocean ridge systems have major controls on formation and evolution of hydrothermal vent fields. Mid-ocean ridge morphology is shaped under these forces and they have direct relationship with the spreading rate of the system (Macdonald, 1982; Kelley et al., 2002; Karson, 2002). Spreading rate is a geological phenomenon defining how fast plates are separating with respect to each other. Different mid-ocean ridge systems can be divided into different groups according to their spreading rates and fast, intermediate and slow spreading ridges can be considered as fundamental types as they are the most common and studied ridge systems in the world. Spreading rate of the mid-ocean ridge systems and resultant ridge morphologies directly affect geochemical reactions that produce hydrothermal fluids since age of the system, depth, size and shape of the heat source, distributions of fractures and fissures in the crust, and composition of the surrounding rocks as a reaction medium determine the temperature and pressure conditions where water-rock reactions and phase separation occur in the subsurface (Tivey, 2007; German and Von Damm, 2003). For example, fast spreading East Pacific Rise (EPR) 9^{o}50’ N has an average spreading rate of 11 cm/ year (Carbotte and Macdonald, 1992). Sinton and Detrick (1992) indicated that a continuous magma supply by a large magmatic body dominates the EPR system. Also, ridge axis is lack of a large rift valley and intense faulting. In addition, due to intense magmatic activity, ridge axis is dominated mostly by basaltic rocks (Figure 1.2). Interaction of seawater with basaltic rocks all over the ridge axis generally produces high temperature (>300 ^{o}C), low pH, anoxic hydrothermal fluids containing variable concentrations of hydrogen sulfide and metals. In addition to

that, due to the intense magmatic activity, magmatic eruption cycle of the system is very short. That is, the first documented eruption happened in EPR 9º50' N in 1991/ 1992 (Haymon et al., 1993; Rubin et al., 1994) and just within ~15 years in the late 2005/early 2006 second eruption was detected (Tolstoy et al., 2006). Besides the fast spreading ridges, Mid-Atlantic Ridge system (MAR) is the best example of slow spreading ridge in the world. Its spreading rate is approximately 3 cm/year in average.

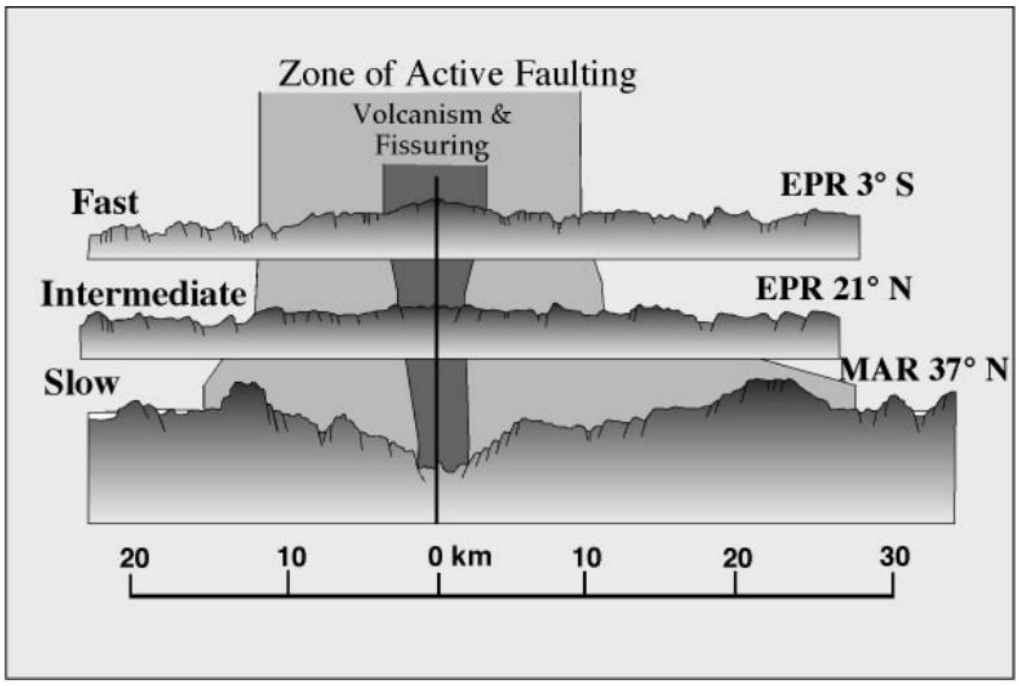

Figure 1.2. Profiles of EPR 3º S (fast spreading ridge), EPR 21º N (intermediate spreading ridge) and MAR 37º N (slow spreading ridge) (Kelley et al., 2002). Magmatic activity is decreasing and faulting intensity is increasing toward slow spreading MAR

Unlike EPR 9º50'N, there occur less emplacement of magma beneath the ridge axis in MAR and therefore magmatic body cannot provide a melt supply as intense and continuous as the one in fast spreading ridges (Kelley et al., 2002). Due to high tectonic activity and less magmatic supply, ridge axis is divided by deep crustal faults and characterized by a large tectonic valley (Figure 1.2). Karson (2002) indicated that system is cut by large amount of discontinuities and therefore different types of

host rocks (e.g. basalt, gabbro, peridotite) can be transported through these faults along the Mid-Atlantic Ridge (e.g. Kelley and Shank, 2010). This local variability makes MAR the most diversified ridge system in the world and as a result, compositionally different hydrothermal vent fields (from acidic to alkaline, metal-rich to metal-free, volatile rich to poor) can be present in close proximities (Kelley and Shanks, 2010). In addition, MAR is very steady system, that is, there is very long eruption cycles unlike EPR, which makes composition of the fluids stable over time (Charlou et al., 2010; Seyfried et al., 2011; Koschinsky et al., 2020). Finally, intermediate spreading ridges are another important type of mid-ocean ridge and understanding processes happening there is crucial because they exhibit transitional features between two other fundamental ridge types, fast and slow spreading ridges (Figure 1.2). East Pacific Rise 21 ^{o}N (EPR) and Juan de Fuca Ridge are the main examples of intermediate spreading ridges in the world and their spreading rate is 6 cm/year in average.

1.2.2 Subseafloor Water/Rock Reactions and Phase Separation

It is possible to divide the subseafloor into three main zones where different geochemical reactions occur during the hydrothermal fluid circulation. The first zone is "recharge" zone, where initial seawater starts to seep down into ocean crust and relatively low temperature reactions start to take place as a result of progressive heating (Alt, 1995). As the temperature of seawater reaches ~150 °C, seawater losses its Mg content with precipitation of Mg into clay minerals such as chlorite ($Mg_5Al_2Si_3O_{10}(OH)_8$) and Mg-rich smectite (Alt, 1995) (Figure 1.3). pH of the seawater starts to decrease as well and evolving fluid becomes more acidic as Mg fixation forms H^+ ions as described in Reaction 1 (Tivey, 2007).

$$4(NaSi)_{0.5}(CaAl)_{0.5}AlSi_2O_8 + 15Mg^{2+} + 24H_2O \Rightarrow \quad \text{(Reaction 1)}$$

$$3Mg_5Al_2Si_3O_{10}(OH)_8 + SiO_2 + 2Na^+ + 2Ca^{2+} + 24H^+$$

Likewise, significant amount of Ca is also removed from the seawater and precipitate as anhydrite ($CaSO_4$) after exceeding ~150 °C since anhydrite has retrograde solubility (Figure 1.3) (Bischoff and Seyfried, 1978). The precipitation of anhydrite removes all of the Ca content of the seawater but it only removes approximately 33% of the sulfate in seawater. It is important to notice that most of the endmember hydrothermal fluids have at least a couple of micromolar level Ca in their composition (see German and Von Damm, 2003) although Ca was highly depleted in anhydrite formation. Therefore, another process acts as a Ca source should be account.

$$CaAl_2Si_2O_8 + 2Na^+ + 4SiO_2\,(aq) \Rightarrow 2NaAlSi_3O_8 + Ca^{2+} \qquad \text{(Reaction 2)}$$

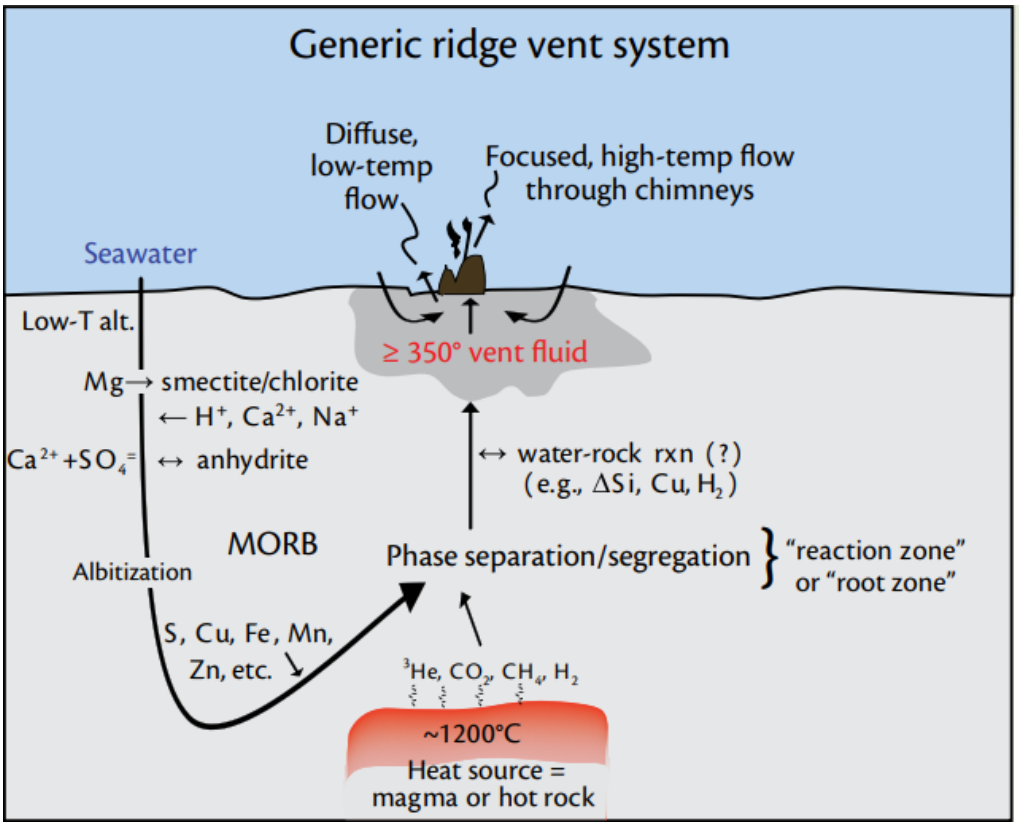

Figure 1.3. General schematic view of hydrothermal vent fluid formation and evolution in the subseafloor (Tivey, 2007)

Albitization is one of the primary reactions explaining the source of excess Ca in hydrothermal fluids. In albitization, alteration of anorthite ($CaAl_2Si_2O_8$) to albite

($NaAlSi_3O_8$) result in substitution of Ca in anorthite with Na and affect their concentrations in hydrothermal fluids as described in Reaction 2 (Berndt and Seyfried, 1993; Alt, 1995; Tivey, 2007). Additionally, in recharge zone, modified seawater starts to obtain a reducing character due to the reactions of water with Fe-bearing minerals such as pyroxene, olivine and pyrrhotite (Figure 1.3). Reducing conditions further cause reduction of remaining seawater sulfate into sulfide (Alt, 1995).

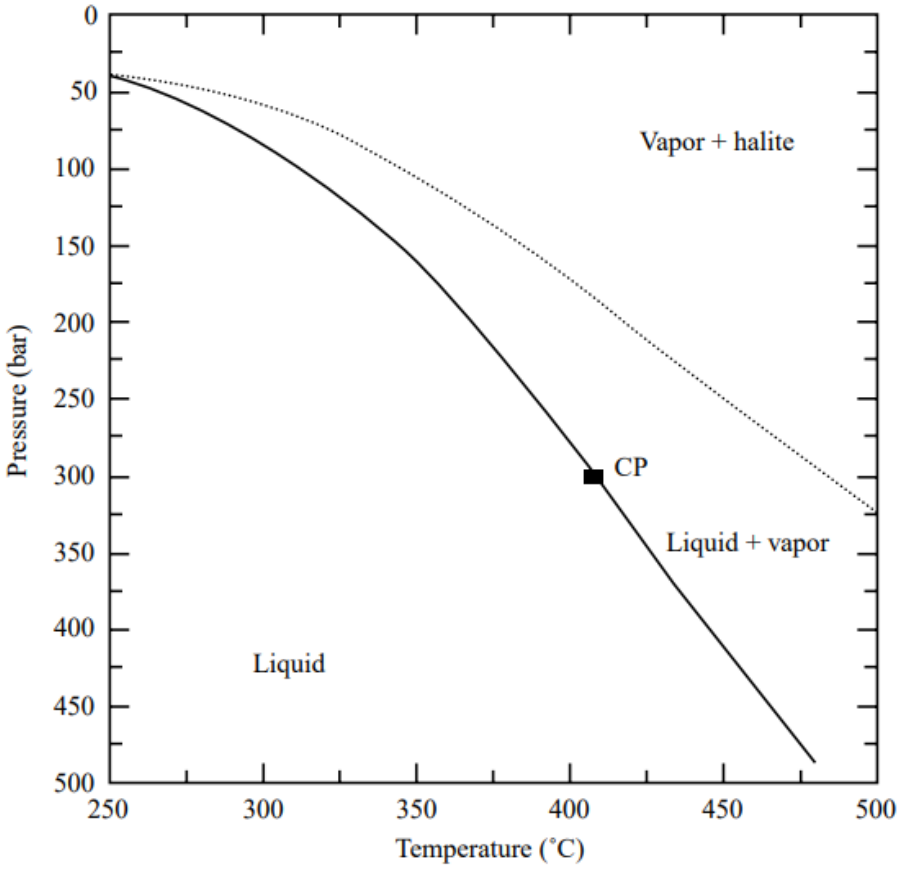

Figure 1.4. Phase separation diagram in the given temperature and pressure conditions (German and Von Damm, 2003). CP indicates critical point of seawater (407 °C and 298 bars)

The second zone is generally known as “reaction” zone (Alt, 1995) where high temperature and pressure conditions (~425°C and ~400 to 500 bars) lead most of the reactions to happen since kinetics of reactions are faster at higher temperatures (e.g.

Pester et al., 2011). In this zone, hydrothermal fluids start to leach metals such as Fe, Mn, Zn, and Cu from the rock (Figure 1.3).

During the fluid circulation in that zone, magmatic volatiles such as ^{3}He, CH_4, CO_2, and H_2 can also be obtained by the hydrothermal fluid due to magmatic interaction and degassing (Alt, 1995). One of the most important reactions in this zone is phase separation (Figure 1.3). The hydrothermal fluid can separate into two different phases mainly as high salinity brine and low-salinity vapor phases as a result of phase separation if the fluid temperature and pressure conditions sufficient enough with respect to critical point of seawater (407 °C and 298 bar) (Figure 1.4) (e.g. Bischoff and Rosenbauer, 1985; German and Von Damm, 2003; Foustoukos and Seyfried, 2007). Phase separation affects the concentration of Cl in hydrothermal fluids. That is, hydrothermal fluids exhibit both enrichments and depletions of Cl concentration with respect to seawater and Cl is quite a conservative element through water-rock reactions however its concentration can mainly change with phase separation. Cl becomes the major anion in the hydrothermal fluids considering depletion of sulfate and titration of carbonate phases due to increasing acidity (Tivey, 2007). Therefore, almost all cations are incorporated with Cl and can be transported as chloro-complexes in hydrothermal fluids, and major changes in Cl concentration affect the endmember concentration of most metals in the hydrothermal fluids (Von Damm, 1990). Additionally, different chemical phases show different partitioning tendency between these two phases generated by phase separation. For example, most of the gases such as H_2S, CO_2, He, CH_4, H_2 partition into vapor phase while ions tend to partition into brine phase (Von Damm, 1995). That is why state of phase separation is very crucial as a determining factor for evolution of hydrothermal fluids.

In the third zone, which is known as “up-flow” zone (Alt, 1995), high temperature hydrothermal fluids modified by all these reactions are very buoyant and rapidly rise to seafloor (Figure 1.3). Because of upward rise of the fluid, pressure and temperature starts to decrease and initiate cooling. Cooling can be either conductive cooling where heat loss to surrounding rocks or adiabatic cooling due to decompression. During the up-flow, hydrothermal fluids can meet and mix with

seawater and/or other modified hydrothermal fluids. This mixing process might rapidly change physicochemical conditions of the hydrothermal fluids and might initiate precipitation of different phases. For example, metals including copper, zinc and iron precipitate to form metal sulfides and these minerals are deposited rapidly and forming the hydrothermal chimneys and vent mineral deposits (Tivey, 2007). Also, recent studies showed that this zone can act as a factory for nanometric size mineral and particle formation. High rates in particle nucleation with respect to particle growth in that zone can favor formation of nanoparticle size kinetically stable metal phases (e.g. pyrite, zinc-sulfide), which might survive the immediate precipitation (Yücel et al., 2011; Gartman et al., 2014).

Furthermore, besides reactions with basaltic rocks, circulating waters might have interactions with ultramafic rocks as well in mid-ocean ridge environments. This leads to a very special set of geochemical reactions called serpentinization. Serpentinization occurs due to aqueous alteration of ultramafic rocks rich in minerals olivine and pyroxene. Ultramafic rocks are mainly mantle rocks and they might be transported to shallower depths by different tectonic forces. Olivine and pyroxene minerals are stable in high temperature and pressure conditions in the mantle, however displacement of ultramafic rocks to depths of lower temperature change the stability of these minerals and they start to react with circulating water (e.g., McCollom and Bach, 2009). Serpentine group minerals, as well as magnetite and brucite are produced as a result of serpentinization. One of the most important consequence of serpentinization is production of H_2 by set of redox reactions. Further, serpentinization is an exothermic reaction therefore it may have some contributions to hydrothermal circulation and fluids form under the control of serpentinization might have alkaline pH as opposed to other main black smoker type hydrothermal fluids (Kelley et al., 2001; McCollom and Bach, 2009; Kelley and Shank, 2010; McCollom and Seewald, 2013).

1.2.3 Hydrothermal Plume Processes

Hydrothermal plumes are generated when hydrothermal fluids are released from the subseafloor into deep water column. Studying geochemistry of hydrothermal plumes are important for two main reasons (1) geochemical anomalies created in the water column by hydrothermal plumes provide evidences in discovering new vent sites and (2) since they are the primary sources for hydrothermally generated chemicals, geochemical reactions happening in the plume determine the fate of evolution and transportation of these species along ocean basins (e.g. Field and Sherrell, 2000; German and Von Damm, 2003; Sands et al., 2012; Resing et al., 2015; Fitzsimmons et al., 2017; Waeles et al., 2017; Lough et al., 2019). As high temperature hydrothermal fluids are ejected from vents, they are buoyant and start to rise because deep water column has higher density due to having much colder temperatures (2-4 °C). Fluids rise with their initial buoyancy at around 150-400 meters above the vent and the character of the hydrothermal fluid and stratification in the local deep ocean basin determine how far hydrothermal fluids rise until reaching background seawater density (Lupton et al., 1995; German and Von Damm, 2003). Progressive dilution and cooling occur as hydrothermal plume rises and mixes with ambient seawater. Hydrothermal plume becomes less buoyant in time and the density of the rising plume is getting similar with the surrounding deep-water column. Then, the buoyancy is terminated at a maximum height above the vent where hydrothermal plume can reach and it starts to disperse laterally. Hydrothermal plume is called as "buoyant plume" in the first stage where the hydrothermal plume rises in the deep-water column and it is known as "nonbuoyant plume" (or sometimes "neutrally buoyant plume") when density is balanced and hydrothermal plume disperses laterally (Lupton et al., 1995; German and Von Damm, 2003) (Figure 1.5). Different dissolved chemical species present in the hydrothermal plumes exhibit different behaviors during the hydrothermal plume rise. For example, ^{3}He is considered as a conservative hydrothermal product and it exhibits an inert behavior therefore its concentration can only be changed by dilution. Although hydrothermal fluids are

diluted approximately ~10^4 fold before they reach nonbuoyant plume stage, ^{3}He might be traced long distances in the water column (Figure 1.5).

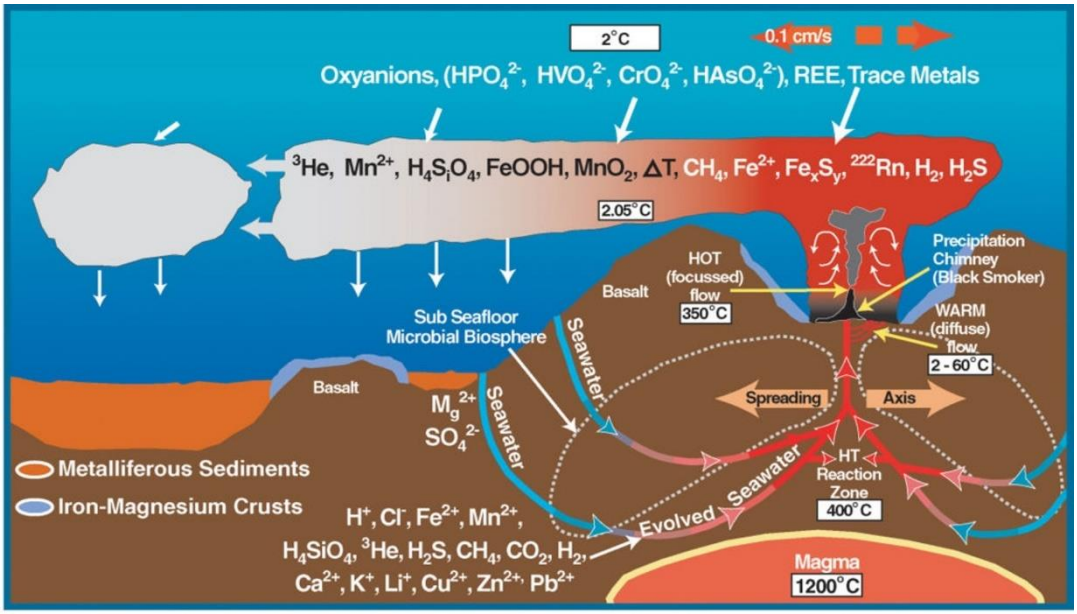

Figure 1.5. Schematic view of hydrothermal plume development (Credit: NOAA)

For example, Lupton and Craig (1981) first traced the dispersal of ^{3}He more than 2000 km from the vent site across the southern Pacific Ocean. Further, there are different reduced dissolved gases in the hydrothermal plume such as H_2S, CH_4, and H_2, and they might show relative depletions as the plume rises. For example, one of the most enriched gases in the hydrothermal fluids is H_2S. It faces with rapid reactions such as oxidation into sulfate phases and/or precipitation with metals as metal sulfides (e.g. German and Von Damm, 2003; Tivey et al., 2007) (Figure 1.5). Therefore, concentration of H_2S is getting depleted as the buoyant plume evolves. Moreover, hydrothermal fluids show great enrichments of metals when compared to ambient seawater, and these metals have pivotal roles and prominent implication on the element cycle in hydrothermal plumes. Fe and Mn are considered as the most enriched metals in hydrothermal fluids so they form a large part of the hydrothermal metal pool. Hydrothermal fluids before ejecting into deep water column carry mostly reduced dissolved forms of these metals (i.e. Fe^{2+} and Mn^{2+}). Upon the entry, Mn exhibits relatively more conservative behavior than Fe and tend to stay in the solution

as dissolved Mn since its oxidation rate is much slower and it does not tend to form precipitates as sulfide phases (Feely et al., 1994b; Breier et al., 2012; Resing et al., 2015). In the oxygen rich deep-water column, however, reduced form of Mn eventually precipitates as oxides in a time scale of days to weeks. Studies showed that oxidation of Mn can be catalysed by microbial activity and also dissolved Mn can be removed from the hydrothermal plume by scavenging of Mn with Fe-oxidation products (Campbell et al., 1988; Cowen et al., 1990; Dick and Tebo, 2010; Dick et al., 2013).

On the other hand, rapid cooling leads Fe to precipitate as sulfide minerals upon the entrance of the deep ocean. Additionally, as hydrothermal plume evolves, Fe-sulfide formation process is followed by Fe-oxidation and generation of Fe-oxyhydroxides (Figure 1.5). Fe oxidation rate shows differences basin to basin. Field and Sherrell (2000) calculated Fe oxidation rates in different basins including Juan de Fuca Ridge, Gorda Ridge, 21° N EPR, 9° 45′ EPR, 17° S EPR, SW Indian Ridge, and Mid-Atlantic Ridge (for TAG and Rainbow vent fields) (Figure 1.6). Although this study does not completely represent Fe oxidation rates of complex forms in hydrothermal plumes, it still provides a general understanding on Fe oxidation rates for different ocean basins by considering external factors such as oxygen concentration and pH of the seawater (Field and Sherrell, 2000). Fe oxidation rate is the highest (e.g. 0.29 h in Rainbow vent field) in the North Atlantic due to having waters with relatively higher oxygen concentration and higher pH while it is getting slower through Pacific Ocean hydrothermal fields (e.g. 6.38 h in Juan de Fuca Ridge). Oxidation rates and resultant oxidation products of Fe are important because different studies already showed that they are important actors of the plume geochemistry. They both represent considerable fractions of Fe in the Fe pool and act as strong scavengers for different elements (Mottl and McConachy, 1990; Rudnicki and Elderfield, 1993; Field and Sharel, 2000; Feely et al., 1996; Breier et al., 2012; Fitzsimmons et al., 2017; Waeles et al., 2017; Hoffman et al., 2018). Further, as opposed to ideas stating immediate precipitation of dissolved Fe as sulfide or oxide particles from hydrothermal plumes in different basins, recent studies showed that some fraction of

dissolved Fe might be survived from immediate precipitation and transported through great distances in the water column (Resing et al., 2015; Fitzsimmons et al., 2017).

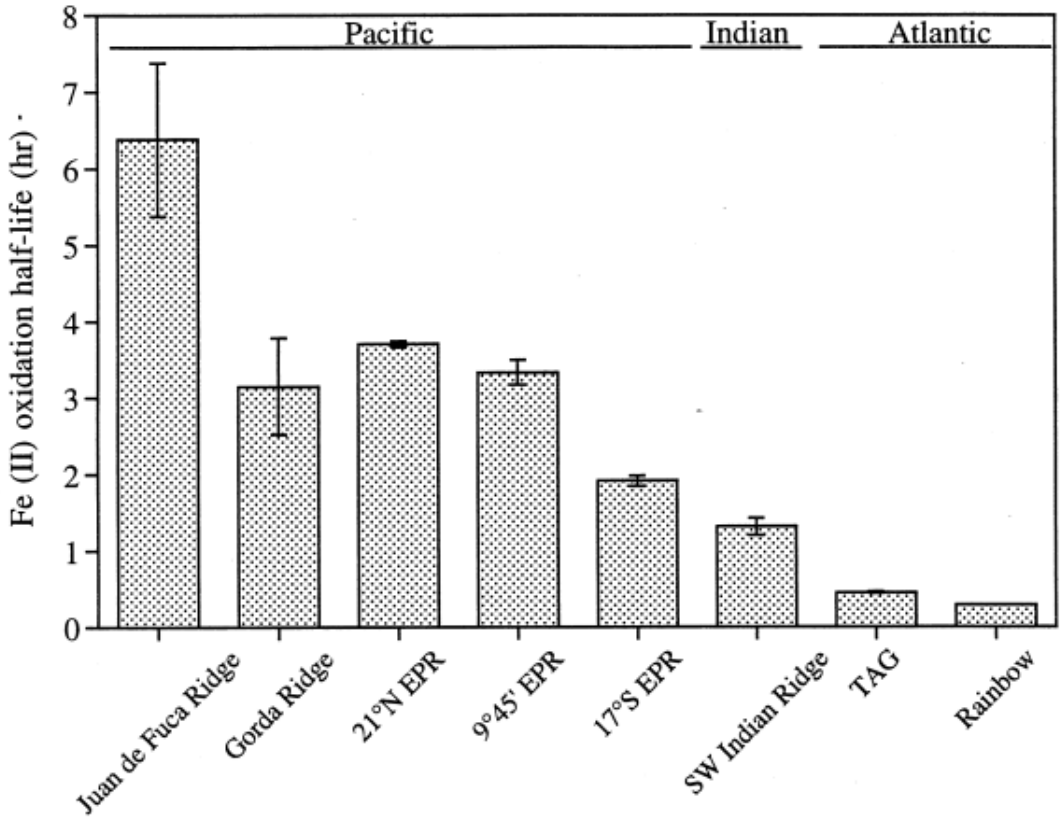

Figure 1.6. Bar chart showing Fe^{2+} oxidation half-lives in background deep seawater conditions for different basins and there is a solid decreasing trend in Fe^{2+} oxidation rate from Atlantic (e.g. MAR: TAG, Rainbow) to Pacific (e.g. Juan de Fuca Ridge) settings (Field and Sherrell, 2000)

For example, recent oceanographic studies conducted by GEOTRACES (Schlitzer et al., 2017) showed in all ocean basins that Fe can be detected thousands of kilometers away from hydrothermal vent sources (Resing et al., 2015; Fitzsimmons et al., 2017) (Figure 1.7). Two main mechanisms were suggested to explain how iron could be transported such long distances. Firstly, complexation of dissolved Fe with organic molecules has been proposed in different studies as a plausible mechanism for stabilization of hydrothermally generated dissolved iron (Bennett et al., 2008;

Sander and Kochinsky, 2011, Kleint et al., 2017). Secondly, nanoparticle iron phases were put forward to further investigate the dissolved Fe export mechanisms into deep-ocean interior and Yucel et al. (2011) showed that 10% of the total Fe is in the form of nanoparticles in the samples collected from vents in the East Pacific Rise and Eastern Lau Spreading Center. Different studies also further investigated and proved that nanoparticle iron phases are prominent in different hydrothermal vent plumes (Gartman et al., 2014; Findlay et al., 2015; Findlay et al., 2019; Yucel et al., 2020).

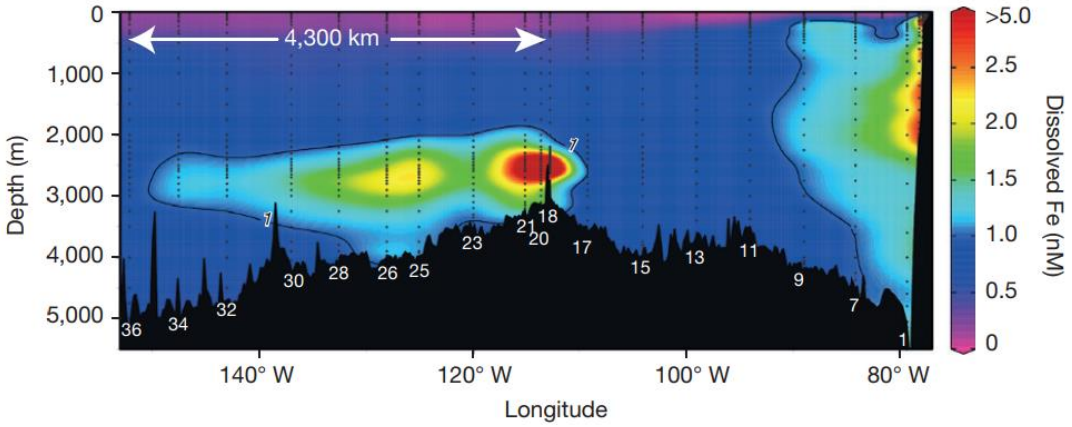

Figure 1.7. Zonal concentration plot of Fe shows that hydrothermal iron was traced 4300 kilometers along Eastern Pacific transect (Resing et al., 2015)

1.3 General Characteristics of Slow Spreading Mid-Atlantic Ridge System

Since the first discovery of hydrothermal vents on Galapagos Spreading Center, main attention was given to fast spreading ridges in hydrothermal vent studies. According to Baker et al. (1996), intense hydrothermal activity might have been mostly restricted to fast and ultra-fast spreading ridges since spreading rate has a positive correlation with magmatic fluxes, hence hydrothermal activity. However, the first discovery of high temperature hydrothermal venting in slow spreading Mid-Atlantic Ridge at TAG (26 °N), and other progressive discoveries of vent fields in following years such as Snakepit, Broken Spur, Logatchev, Rainbow, Lost City, Lucky Strike, and Menez Gwen showed that existence of prominent hydrothermal venting is not

only restricted to fast and ultra-fast spreading ridges (Rona et al., 1986; Campbell et al., 1988; Jean-Baptiste et al., 1991; Langmuir et al., 1993; Elderfield et al., 1993; Murton et al., 1994; James et al., 1995; German et al., 1996; Douville et al., 1997; Charlou et al., 2000; Kelley et al., 2001; Charlou et al., 2002; Douville et al., 2002; Früh-Green et al., 2003; Kelley et al., 2005; Schmidt et al., 2007). In slow spreading systems, some model studies showed that instead of solely high magmatic activity, hydrothermal venting might be controlled and maintained by tectonic character of the ridge. That is, detachment faulting might create a permeable medium in which fluids might penetrate to various depths and obtain heat from lower crust and upper mantle to maintain hydrothermal circulation (e.g. German and Lin, 2004; Allen and Seyfried, 2004; McCaig et al., 2007).

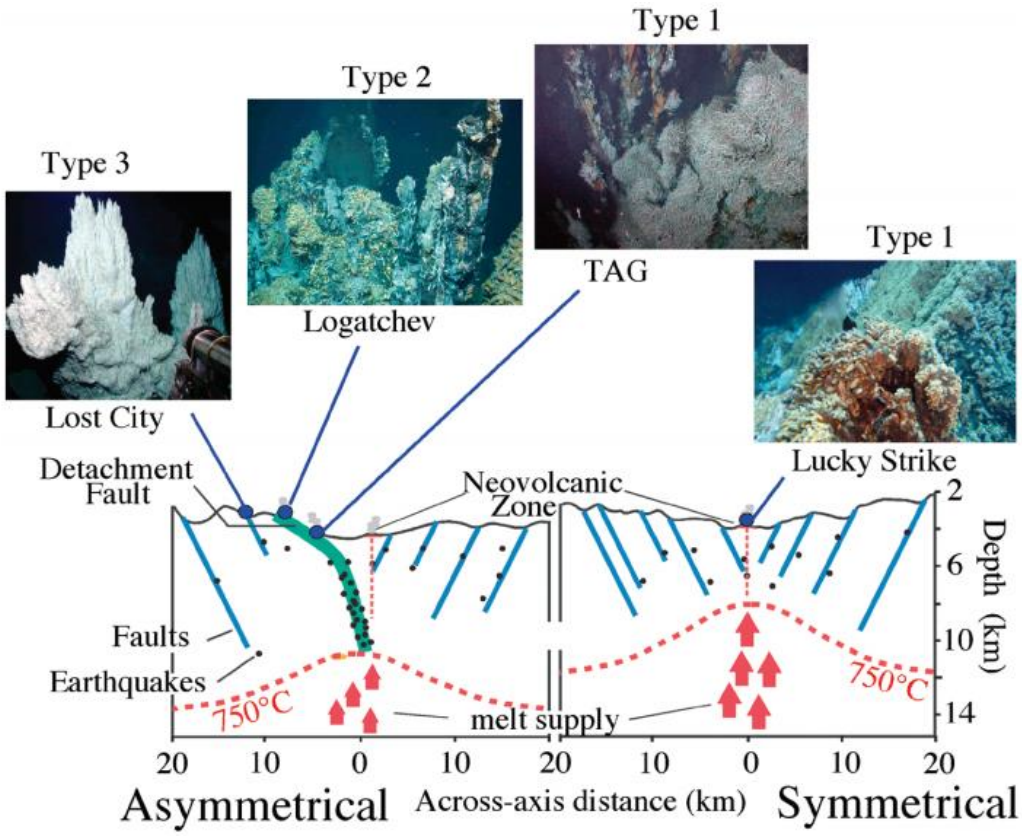

Figure 1.8. Diagram showing mode of formation of three main types of vent field present in slow spreading Mid-Atlantic Ridge system (Kelley and Shank, 2010)

The intense tectonic activity in relation with magmatic spreading in Mid-Atlantic Ridge creates geological heterogeneity throughout the entire ridge system (Schmidt et al., 2007). Therefore, different kinds of hydrothermal vent fields in different mode of formation systematics are present in Mid-Atlantic Ridge. There are three main types of hydrothermal vent fields in MAR (Figure 1.8) (Kelley and Shank, 2010). Type 1 systems form in neo-volcanic zones along ridge axis where magmatic eruptions occur and system mostly dominated by basaltic rocks. Type 1 systems host high-temperature black smokers driven by heat directly extracted from cooling magma and/or surrounding gabbroic crust (Kelley and Shank, 2010). Due to magmatic interactions, acidic vent fluids are enriched in magmatically derived CO_2, metals and variable concentrations of H_2S, H_2, and CH_4 (James et al., 1995; Von Damm et al., 1998; Jean-Baptiste et al., 1998; Charlou et al., 2000; Kelley et al., 2002). Phase separation might occur in the deeper portion of the system and alter fluid composition. Lucky Strike is the type example of this system. On the other hand, Type 2 systems are seen in areas where extreme crustal attenuation and detachment faulting are dominant (Figure 1.8) (Campbell et al., 1988; Charlou et al., 2002; Escartín et al., 2003, 2008; Petersen et al., 2009). In these areas, mixtures of different kinds of rocks such as gabbroic and ultramafic mantle rocks can be transported along detachment faults into shallower depths (Kelley and Shank, 2010). Hydrothermal circulations through all these materials results in high temperature black smokers with fluids in variable chemical compositions. Hydrothermal fluids might be enriched in different volatile species such as CO_2, H_2, CH_4, different metals and low-molecular weight hydrocarbons (Kelley and Shank, 2010). Specifically, magmatic-gabbroic interaction is responsible of CO_2 enrichments while water-rock reactions with peridotitic rocks (e.g. serpentinization) is the primary factors controlling H_2, CH_4 enrichments and low-molecular weight hydrocarbons in this system (Douville et al., 2002; Charlou et al., 2002; Schmidt et al., 2007; Konn et al., 2009; Charlou et al; 2010; Kelley and Shank, 2010). Additionally, phase separation might be prominent and occurring at different depths likewise Type 1 systems (e.g. Douville et al., 2002; Charlou et al., 2002; Charlou et al., 2010). The Logatchev vent

field is the type example of this system. Finally, Type 3 systems are formed far away from the spreading axis (Figure 1.8). In this system, ultramafic rocks are dominated and hydrothermal fluids are mainly formed due to interaction of water with these rocks. Therefore, fluid circulation is driven by exothermic serpentinization reactions and cooling of surrounding geological materials (mostly mantle rocks) (Kelley et al., 2001; Kelley et al., 2005; Früh-Green et al., 2003). The most important features of fluids seen in Type 3 systems is that this system contains relatively low temperature (up to around 90°C), high pH (9–11), metal and CO_2 poor fluids when compared to Type 1 and 2 (Kelley et al., 2005; Proskurowski et al., 2008; Seyfried et al., 2013). However, due to serpentinization reactions, fluids have high concentrations of CH_4, H_2 and low-molecular weight hydrocarbons (Kelley et al., 2005; Proskurowski et al., 2006, 2008; Konn et al., 2009; Lang et al., 2010). Lost City hydrothermal vent field is the only known example of Type 3 system in MAR.

1.4 Study Sites: Broken Spur, Rainbow and Lost City Vent Fields

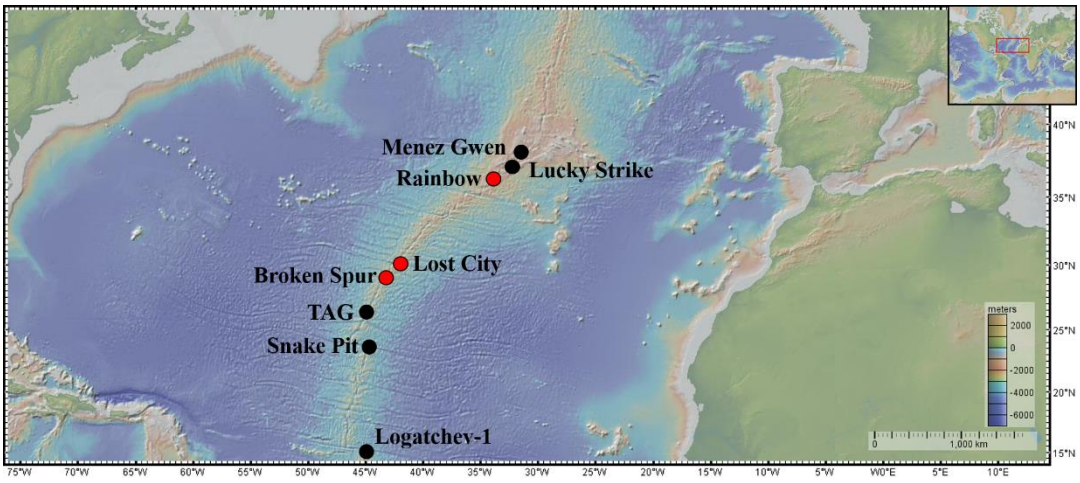

Figure 1.9. Map showing some of the active vent locations up to date in the North Atlantic Ocean. Visited hydrothermal vent fields in this study is marked in red. Map courtesy of http://www.geomapapp.org

Broken Spur vent field (29° 10′ N, 43° 10′ W) is a very good example of Type 1 systems according to Kelley and Shank (2010) classification. The vent field was

discovered in 1993 and first direct observations in the field was conducted by DSV Alvin (Murton et al. 1995; James et al., 1995). Broken Spur lies on the crest of a neovolcanic zone at a depth of ~3100 m in Mid-Atlantic Ridge (Murton et al. 1995; James et al., 1995) (Figure 1.9). Broken Spur hydrothermal vents are located in a 30-meter deep axial summit graben (ASG), both as within and on the walls of ASG (Figure 1.10) (Murton et al., 1995). Broken Spur hydrothermal field is covered by fresh and glassy pillow basalts with variable amount of pelagic sediment cover (James et al., 1995). Murton et al. (1995) described Broken Spur as an axial summit caldera formed by subsidence due to volcanic eruptions since fresh pillow lavas present on the graben walls. The largest hydrothermal vent (i.e. The Saracen's Head, 37 m high) at Broken Spur field was located at the center of the ASG (James et al., 1995). There are two main discontinuities which are cross-cutting each other as reported in the Broken Spur field (Figure 1.10).

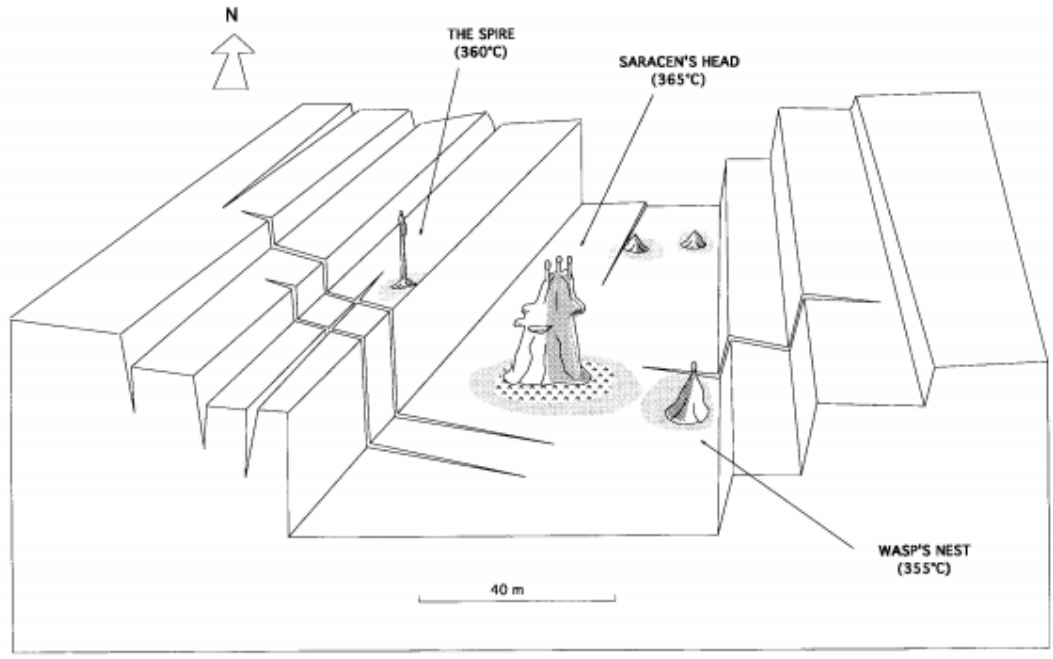

Figure 1.10. A sketch showing general distribution of vents and fractures in Broken Spur vent field (Murton et al., 1995)

Murton et al. (1995) suggested that the possible intersection of these discontinuities at the center might increase crustal permeability, hence support hydrothermal

circulation, and might be the cause of the largest vent present at the center (Figure 1.10). Broken Spur hosts high-temperature black smokers driven by heat extracted from cooling magma. Water-rock reactions with basaltic rocks control the formation and evolution of hydrothermal fluids in the vent field and it has high temperature (~ 360 °C) fluids with very high concentration of H_2S (~11 mmol/kg), relatively lower concentration of Cl (469 mmol/kg) and comparable amount of trace metals (e.g. Fe: ~2.2 mmol/kg; Cu: ~70 µmol/kg; Zn: ~90 µmol/kg) with respect to other hydrothermal vent sites in Mid-Atlantic Ridge (James et al., 1995; Charlou et al., 2010). The Rainbow hydrothermal vent field can be considered as an example of Type 2 system according to Kelley and Shank (2010) classification. The first direct observation of vent field was conducted in 1997 by DSV Nautile.

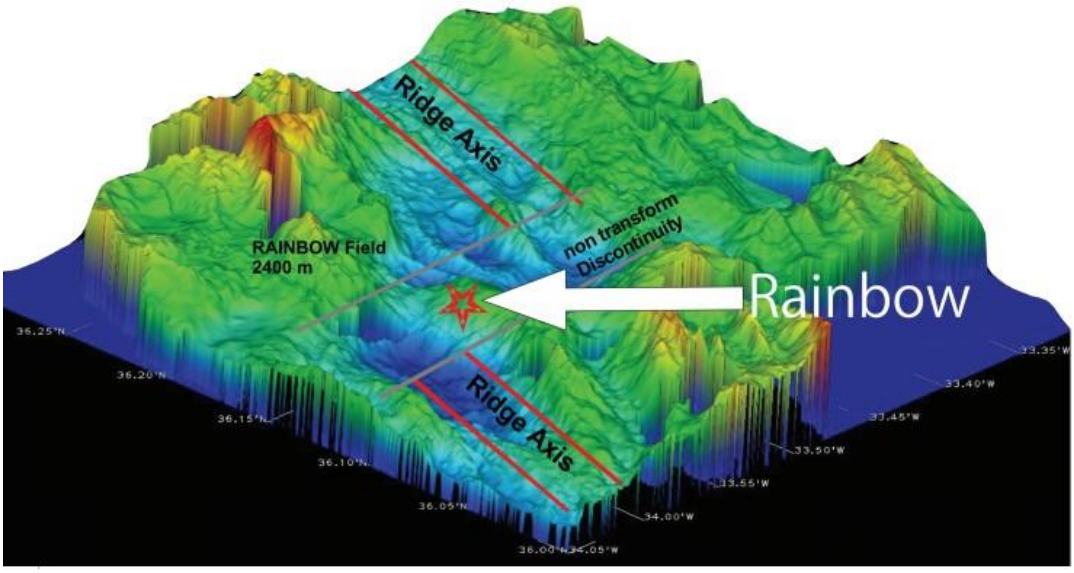

Figure 1.11. Map showing location of Rainbow hydrothermal vent field on a nonvolcanic ridge between the South AMAR and AMAR segments in Mid-Atlantic Ridge (Charlou et al., 2010)

The Rainbow field is located at 36° 14′ N, 33° 54′ W on a nonvolcanic ridge between the South AMAR and AMAR segments in the Mid-Atlantic Ridge at a water depth ~2300 meters (Figure 1.11) (German et al., 1996; Fouquet et al., 1997; Douville et

al., 2002; Charlou et al., 2010). The Rainbow vent field hosts 10 major active black smokers over 100 m x 200 m area (Douville et al., 2002; Charlou et al., 2002). The Rainbow massif mainly composed of serpentinized ultramafic mantle rocks which are covered by pelagic sediments and carbonates (Douville et al., 1997; Fouquet et al., 1997, Andreani et al., 2014). On the other hand, although exposures of mafic plutonic and volcanic rocks are relatively rarer in the hydrothermal field, volcanic rock outcrops are present within the northern and southern edges of the Rainbow massif (Andreani et al., 2014, Eason et al., 2016) (Figure 1.12).

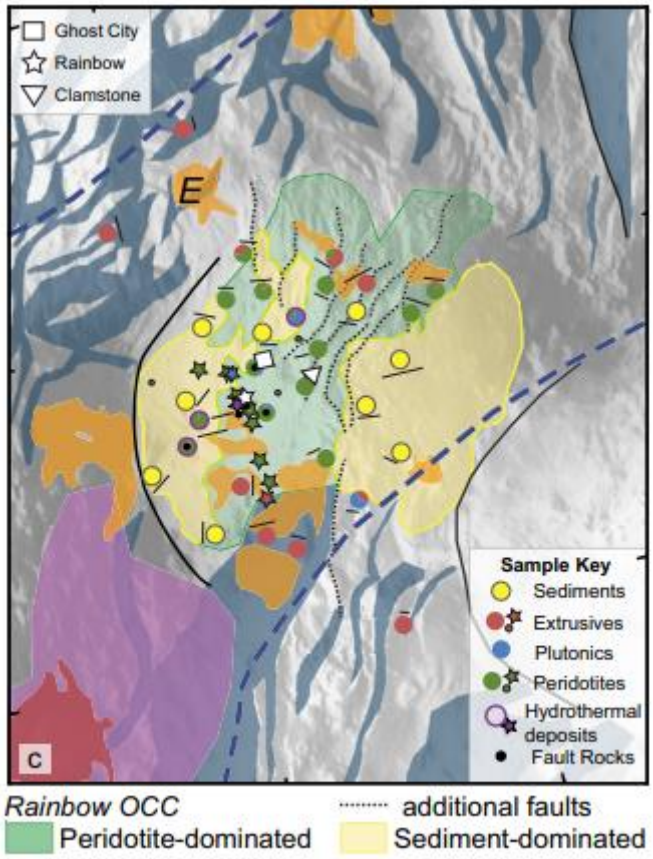

Figure 1.12. Geological map of Rainbow massif. Colors are representing exposures of different geological materials. White star indicates active Rainbow hydrothermal vent field (Eason et al., 2016)

Additionally, lithological and morphological considerations showed that dome-shaped Rainbow massif is an oceanic core complex transported by a west dipping detachment fault (Andreani et al., 2014). These geological complexities observing in the Rainbow hydrothermal field suggest that interplay of tectonic and magmatic processes must be considered to understand driving forces of high temperature hydrothermal activity in Rainbow hydrothermal field (Cave et al., 2002; German and Lin, 2004). Since it is an ultramafic-hosted system, serpentinized peridotites have the primary role on evolution of vent fluid geochemistry in Rainbow field, and high temperature vents (~ 365 °C) contain very low pH (~2.8) fluids with the highest concentration of trace metals (Fe, Zn and Cu), Cl (>750 mmol/kg) and relatively low concentrations of sulfide with respect to other vents in MAR (Douville et al., 2002; Charlou et al., 2010; Seyfried et al., 2011; Findlay et al., 2015). High concentration of Cl indicates phase separation in the subsurface and it has a primary control on metal solubility. Additionally, as a result of serpentinization reactions, Rainbow fluids contain high concentration of H_2 (~16 mmol/kg) and CH_4 (~2.5 mmol/kg) (Charlou et al., 2002; Charlou et al; 2010; Seyfried et al., 2011). It was recognized that long lived detachment faults are an important component of slow spreading ridges and might act as primary fluid circulation pathways (Kelley et al., 2005; McCaig et al., 2007; Escartin et al., 2008). However, recent studies showed that geophysical data indicates currently inactive detachment faulting in Rainbow therefore high temperature hydrothermal venting presents in this field might be fed by other sources such as melt bodies and/or gabbroic intrusions (Andreani et al., 2014; Horning et al., 2018). As a supporting statement, Allen and Seyfried (2004) indicated that a magmatic heat source is needed near the Rainbow hydrothermal vent field in order to maintain high temperature venting with high fluid flow rates seen in the Rainbow. Further, in addition to active venting sites, there are two fossil hydrothermal areas known as Ghost City and Clamstone in the Rainbow hydrothermal field, and they are located at water depths of 2100 meters and 1980 meters, respectively. They are associated with serpentinized peridotites and gabbros and they contain fossil rich carbonates (Lartaud et al. 2010; Lartaud et al.,2011).

Vent fluids of these fields were inferred as low temperature and metal-poor, hence resembles to present day Lost City hydrothermal fluids (Lartaud et al., 2010; Lartaud et al., 2011). Age of these systems were determined as 110±0.9 kyr for Ghost City and 25 kyr for Clamstone, which implies the activity and stability of the Rainbow vent field over time (Lartaud et al., 2010; Lartaud et al., 2011). Fluid geochemistry studies further showed that Rainbow vent fluids show stability in both temporal and spatial scales. Studies in 1997 (Douville et al., 2002), and 2008 (Seyfried et al., 2011) indicated fluid composition of Rainbow have not changed substantially across ~10 years timespan and samples obtained from individual vents in Rainbow field exhibits uniform composition, which might indicate that Rainbow fluids might be fed by a single deep source (Charlou et al., 2002; Charlou et al., 2010; Seyfried et al., 2011).

As stated before, the Lost City hydrothermal vent field (30° 07.41 ′N, 42° 07.27′ W) is the only known example of Type 3 systems in MAR (Kelley and Shank, 2010). It was discovered in 2000 at ~800 m water depth in Mid-Atlantic Ridge (Kelley et al., 2001) (Figure 1.9). The Lost City is an off-axis system. That is, the hydrothermal field is located on the Atlantis Massif, which is 15 km far away from the axial valley of Mid-Atlantic Ridge (Kelley et al., 2001; Kelley et al., 2005).

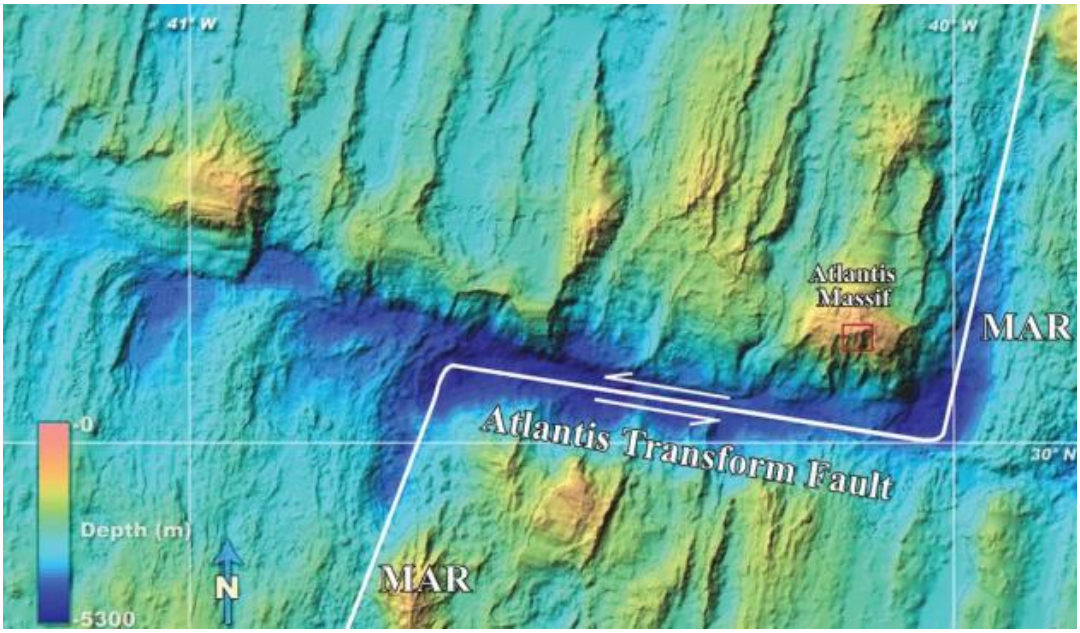

Figure 1.13. Bathymetric map of Atlantis Massif (Kelley et al., 2007)

The Atlantis Massif is 400 m high with respect to surrounding seafloor and it is bounded by Atlantis Fracture Zone in the south and Mid-Atlantic Ridge in the east (Figure 1.13). The Lost City hydrothermal field covers 100 m x 200 m area and approximately 15 known hydrothermal chimneys rises on top of different geological materials including serpentinized peridotites and altered gabbroic rocks (Kelley et al., 2001; Früh-Green et al., 2003; Denny et al., 2015) (Figure 1.14). Poseidon (height: ~ 60 m) is the largest chimney structure in the hydrothermal field. As opposed to classical metal-sulfide rich black smoker type chimneys, Lost City has carbonate chimneys with mineralogy including calcite, aragonite ($CaCO_3$) and variable amount of brucite ($Mg(OH)_2$) (Kelley et al., 2001; Kelley et al., 2005).

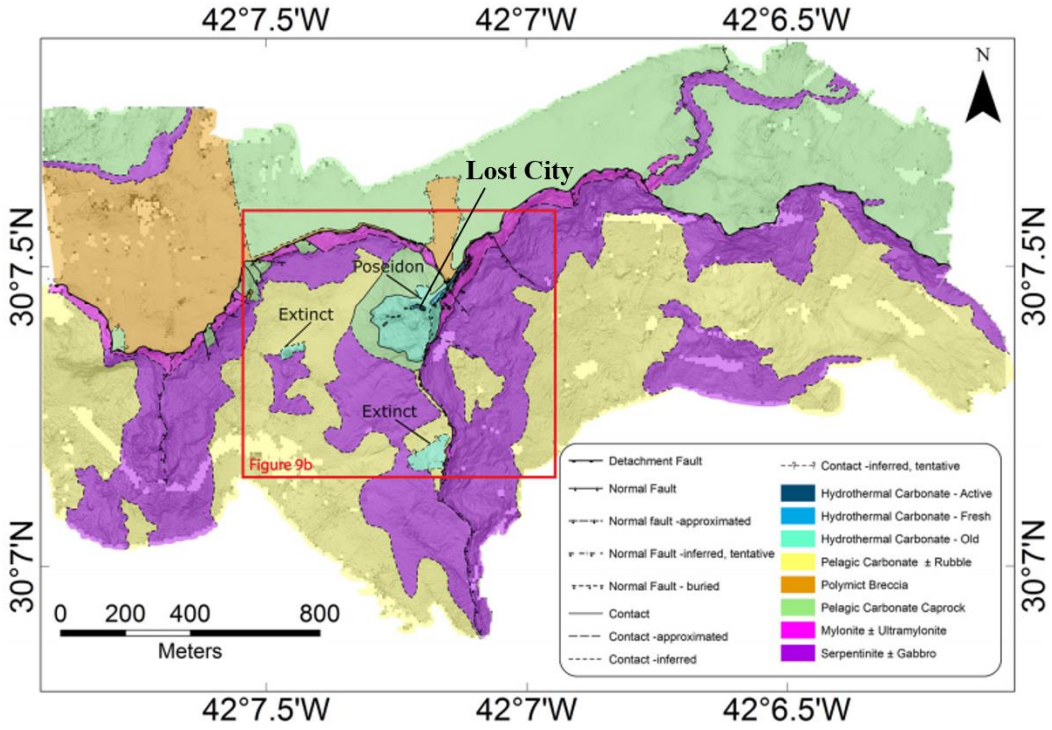

Figure 1.14. Geological map of Atlantis massif and Lost City hydrothermal vent field. Colors are representing exposure of different geological materials including serpentinite, gabbro and carbonates (see Denny et al., 2015 for further details)

Hydrothermal fluid composition emitted in the Lost City field is a direct result of serpentinization reactions between circulation water and peridotites. Fluids are very high in pH (9-11), low in temperature (up to 94 °C), Ca rich and metal poor (Kelley

et al., 2005; Kelley and Shank, 2010). High pH and high Ca concentrations favor the formation of carbonates as a chimney material after the mixing of Lost City fluids with ambient seawater. Additionally, volatile composition of Lost City fluids resembles Rainbow by containing relatively high concentration of H_2 (up to 14.4 mmol/kg), CH_4 (1-2 mmol/kg) and low molecular weight hydrocarbons since both systems evolve mainly under the control of serpentinization reactions however Lost City fluids have significantly small amount of CO_2 (Charlou et al., 2002; Kelley et al., 2005; Proskurowski et al., 2008; Lang et al., 2010; Charlou et al., 2010). Heat source driving the hydrothermal circulation in Lost City system is considered as lithospheric cooling and exothermic serpentinization reactions (Kelley et al., 2001, 2005; Früh-Green et al., 2003). Regarding its location far away from the spreading axis and its low temperature character, a magmatic heat source might not have prominent contributions however Allen and Seyfried (2004) proposed that it is still possible to have magmatic interaction in Lost City by considering tectonic character of Mid-Atlantic Ridge. Dating efforts showed that hydrothermal activity in the Lost City vent field has been ongoing for more than 120 kyr, which implies the stability of the field over time (Ludwig et al., 2011).

1.5 Aims of This Study

As emphazised in previous sections, understanding the role of hydrothermal vents and their products in both local and global scale in Earth system has been an important effort. Until now, different studies have tackled with that question mainly by focusing on (bio)geochemical processes in the subseafloor or deep ocean water column. However, mechanisms occuring between these two stages are still poorly constrained. This thesis, therefore, mainly aims to understand the procceses occuring at the intermediate stage by establishing the connections between subseafloor water/rock reactions and rising plume processes. In that respect, a multielemental dataset were generated for hyrothermal vents in Mid-Atlantic Ridge (MAR) system. MAR is a very special tectonic environment and its distinct geological characteristics

result in formation of compositionally different hydrothermal vent fields in close proximities. Hence, MAR opens a gate to study formation, evolution and near field transportation of hydrothermal products in distinct settings.

In that respect, in this study, following objectives were aimed to achieve by examining one representative example of each vent type exists in Mid-Atlantic Ridge system (i.e. Type 1: Broken Spur; Type 2: Rainbow; Type 3: Lost City) (see Kelley and Shank, 2010):

(i) Establishing a comprehensive understanding on how different hydrothermal systems behave under different conditions by comparing different water/rock reaction processes occuring in Rainbow, Broken Spur and Lost City hydrothermal vent fields

(ii) Examining mobilization and near field transportation of hydrothermal vent products and understanding how different subsurface water/rock reaction dynamics create compositonal shifts and control the geochemical evolution of hydrothermal vent plumes in different vent fields

(iii) Understanding the degree of temporal and spatial varitions observed in each visited hydrothermal vent field in order to better understand the geochemical stability and/or variability of Mid-Atlantic Ridge system over time

(iv) Examining further possible roles of hydrothermal vents in different major geological events in Earth's history by using the approaches obtained from this study and present in the literature

Furthermore, this thesis is organized as follows: Chapter 2 gives information on materials that were used in collecting hydrothermal fluid samples and methods that were conducted to generate a multielemental geochemical dataset. Chapter 3 is designed for results of different geochemical species. In that chapter, both calculated endmember hydrothermal fluid compositions of Rainbow, Broken Spur and Lost City vents and measurement results for Rainbow and Broken Spur rising plumes are

given. In Chapter 4, a comprehensive discussion on the geochemical processes controlling the formation and evolution of hydrothermal (nano)particles are presented in the subsurface and hydrothermal plumes. Then, Chapter 4 continues with examination of spatial and temporal variations of Rainbow, Broken Spur and Lost City systems and it ends with possible important roles that hydrothermal vents might have played in major geological event in Earth's history. Finally, in Chapter 5, a comprehensive summary of this thesis is presented.

CHAPTER 2

MATERIALS AND METHODS

2.1 Sample Collection

All hydrothermal fluid samples were collected during the July-August 2018 TRANSECT research cruise to Mid-Atlantic Ridge with N/O L'Atalante and remotely operated vehicle (ROV) Victor 6000 (Figure 2.1). Broken Spur, Rainbow and Lost City hydrothermal vent fields were visited in TRANSECT cruise and high temperature hydrothermal fluid samples were collected from individual chimneys in Fumeur Tres Dense, Fumeur Nouveau and Magali vents in Rainbow hydrothermal field; Chandelier, Dragon, and Spire vents in Broken Spur hydrothermal field; Marker B in Lost City hydrothermal field (Table 2.1).

Figure 2.1. (A) N/O L'Atalante, (B) ROV Victor 6000, (C) Titanium syringes (major samplers) for high temperature fluid sampling (Credit: IFREMER)

Table 2.1 Coordinates and depths of visited individual vents in Rainbow, Broken Spur and Lost City hydrothermal fields

Vent Field	Latitude (N)	Longitude (W)	Depth (m)
Rainbow			
Fumeur Tres Dense	36° 13 '45.12"	33° 54' 3.24"	2238
Fumeur Nouveau	36° 13' 45.18"	33° 54' 12.78"	2321
Magali	36° 13' 75.25"	33° 54' 22.83"	2238
Broken Spur			
Spire	29° 10' 5.2"	43° 10' 28.45"	3060
Dragon	29° 10' 2.96"	43° 10' 27.59"	3046
Chandelier	29° 10' 3.27"	43° 10' 26.22"	3046
Lost City			
Marker B	30° 7′ 24.6"	42° 7′ 16.02"	784

At the orifice, hydrothermal fluids were collected using titanium syringes (also called "major samplers") deployed from ROV Victor 6000, and each major sampler can collect approximately 760 mL of hydrothermal fluids (Figure 2.1C). Major samplers use a titanium syringe system to draw high temperature vent fluids through a nozzle when they are triggered (Von Damm et al., 1985). In each sampling, the nozzle (~15 cm long) of the major sampler was placed ~10 cm inside the vent orifice to sample the actual vent fluid before mixing with ambient seawater (Figure 2.2A). Additionally, Pepito samplers and Niskin bottles were used to take samples from different heights in the hydrothermal plume (0.1 m to 12 m) only in Rainbow and Broken Spur fields. Further, temperatures of fluids were monitored with high temperature probe carried by ROV Victor 6000 just before each sampling (Figure 2.2B). However, temperatures were not measured in real time during sampling because: (1) high temperature probe is not attached to the major samplers and (2) major samplers and temperature probe can be carried with only one of the manipulator arm of ROV (called as "Maestro").

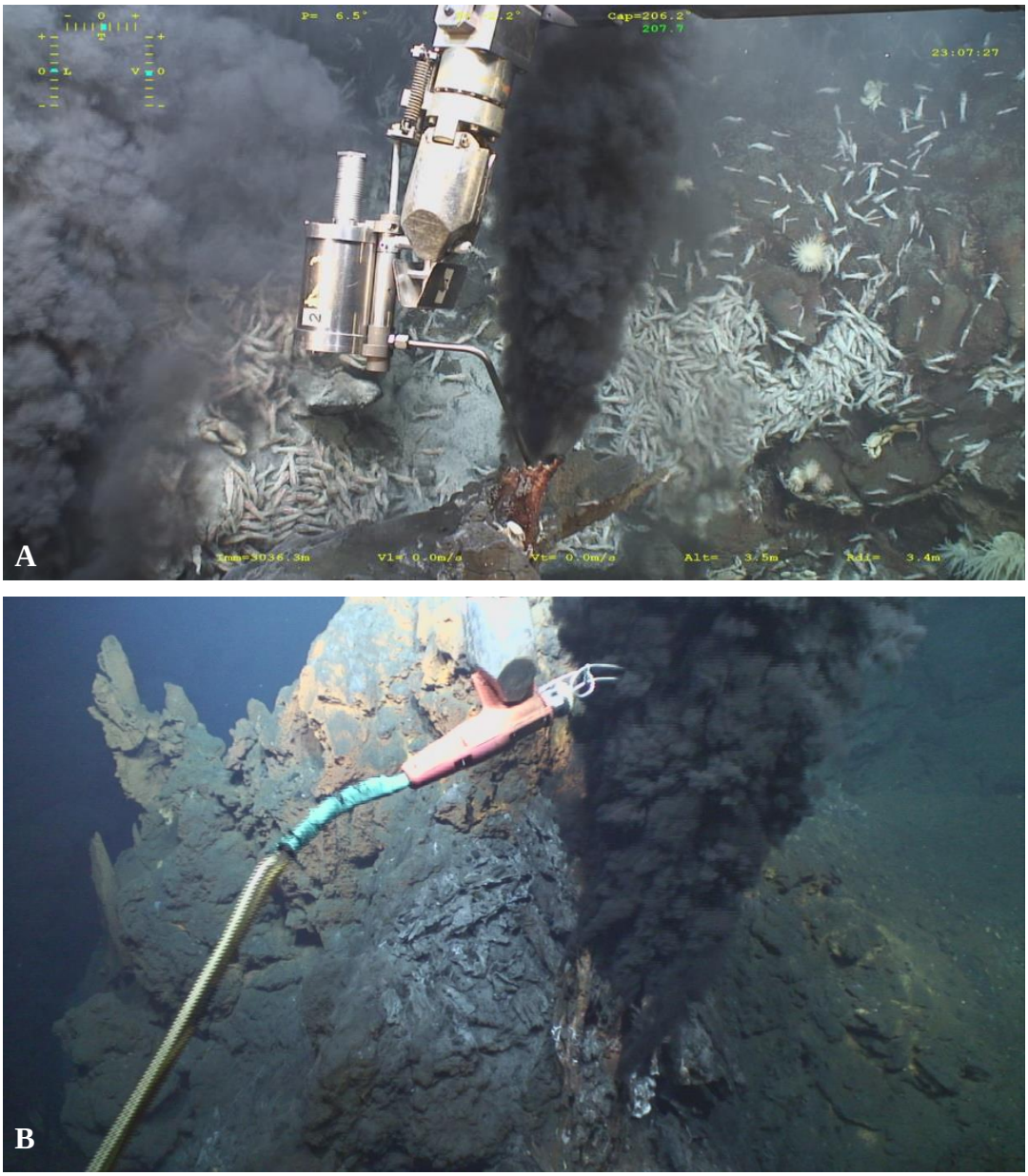

Figure 2.2. (A) Underwater hydrothermal fluid sampling with titanium samplers and (B) temperature measurements with high temperature probe (Credit: Mission TRANSECT/ Le Bris et al. (2018))

Therefore, the probe was kept stationary for 2-3 minutes inside each orifice and discrete temperature measurements were obtained for each vent to see the temperature fluctuations. Then, recurring maximum temperatures for each fluid samples are reported. Maximum underwater ROV operation took place 36-hours and

an elevator system was used in order to exchange filled samplers with empty ones during each corresponding dive. Upon retrieval of the fluid samples on ROV Victor 6000, onboard sample processing was conducted as soon as possible. Fluid aliquots were extracted for shipboard pH analysis, colorimetric determination of dissolved Fe, and shore-based analysis for H_2S, trace metals and major ions. pH analysis was conducted at 25 °C, 1 atm immediately after each sample recovery by potentiometry using an Ag/AgCl combination reference electrode in collaboration with LECOB team.

2.2 Colorimetric Iron and Hydrogen Sulfide Measurements

Subsamples for onboard dissolved iron measurements for each fluid samples were filtered through 0.2 μm pore size filters and were treated with 1 mL 4N HCl. After 6-10 hours of treatment, the samples were analyzed by the Ferrozine assay for dissolved Fe^{2+} with 1 cm quartz cuvettes at 562 nm wavelength using an Ocean Optics spectrophotometer (Stookey, 1970). 1 mL 2.5 M NH_4-Acetate, 1 mL 0.1 M hydroxylamine hydrochloride, 1 mL 0.01 M ferrozine and enough amount of MilliQ water by considering the dilution factor were added to all filtered samples with different volumes according to the corresponding iron concentration of each fluid samples (e.g. Yucel et al., 2011; Findlay et al., 2015). All dissolved Fe^{3+} was converted to Fe^{2+} by using hydroxylamine hydrochloride as a reducing agent. In each day before the measurements, spectrophotometer was calibrated by iron standard stock solution prepared by using ferrous ammonium sulfate ($(NH_4)_2Fe(SO_4)_2 \cdot 6H_2O$).

On the other hand, unfiltered subsamples (1.5 ml) for dissolved hydrogen sulfide measurements were treated with 1.5 ml NaOH and 1.5 ml 0.05 M zinc acetate to adjust pH into a proper level and precipitate dissolved H_2S as ZnS, respectively. After sample tubes were shaken properly, white precipitation of ZnS accumulated at the bottom. Then, all fixed subsamples were stored at -20 °C. Upon retrieval of samples to METU IMS laboratories, they were analyzed by methylene blue method for dissolved H_2S (Cline, 1969). A proper dilution was applied for all fluid

subsamples considering high H_2S concentrations. Then, 0.1 mL 0.02 M N, N-dimethyl- p-phenylene diamine, and 0.1 ml 0.1 M $FeCl_3.6H_2O$ were added to each sample in the given order. After having the color change and waiting approximately 1-hour, all samples were measured with 1 cm quartz cuvettes at 670 nm wavelength using a Cary Varian UV-Vis spectrophotometer. Spectrophotometer was calibrated by sulfide standard stock solution prepared by using sodium sulfide ($Na_2S.\ 9H_2O$). Detection limit for hydrogen sulfide measurement is around 0.3 μM.

2.3 Analytical Methods for Major Ions and Metals

Subsamples for shore-based analysis were transferred to polypropylene tubes for measurements of major and trace chemical species in the vent fluids. Aliquots were acidified with 1 mL 4N HCl immediately after subsampling and all subsamples for chemical analysis were stored at -20 °C. Concentration of anions (Cl, SO_4, Br) were determined in Ion Chromatography (IC) using a Dionex AS4A-SC separation column, sodium hydroxide eluent and ASRS-I suppressor whereas concentration of cations (Mg, Na, Ca, K, Li) were determined with a Dionex CS12-SC separation column, with methane sulfonic acid eluent and CSRS-I suppressor. Filtration through 0.45 μm pore size filters and 100-fold dilution were applied for each sample before the measurement. Detection limit of both anions and cations are all less than 0.5 μM. On the other hand, concentrations of Fe, Mn, Cu, Zn, Cd, Ni, Co, Cr, Al, Ag, Si were measured by a NexIon 350X Inductively Coupled Plasma Mass Spectrometry (ICP-MS). 1 mL 6N HNO_3 was added and 200-fold dilution were applied to all subsamples before the measurement. Perkin Elmer multi-element calibration standard solution for metals (Fe, Al, As, Mn, K, Mg, V, Co, Cr, Ni, Se, Sr, Ca, Ba, Ga, Be, Pb, Cs) in 5% HNO_3 with concentration of 10 μg/mL was used to prepare calibration standards. Also, Internal Yttrium standard was used to correct the intensity deviations during measurement with ICP-MS. Detection limit of metals measured in ICP-MS are all less than 0.05 μM. All concentrations obtained from IC

and ICP-MS analysis were calculated by using calibration curves for each element after considering dilution factors, and molar mass calculations.

2.4 Calculation of Endmember Fluid Compositions

Experimental studies have shown that reactions of fluids with basalt, gabbro and peridotite at high temperatures and low water/rock ratios result in nearly quantitative removal of Mg and SO_4 in hydrothermal fluids (Bischoff and Dickson, 1975; Moitl and Holland, 1978; Seyfried and Bischoff, 1981; Janecky and Seyfried, 1986; Seyfried et al., 2007). However, some fraction of seawater is always present within the collected hydrothermal fluid samples because of (1) filling the dead volume of major samplers with seawater before the sampling, (2) seawater penetration into major samplers during the sampling procedure as a contamination factor, (3) mixing of hydrothermal fluids with seawater in the subsurface and/or within the chimney structures prior to venting (Von Damm et al., 1985; Von Damm, 2000). All these cases cause elevation of Mg concentration in sampled hydrothermal fluids. The lowest Mg concentration observed in hydrothermal fluid samples indicates the highest fraction of vent fluid collected in the samplers. Hence, collected samples typically represent two-component mixing of zero Mg endmember fluids with ambient seawater. As a result, in order to make the correction, compositions of each vent fluid are calculated by applying least-squares regression method weighted to pass through the background seawater composition and extrapolated to 0 mmol/kg Mg concentration in plots of Mg versus each individual conservative chemical species (e.g. Fe, Mn, Cl, Ca, K, Na etc.) for all fluid samples collected from one vent orifice in each vent field (e.g. Von Damm et al., 1985; Von Damm, 2000; McDermott et al., 2018). On the other hand, pH measurements conducted in hydrothermal fluid samples have always large uncertainties with respect to other chemical compounds for two reasons (1) plots of Mg vs pH have resemblance to titration curve rather than having a linear relationship like most of the other chemical species because two component mixing of seawater and hydrothermal fluids result in titration of seawater

alkalinity with high concentration of H^+ coming from low pH hydrothermal fluids (Von Damm, 2000) therefore, by using this method, calculating of pH endmember is more difficult than other chemical species and (2) metal sulfide and oxide precipitation in samplers during sample recovery and sample processing might lead to shift the fluid pH from its in situ values and result in observing lower pH (Von Damm et al., 1985; Seewald and Seyfried, 1990; Von Damm, 2000; Seyfried et al., 2011). As a result, pH is not calculated by using this method due to having a non-conservative behavior during seawater and hydrothermal fluid mixing and minimum measured pH at 25 °C, 1 atm conditions (also corresponding to minimum Mg concentration for corresponding fluid sample) is reported.

2.5 Generation of Mixing Lines for Hydrothermal Plumes

After calculating the endmember fluid compositions, mixing lines are created for different elements in order to understand geochemical dynamics in the hydrothermal plumes. Since Mg exhibits a conservative behavior during mixing of endmember hydrothermal fluids with seawater in the plume development stage, we preferred to use Mg as a mixing tracer. Seawater is rich in Mg while hydrothermal fluid endmembers have near zero Mg concentrations as stated above. Therefore, mixing lines are generated between the average endmember fluid compositions of corresponding vent fluid and background seawater composition (e.g. McDermott et al., 2020). Shifting from the mixing lines basically indicates there should be removal and/or enrichment of corresponding element.

CHAPTER 3

RESULTS

This chapter, starting from the general observable features in Rainbow, Broken Spur and Lost City hydrothermal vent fields, provides the results of endmember fluid concentrations for corresponding hydrothermal fluids. In addition to that, results of measurements of different chemical species from different heights in the Broken Spur and Rainbow hydrothermal rising plumes are presented as well.

3.1 General Observations

The study was conducted in a total of 7 different individual hydrothermal vents in Broken Spur (i.e. Spire, Dragon, and Chandelier), Rainbow (i.e. Fumeur Tres Dense, Fumeur Nouveau, and Magali) and Lost City (i.e. Marker B) hydrothermal fields. At Broken Spur, pillow basalts on the basement support the idea that Broken Spur is forming near the spreading axis, where volcanic eruptions created these basalt layers. However, pillow basalts were not fresh and covered with sediments with varying thicknesses (>1 mm). Mitchell et al. (1998) calculated 29 °N area (where Broken Spur field is located) in Mid-Atlantic Ridge has a sedimentation rate of <10 mm/ka therefore it is possible to assume certain amount of time passed since last eruption in Broken Spur field. Additionally, Spire was a mature vent during the date of sampling while Chandelier and Dragon were two relatively newly forming chimneys. Therefore, Spire, which was also described in James et al. (1995) has a tall (>10 m) and complex edifice (Figure 3.1). On the other hand, orifices where samples were taken in Chandelier and Dragon chimneys were less than 2 meters height from the basement basalts. The color of chimneys in Broken Spur is varying between dark gray to black, which is probably due to precipitation of metal sulfides as opposed to metal oxides displaying lighter colors (Figure 3.1).

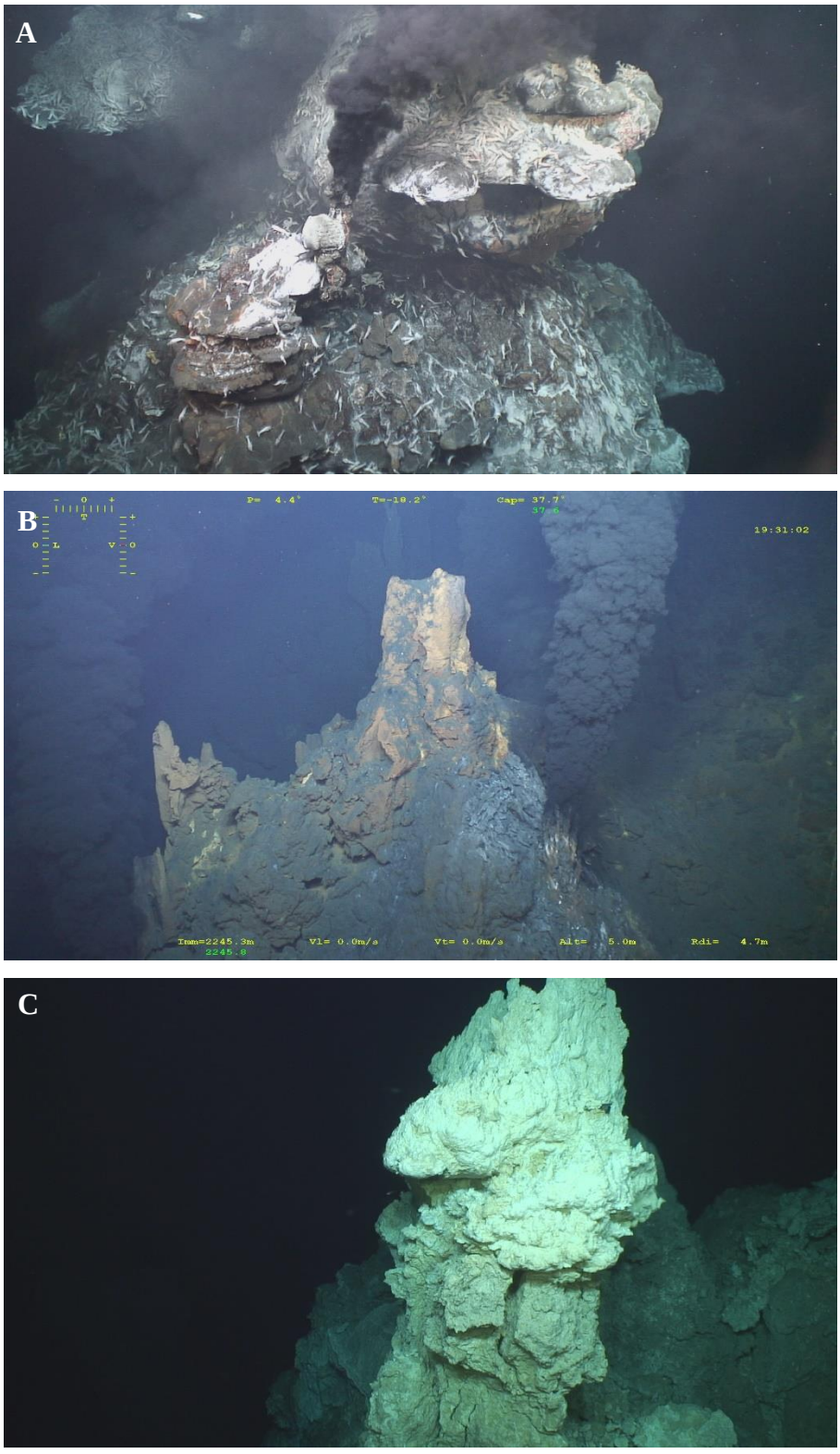

Figure 3.1. Representative field images of Broken Spur (A), Rainbow (B) and Lost City (C) hydrothermal vents (Credit: Mission TRANSECT/ Le Bris et al. (2018))

A similar intense venting of black smokers was observed in Rainbow hydrothermal vent field as well (Figure 3.1). Rainbow hydrothermal chimneys included Magali as well as two unnamed structures were called as Fumeur Tres Dense and Fumeur Nouveau were mature vents having plumes reaching couple of meters into the deep-water column from each vent orifice. No pillow basalts were observed around Rainbow vents. Being located on peridotites in an oceanic core complex far away from the spreading axis might be the main reason for that (Charlou et al., 2002; Charlou et al., 2010; Kelley et al., 2010; Andreani et al., 2014). The color of chimneys in Rainbow is reddish to brownish, which indicates metal oxide forms precipitating nearby (Figure 3.1). On the other hand, no black smokers and intense venting was observed in Lost City vent field, instead it emitted colorless fluids (Figure 3.1). Marker B was a mature and tall chimney (>10 m) with a color of milky white, which indicates precipitation of carbonate minerals around the chimney (Kelley et al., 2001, 2005; Le Bris et al., 2018).

3.2 End-member Fluid Geochemistry

3.2.1 Temperature and pH

Temperature measurements were conducted on top of the orifice of each individual hydrothermal chimney before each fluid sampling in Rainbow, Broken Spur and Lost City hydrothermal vent fields. On the other hand, pH of each fluid samples was measured onboard at 25 °C, 1 bar (Le Bris et al. (unpub)). Focused and high temperature fluids collected from Fumeur Tres Dense, Fumeur Nouveau and Magali chimneys in Rainbow vent field exhibited temperatures ranging from 315 °C to 372 °C. High temperature Rainbow vents were acidic with pH values around 3.10. Moreover, high temperature Broken Spur hydrothermal fluids collected from Spire, Dragon and Chandelier vents had temperatures between 310 °C and 332 °C. Broken Spur vent fluids were acidic and pH measurements (at 25 °C, 1 bar) show relative variability in high temperature fluids. Minimum pH values were in between 3.01 and

3.47 for Broken Spur vents (Table 3.1). On the other hand, Lost City showed the lowest hydrothermal vent fluid temperatures among other fields. Temperatures measured from focused fluids in Lost City is around 84 °C. Likewise, pH in Lost City fluids was also highly unique since it had an alkaline pH of 10.32 (Table 3.1).

Table 3.1 Table representing maximum temperature measured at the vent orifice, minimum pH at 25 °C, 1 atm, measured minimum Mg concentrations and sampling procedure in different heights from the orifice for individual vents fluids in Rainbow, Broken Spur and Lost City hydrothermal fields (FTD: Fumeur Tres Dense; FN: Fumeur Nouveau)

Vent Field	Temperature (°C)	Minimum pH	Minimum Mg	Sampling (m above orifice)
Rainbow				
FTD	315	-	7.58	0, 0.3, 2, 3, 5, 12
FN	320	3.04	2.34	0, 0.2, 1.5, 4, 7
Magali	372	3.10	7.44	0, 0.1, 1, 2, 3, 5
Broken Spur				
Spire	310	3.47	3.19	0, 0.1, 1, 2, 5
Dragon	332	3.02	5.57	0, 0.1, 1.5
Chandelier	-	3.01	5.83	0, 0.1, 1, 3
Lost City				
Marker B	84	10.32	4.7	0

3.2.2 Mg and SO_4

Endmember concentrations of Mg and SO_4 in hydrothermal fluids are expected to be near zero because of nearly total removal of Mg and SO_4 in hydrothermal fluids during high temperature water-rock reactions with mafic and ultramafic rocks (Bischoff and Dickson, 1975; Moitl and Holland, 1978; Seyfried and Bischoff, 1981; Janecky and Seyfried, 1986; Seyfried et al., 2007). However, measured Mg and SO_4 concentrations in Rainbow, Broken Spur and Lost City vent fluids were highly variable (both close to zero or higher) and lower than background seawater values (e.g. $Mg_{seawater}$: 52.6 mmol/kg and $SO_{4seawater}$: 28.2 mmol/kg). For example,

minimum Mg concentration in Rainbow fluids was measured as 2.34 mmol/kg in Fumeur Nouveau while it had a maximum value of 42.76 mmol/kg in one of the samples from Fumeur Tres Dense (Table 3.2). Additionally, sulfate concentrations in the Rainbow vent fluids exhibit a similar trend with Mg. Minimum and maximum sulfate concentrations were measured as 0.71 mmol/kg in Fumeur Nouveau and 22.74 mmol/kg in Fumeur Tres Dense, respectively (Table 3.2). Furthermore, high temperature Broken Spur vent fluids follow a similar variation with a slightly narrower concentration range for both species. For example, Mg and SO_4 concentrations in Spire vent fluids ranged from 3.19 mmol/kg to 33.81 mmol/kg and 1.87 mmol/kg to 19.47 mmol/kg, respectively (Table 3.2). In Dragon, measured Mg concentrations in vent fluids were in between 5.57 mmol/kg and 22.91 mmol/kg while measured SO_4 concentrations changed between 2.88 mmol/kg and 12.03 mmol/kg. Additionally, Chandelier vent fluids had similar concentrations and it was 5.83 – 18.69 mmol/kg for Mg and 3.21 – 10.16 mmol/kg for SO_4. On the other hand, there were only two high temperature focused fluid samples obtained from Lost City vent field and their Mg and SO_4 concentrations were 4.70 - 16.31 mmol/kg and 5.74 - 13.80 mmol/kg, respectively. By using these results, endmember SO_4 concentrations for each individual vent was calculated with least-squares regression method weighted to pass through the background seawater composition and extrapolated to 0 mmol/kg Mg concentration (Figure 3.2). According to this calculation, endmember SO_4 concentrations of Fumeur Tres Dense, Fumeur Nouveau and Magali vent fluids were -0.7 mmol/kg, -0.7 mmol/kg and 0.4 mmol/kg, respectively while they were 1.1 mmol/kg, 0 mmol/kg and 0.1 mmol/kg for Spire, Dragon and Chandelier, respectively (Table 3.3). Negative endmember dissolved sulfate values might reflect precipitation of dissolved sulfate as alkaline earth sulfate minerals in the subsurface (Von Damm, 2000). Lost City vent fluid had the highest endmember SO_4 concentration with respect to Rainbow and Broken Spur fluids and it was calculated as 4.9 mmol/kg.

Table 3.2 Measured concentrations of dissolved species for Rainbow, Broken Spur and Lost City hydrothermal vent fluids (FTD: Fumeur Tres Dense; FN: Fumeur Nouveau)

Vent Field	Mg (mmol/kg)	SO_4 (mmol/kg)	Cl (mmol/kg)	Br (µmol/kg)	Li (µmol/kg)
Rainbow					
FTD	42.76	22.74	592.38	959.82	109.57
	7.58	3.07	738.40	1096.17	332.42
	38.84	21.87	-	950.21	118.85
FN	2.34	0.71	788.26	1140.21	388.13
	39.23	22.00	580.58	885.83	100.28
	29.21	14.48	-	992.01	193.14
Magali	9.83	4.69	736.14	1045.43	308.28
	7.44	4.57	-	1210.87	326.09
	29.10	16.87	-	930.49	246.86
Broken Spur					
Spire	3.19	1.87	319.07	487.06	635.13
	33.81	19.47	-	750.38	271.14
	24.14	14.74	-	659.78	510.31
	28.78	15.41	483.54	748.14	410.86
Dragon	6.49	3.56	413.33	705.23	864.12
	5.57	2.88	418.56	610.00	774.41
	6.86	3.60	382.50	607.32	783.70
	22.91	12.03	-	718.19	621.20
Chandelier	5.83	3.21	442.12	714.84	937.83
	9.25	5.01	469.30	678.96	790.20
	18.69	10.16	-	743.45	673.20
Lost City					
Marker B	16.31	13.80	595.87	816.09	33.43
	4.70	5.74	494.60	927.63	39.00
Seawater	52.6	28.2	546.0	838.0	26.0

Table 3.2 (continued)

Vent Field	Na (mmol/kg)	K (mmol/kg)	Ca (mmol/kg)	Si (mmol/kg)
Rainbow				
FTD	520.86	12.40	22.97	1.52
	572.11	17.23	56.68	6.87
	524.65	12.18	23.81	1.51
FN	601.17	18.80	64.71	7.44
	485.82	11.38	20.85	1.70
	543.51	14.59	36.15	3.92
Magali	553.87	16.67	53.48	6.67
	598.18	16.58	53.12	6.67
	558.10	16.80	45.35	3.62
Broken Spur				
Spire	270.61	10.73	9.41	6.31
	396.42	10.26	8.99	5.09
	325.82	11.97	10.87	3.54
	419.65	11.72	10.95	6.92
Dragon	382.44	14.99	9.54	5.08
	323.23	12.90	13.34	4.76
	341.20	12.99	11.25	6.21
	409.46	13.64	13.19	7.84
Chandelier	393.29	14.84	14.59	4.99
	366.85	13.81	13.99	8.99
	419.26	13.79	15.31	7.75
Lost City				
Marker B	394.73	7.74	15.15	0.48
	453.95	8.51	21.30	0.50
Seawater	464.0	9.9	10.6	0.3

3.2.3 Other Non-Volatile Dissolved Species

Rainbow, Broken Spur and Lost City hydrothermal fluids exhibit variations in Cl, Br, Li, Ca, K, Na and Si concentrations (Table 3.2) and chemical measurement results regarding these elements were used to calculate endmember concentration of vent fluids. Endmember concentrations of non-volatile dissolved species are crucial to understand the formation and evolution of hydrothermal fluids. In other words, it is possible to interpret overall water-rock reactions happening in the sub-seafloor by using endmember fluid compositions. Furthermore, most of the cations in hydrothermal fluids are transported with Cl as chloro-complexes (Von Damm, 1990) since Cl is the dominant anion in hydrothermal vent fluids and hence changes in Cl concentration control changes in concentration of dissolved cations. Therefore, normalizing other major chemical species with respect to Cl concentration is a convenient and informative way in addition to interpreting absolute endmember concentrations of hydrothermal fluids in order to identify enrichments and depletions relative to ambient seawater (e.g. Gallant and Von Damm, 2006; Mcdermott et al., 2018). As a result, both endmember concentrations of Cl, Br, Li, Ca, K, Na and Si and their normalized counterparts with respect to Cl are represented in this section for Rainbow, Broken Spur and Lost City vent fluids individually.

3.2.3.1 Rainbow Hydrothermal Vent Field

Concentrations of endmember major and minor dissolved species in high temperature hydrothermal fluids obtained from Rainbow hydrothermal field showed close proximity to each other between individual vents (Figure 3.2). For example, endmember Cl concentrations were calculated as 772 mmol/kg for Fumeur Tres Dense, 792 mmol/kg for Fumeur Nouveau and 780 mmol/kg for Magali vents (Table 3.3). These results showed that endmember Cl concentrations in Rainbow fluids were much greater than seawater Cl concentration ($Cl_{seawater}$: 546 mmol/kg) up to 45%.

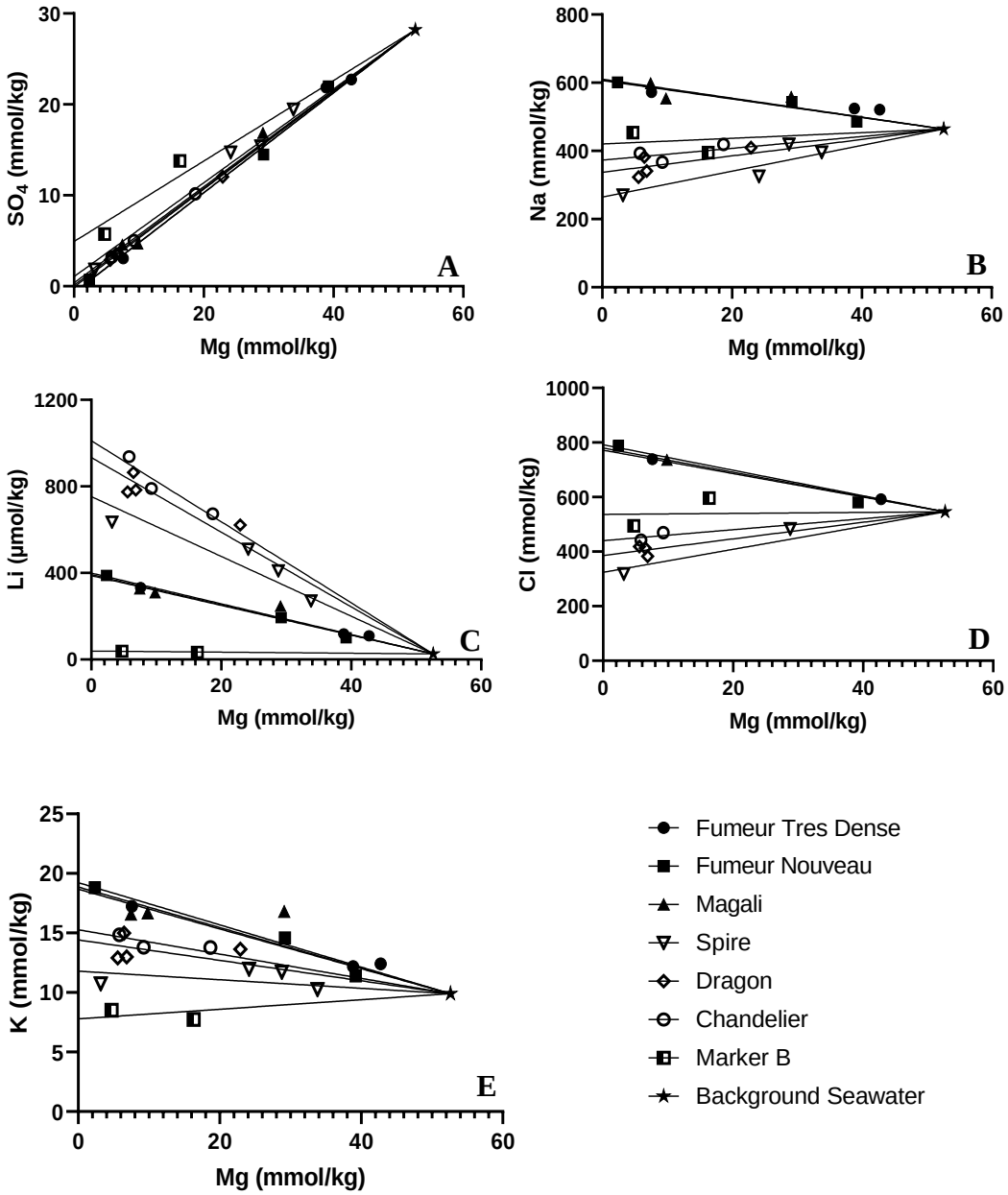

Figure 3.2. Measured Mg versus SO_4 (A), Na (B), Li (C), Cl (D), K (E), Br (F), Ca (G) for all high temperature fluid samples from Rainbow, Broken Spur and Lost City vent fields. Endmember concentrations are calculated by using least-squares regression method. Endmember concentrations are represented as solid lines. Black filled symbols are for Rainbow, open symbols are for Broken Spur and half filled symbol is for Lost City

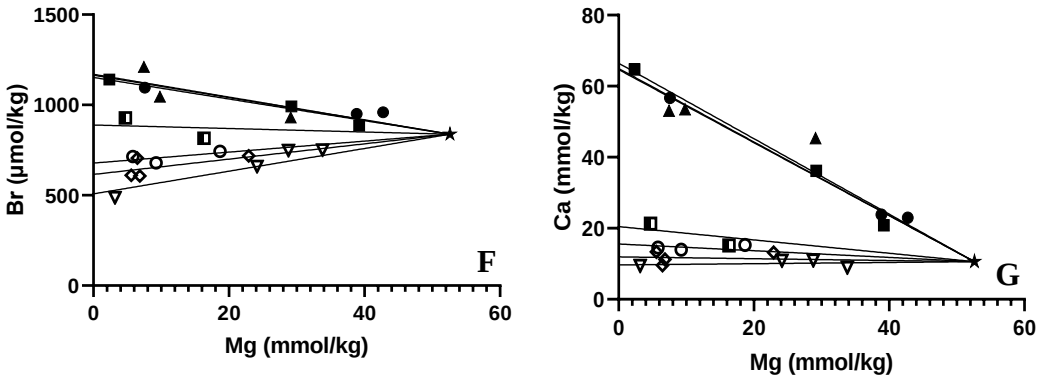

Figure 3.2. (continued)

Similar trend for Br was also present in Rainbow fluids. Endmember Br concentrations were calculated as 1165 µmol/kg in Fumeur Tres Dense, 1152 µmol/kg in Fumeur Nouveau, and 1170 µmol/kg in Magali high temperature vent fluids (Table 3.3). The average endmember Br concentration in Rainbow exhibited that Rainbow fluids had higher (~40%) Br concentrations with respect to ambient seawater ($Br_{seawater}$: 838 µmol/kg). Likewise, endmember Li concentration in Rainbow fluids was much higher than ambient seawater (Table 3.3). Calculated endmember Na concentrations were 606 mmol/kg, 610 mmol/kg, and 608 mmol/kg for Fumeur Tres Dense, Fumeur Nouveau and Magali, respectively. With these endmember concentrations, Rainbow fluids had greater Na up to ~31% relative to background seawater ($Na_{seawater}$: 464 mmol/kg). Endmember K concentrations were greater, as much as ~100%, relative to background seawater concentration in Rainbow fluids. Likewise, Rainbow fluids exhibited greater values in endmember Ca concentrations, which were calculated as 65 mmol/kg for Fumeur Tres Dense, 67 mmol/kg for Fumeur Nouveau, and 65 mmol/kg for Magali fluids (Table 3.3). Si was another important parameter to pay attention in vent fluid geochemistry. Endmember Si concentrations for Fumeur Tres Dense, Fumeur Nouveau and Magali were calculated as 7.7 mmol/kg, 7.8 mmol/kg, and 7.9 mmol/kg, respectively (Figure 3.3).

Table 3.3 Calculated endmember compositions for Rainbow, Broken Spur and Lost City hydrothermal vent fluids

Vent Field	**Cl (mmol/kg)**	**SO_4 (mmol/kg)**	**Br (µmol/kg)**	**Mg (mmol/kg)**
Rainbow				
Fumeur Tres Dense	772.0	-0.7	1165.0	0
Fumeur Nouveau	792.0	-0.7	1152.0	0
Magali	780.0	0.4	1170.0	0
Broken Spur				
Spire	324.0	1.1	508.0	0
Dragon	386.0	0.0	615.0	0
Chandelier	440.0	0.1	678.0	0
Lost City				
Marker B	537.0	4.9	890.0	0
Bottom Seawater	546	28.2	838	52.6

Vent Field	**Li (µmol/kg)**	**Na (mmol/kg)**	**K (mmol/kg)**	**Ca (mmol/kg)**
Rainbow				
Fumeur Tres Dense	388.0	606.0	18.7	65.0
Fumeur Nouveau	400.0	610.0	19.2	67.0
Magali	393.0	608.0	18.9	65.0
Broken Spur				
Spire	753.0	265.0	11.8	10.0
Dragon	934.0	337.0	14.4	12.0
Chandelier	1011.0	373.0	15.3	16.0
Lost City				
Marker B	39.0	420.0	7.8	21.0
Bottom Seawater	26	464	9.9	10.6

Background seawater Si concentrations was around 0.2 mmol/kg therefore, high temperature Rainbow fluids contained very high amount of Si with respect to background seawater (Table 3.3). Furthermore, seawater Na/Cl, K/Cl, Ca/Cl, Li/Cl and Br/Cl ratios were calculated as 0.85, 0.018, 0.019, 0.05, and 1.53, respectively (Table 3.4). In general, ratio of cations to Cl in Rainbow fluids exhibited relatively homogenous distribution among each individual vent. For example, Na/Cl ratio was 0.78, 0.77, and 0.78 for Fumeur Tres Dense, Fumeur Nouveau and Magali, respectively, and they were all much lower than ambient seawater Na/Cl ratio. Similar trend could be seen in Br/Cl ratios in Rainbow fluids, they also indicated relative depletions with respect to ambient seawater Br/Cl ratio (Table 3.4). All other ratios of cations to Cl showed relative enrichments when compared to seawater. For example, Ca/Cl ratios were calculated as 0.084 for Fumeur Tres Dense, 0.085 for Fumeur Nouveau and 0.083 for Magali. Likewise, K/Cl ratios in Rainbow fluids were calculated as 0.024 and Li/Cl ratios were 0.50- 0.51 for each individual vent in Rainbow hydrothermal field (Table 3.4).

3.2.3.2 Broken Spur Hydrothermal Vent Field

High temperature Broken Spur fluids obtained from Spire, Dragon, and Chandelier vents had relatively diverse concentrations in the case of major and minor dissolved species (Figure 3.2). For example, endmember Cl concentrations were calculated as 324 mmol/kg, 386 mmol/kg and 440 mmol/kg for Spire, Dragon and Chandelier, respectively. It can be seen that Broken Spur vent fluids had lower Cl concentrations (up to 41%) relative to ambient seawater ($Cl_{seawater}$: 546 mmol/kg). In addition to endmember Cl concentrations, a similar decreasing trend relative to starting seawater composition for Br and Na concentrations was present in Broken Spur fluids. Endmember Br concentrations were calculated as 508 µmol/kg for Spire, 615 µmol/kg for Dragon and 678 µmol/kg for Chandelier while Na concentrations of Broken Spur fluids were 265 mmol/kg, 337 mmol/kg, 373 mmol/kg for Spire, Dragon and Chandelier, respectively (Table 3.3). Therefore, Broken Spur fluids had

relatively lower Br concentrations (up to 40%) and Na (up to 43%) concentrations with respect to background seawater. On the other hand, endmember Li concentrations were much higher than ambient seawater concentrations. For example, endmember Li concentration of Spire fluids was 753 μmol/kg while it was 934 μmol/kg in Dragon fluids. Chandelier, on the other hand, had the highest endmember Li concentration among other vent fluids and it was calculated as 1011 μmol/kg. In addition, endmember K concentrations were relatively higher and showed much more homogenous trend among each individual vent. It was calculated as 14.4 mmol/kg for Dragon and 15.3 mmol/kg for Chandelier fluids while Spire fluids had 11.8 mmol/kg and Broken Spur vent fluids had greater K (up to 56%) with respect to background seawater (Table 3.3). Endmember Ca concentrations of Broken Spur fluids exhibited both higher and similar values with respect to background seawater values ($Ca_{seawater}$: 10.3 mmol/kg) and they were calculated as 10 mmol/kg for Spire, 12 mmol/kg for Dragon and 16 mmol/kg for Chandelier fluids (Table 3.3). Endmember dissolved silica concentration of Broken Spur vent fluids were calculated as 8.3, 7.0 and 8.9 mmol/kg for Spire, Dragon and Chandelier vents, respectively (Figure 3.3).

Moreover, values obtained by normalization to Cl concentration in Broken Spur fluids showed relative enrichments and depletion for different dissolved species with respect to starting seawater composition. For example, Na/Cl ratio in Broken Spur fluids was calculated as 0.82 for Spire, 0.87 for Dragon and 0.85 for Chandelier ($Na/Cl_{seawater}$: 0.85). On the other hand, Br/Cl ratios indicated that Spire and Dragon showed relative enrichment while Chandelier showed similar value with respect to seawater (Table 3.4). Moreover, K/Cl ratios were 0.036, 0.037 and 0.035 for Spire, Dragon and Chandelier fluids, respectively and they showed relative enrichments relative to seawater ($K/Cl_{seawater}$: 0.019). Also, relative enrichment was observed in Li, too. Since Broken Spur fluids had one of the highest Li concentrations observed in Mid-Atlantic Ridge vent fluids (e.g. Charlou et al., 2010), normalization of Li to Cl exhibited much higher value than ambient seawater. Li/Cl ratio was calculated in between 2.30 and 2.42 whereas seawater Li/Cl is around 0.05 (Table 3.4).

Table 3.4 Cl normalized elemental ratios calculated from endmember fluid composition at Rainbow, Broken Spur and Lost City hydrothermal fields. Indicated units are as follows mM: mmol/kg and μM: μmol/kg

Vent Field	**Na/Cl**	**K/Cl**	**Ca/Cl**	**Li/Cl**
Units	mM/mM	mM/mM	mM/mM	μM/mM
Rainbow				
Fumeur Tres Dense	0.78	0.024	0.084	0.50
Fumeur Nouveau	0.77	0.024	0.085	0.51
Magali	0.78	0.024	0.083	0.50
Broken Spur				
Spire	0.82	0.036	0.031	2.32
Dragon	0.87	0.037	0.031	2.42
Chandelier	0.85	0.035	0.036	2.30
Lost City				
Marker B	0.78	0.015	0.039	0.07
Bottom Seawater	0.85	0.018	0.019	0.05
Vent Field	**Br/Cl**	**Fe/Mn**	**Fe/Cl**	**Mn/Cl**
Units	μM/mM	μM/μM	μM/mM	μM/mM
Rainbow				
Fumeur Tres Dense	1.51	12.71	29.004	2.281
Fumeur Nouveau	1.45	12.77	25.621	2.006
Magali	1.50	12.87	26.391	2.050
Broken Spur				
Spire	1.57	1.78	1.762	0.991
Dragon	1.59	1.90	1.759	0.925
Chandelier	1.54	2.86	2.032	0.711
Lost City				
Marker B	1.66	-	-	-
Bottom Seawater	1.53	<1	<0.001	<0.001

However, although Ca exhibited such enrichments, it was not as drastic as Li. Ca/Cl ratios in Broken Spur were calculated in between 0.031- 0.036 for each vent fluid while Ca/Cl ratio was around 0.019 for ambient seawater.

3.2.3.3 Lost City Hydrothermal Vent Field

Endmember fluid composition of non-volatile dissolved species were calculated for high temperature fluid samples obtained from Marker B vent in the Lost City hydrothermal field (Figure 3.2). Concentration of all chemical species had close proximity with ambient seawater values in Marker B vent. For example, endmember Cl, Na and K concentrations were calculated as 537 mmol/kg, 420 mmol/kg, and 7.8 mmol/kg, respectively and Marker B fluids had slightly lower amount of Cl (~2%), Na (~10%) and K (~20%) in its endmember composition (Table 3.3). Additionally, a similar trend could be seen in Br concentration as well, however, in that case it exhibited slightly higher concentration value by only ~6% with respect to ambient seawater. Endmember Br concentration was calculated as 890 μmol/kg while seawater Br was 838 μmol/kg. On the other hand, endmember Li and Ca concentrations were calculated as 39 μmol/kg and 21 mmol/kg, respectively and they showed greater concentrations (e.g. 50% for Li and 76% for Ca) with respect to ambient seawater. Moreover, endmember Si concentration for Lost City was able to be calculated as 0.5 mmol/kg. It had a concentration approximately three-times of ambient seawater concentration (e.g. $Si_{seawater}$: <0.2 mmol/kg).

Furthermore, values obtained by normalization to Cl concentration in Lost City fluid showed relative enrichments and depletion for different dissolved ion species with respect to starting seawater composition. For example, Na/Cl and K/Cl ratios were calculated as 0.78 and 0.015, respectively and showed relative depletion with respect to seawater ratios while Ca, Li and Br showed relative enrichments with respect to corresponding seawater ratios (Table 3.4).

3.2.4 Transition Metals and $\sum H_2S$

Measured concentrations of dissolved transition metals including Fe, Mn, Cd, Co, Cu, Ni, Al, and Zn obtained from Rainbow and Broken Spur hydrothermal fluids show large enrichments with respect to ambient seawater concentrations. However, endmember concentrations of many metals except Fe and Mn could not be calculated since they do not exhibit linear correlation with Mg. This might be due to variable degree of uncertainty seen in transition metals in hydrothermal vents because most of these metals might precipitate both in subseafloor and fluid samplers, which limits the detection of any linear relationship with magnesium (see Yucel et al., 2011; McDermott et al., 2018). In addition, all metal concentrations obtained from Lost City hydrothermal fluids are below the limit of detection, hence no analysis is presented for Lost City fluids other than confirming the earlier findings that the site is low in metal fluxes and a hydrogen and hydrocarbon fluxes dominated.

Table 3.5 Calculated endmember compositions of Fe, Mn, Si and H_2S for Rainbow, Broken Spur and Lost City hydrothermal vent fluids

Vent Field	**Fe (µM)**	**Mn (µmol/kg)**	**Si (mmol/kg)**	**$\sum H_2S$ (mM)**
Rainbow				
Fumeur Tres Dense	25881	1761	7.7	-
Fumeur Nouveau	26533	1589	7.8	-
Magali	24024	1599	7.9	-
Broken Spur				
Spire	571.0	321.0	8.3	5.72
Dragon	679.0	357.0	7.0	6.56
Chandelier	894.0	313.0	8.9	5.82
Lost City				
Marker B	-	-	0.5	-
Bottom Seawater	<0.001	<0.001	0.3	0

Endmember concentrations of Fe for Rainbow fluids are calculated as 25881 µmol/kg, 26533 µmol/kg, 24024 µmol/kg for Fumeur Tres Dense, Fumeur Nouveau and Magali vents, respectively (Figure 3.3). On the other hand, Broken Spur has relatively much lower endmember Fe concentrations and they are calculated as 571 µmol/kg, 679 µmol/kg and 894 µmol/kg for Spire, Dragon and Chandelier vents, respectively (Table 3.5). Both hydrothermal vent fields are following a similar trend in the case of endmember Mn concentrations as well. That is, Mn concentrations for Rainbow vents are in between 1590-1761 µmol/kg while they are much lower (313-357 µmol/kg) in Broken Spur fluids (Table 3.5). The Cl normalization that have been performed for major and minor dissolved species can be applied to Fe and Mn in order to check the relative differences between individual vent fluids although both Fe and Mn concentrations already indicate great enrichments with respect to ambient seawater. In that respect, Fe/Cl and Mn/Cl ratios are calculated very close to each other as 29.0, 25.6 and 26.4 and 2.3, 2.0, and 2.1 for Fumeur Tres Dense, Fumeur Nouveau, and Magali vents, respectively (Table 3.4). Although endmember Cl concentration is so high in Rainbow fluids, the highest ever measured endmember Fe and one of the highest Mn concentrations in Rainbow fluids are responsible in creating very high Fe/Cl and Mn/Cl ratios. Relatively higher variation in endmember Fe, Mn and Cl concentrations seen in Broken Spur fluids create relatively higher differences in Fe/Cl and Mn/Cl ratios between individual vents. For example, Mn/Cl ratios for Spire and Dragon are very close to each other however relatively higher endmember concentrations of Cl and lower concentration of Mn calculated in Chandelier fluids creates lower Mn/Cl ratio relative to other Broken Spur vents (Table 3.4). Additionally, Fe/Cl ratios are relatively more dispersed with respect to each other in Broken Spur fluids. Moreover, results of $\sum H_2S$ ($\sum H_2S = H_2S + HS^- + S^{2-}$) measurements could only be obtained for some of Broken Spur fluids, and they are used to calculate overall endmember concentrations for individual Broken Spur vents. On the other hand, $\sum H_2S$ concentrations are below the limit of detection in Rainbow and Lost City vent fields (see Le Bris and Duperon, 2010).

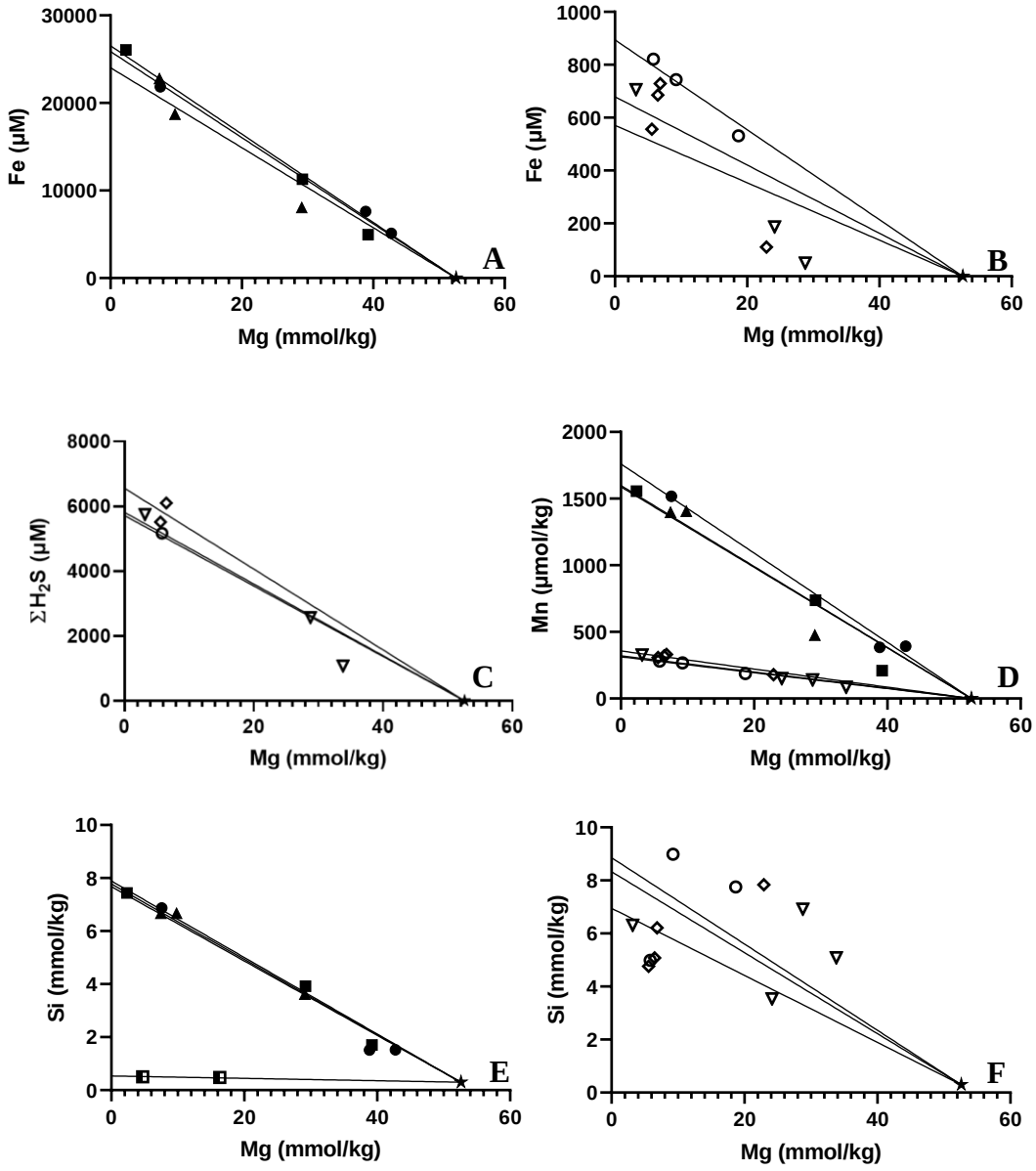

Figure 3.3. Measured Mg versus Fe (A, B), $\sum H_2S$ (C), Mn (D), Si (E, F) plots for all high temperature fluid samples where appropriate from Rainbow, Broken Spur and Lost City vent fields. Endmember concentrations are calculated by using least-squares regression method and represented as solid lines. Black filled symbols are for Rainbow (Circle: Fumeur Tres Dense, Square: Fumeur Nouveau, Triangle: Magali), open symbols are for Broken Spur (Inverted Triangle: Spire, Diamond: Dragon, Circle: Chandelier) and half-filled square is for Marker B, Lost City

Table 3.6 Table showing standart error values of slope and Y-intercepts for each endmember chemical species obtained by using regression plots in Figure 3.2 and Figure 3.3 for Rainbow (Fumeur Tres Dense, Fumeur Nouveau, Magali), Broken Spur (Spire, Dragon, Chandelier) and Lost City (Marker B) vent fluids (units are same as the regression plots)

Chemical Species	**Uncertainty**	**Fumeur Tres Dense**	**Fumeur Nouveau**	**Magali**
Cl	Slope	0.09	0.55	-
	Y-intercept	4.82	29.19	-
Na	Slope	0.60	0.26	0.44
	Y-intercept	31.42	13.87	23.32
Br	Slope	1.03	0.44	1.29
	Y-intercept	53.92	22.91	67.91
Li	Slope	0.24	0.26	0.65
	Y-intercept	12.61	13.92	34.13
K	Slope	0.01	0.01	0.03
	Y-intercept	0.68	0.68	1.74
Ca	Slope	0.04	0.05	0.12
	Y-intercept	1.89	2.66	6.34
Si	Slope	0.01	0.01	0.00
	Y-intercept	0.60	0.38	0.14
Fe	Slope	13.66	24.56	37.52
	Y-intercept	718.30	1292.00	1973.00
Mn	Slope	1.45	2.49	2.79
	Y-intercept	76.46	131.20	146.80
SO_4	Slope	0.02	0.02	0.02
	Y-intercept	1.00	0.94	0.80
H_2S	Slope	-	-	-
	Y-intercept	-	-	-

Table 3.6 (continued)

Chemical Species	Uncertainty	Spire	Dragon	Chandelier	Marker B
Cl	Slope	0.77	0.26	0.23	1.18
	Y-intercept	40.55	13.87	11.85	61.96
Na	Slope	0.50	0.31	0.28	0.82
	Y-intercept	26.09	16.17	14.46	43.01
Br	Slope	0.70	0.53	0.34	1.19
	Y-intercept	36.85	27.83	17.67	62.66
Li	Slope	1.17	0.79	0.60	0.03
	Y-intercept	61.35	41.50	31.36	1.69
K	Slope	0.02	0.01	0.01	0.01
	Y-intercept	0.82	0.75	0.36	0.77
Ca	Slope	0.02	0.02	0.02	0.05
	Y-intercept	0.80	1.18	0.88	2.48
Si	Slope	0.04	0.03	0.04	0.00
	Y-intercept	1.89	1.49	1.99	0.02
Fe	Slope	3.38	2.18	0.52	-
	Y-intercept	177.60	114.60	27.17	-
Mn	Slope	0.40	0.22	0.17	-
	Y-intercept	20.90	11.61	8.72	-
SO_4	Slope	0.02	0.00	0.00	0.03
	Y-intercept	0.87	0.09	0.04	1.82
H_2S	Slope	12.63	7.54	-	-
	Y-intercept	664.50	396.50	-	-

3.3 Geochemistry of Rainbow and Broken Spur Hydrothermal Plumes

For a better contextual understanding of the mixing processes in the plume as well as assessing the mixing status of the samples, results of concentration ranges of different vent forming chemicals collected in different heights from the orifice (e.g. 0 m to 12 m in the plume) in Rainbow and Broken Spur hydrothermal vents are presented in this section. Plots of distance from the orifice versus temperature and

different dissolved chemical species measured in both vent fluids exhibited different trends for Rainbow and Broken Spur vent fields (Figure 3.3-3.8). For example, variable amount of Mg was seen in rising plume for each vent. Mg in hydrothermal fluids can be a good seawater mixing tracer since endmember Mg concentration of vent fluids is near zero while it is much higher (~52.6 mmol/kg) at ambient seawater. Therefore, Mg should gradually increase starting from the orifice throughout the rising plume in normal conditions. For example, Mg concentrations displayed expected depletion towards the orifice with a minimum of 6.9 mmol/kg measured at Dragon and 7.4 mmol/kg at Magali and increase up to ~48 mmol/kg for both vents at around 1.5 meters and 5 meters from the orifice (Figure 3.3 and Figure 3.8). However, variable amount of seawater entraining into major samplers during the sampling process may increase the Mg concentration more than expected and interrupt the trend of gradual increase. For example, in Dragon and Chandelier plumes, Mg profiles indicated a logarithmic shape implying a regular mixing curve while in Spire there in the first two samples near the orifice, we found strong indications of high fraction of seawater mixing just above the orifice. Similar trend was also present in Fumeur Tres Dense plume in Rainbow as well. Additionally, SO_4 displayed similar trend with Mg and its concentration increased as the plume rises (Figure 3.3). However, in some vent fluids such as Magali and Spire, SO_4 concentrations exceeded ambient seawater concentration (e.g. ~ 40 mmol/kg) up in the plume while other vents exhibited a trend converging ambient seawater SO_4 concentration. Further, “mirror image” like profiles of Mg and SO_4 (i.e. a decreasing trend from orifice to up in the rising plume) were expected for Fe, Mn and Si since their concentrations were so low in ambient seawater when compared to vent fluids. In other words, hydrothermal fluids act as a source for those chemical species. All profiles for each dissolved species in Rainbow and Broken Spur vents followed this trend as expected (Figure 3.3-3.8).

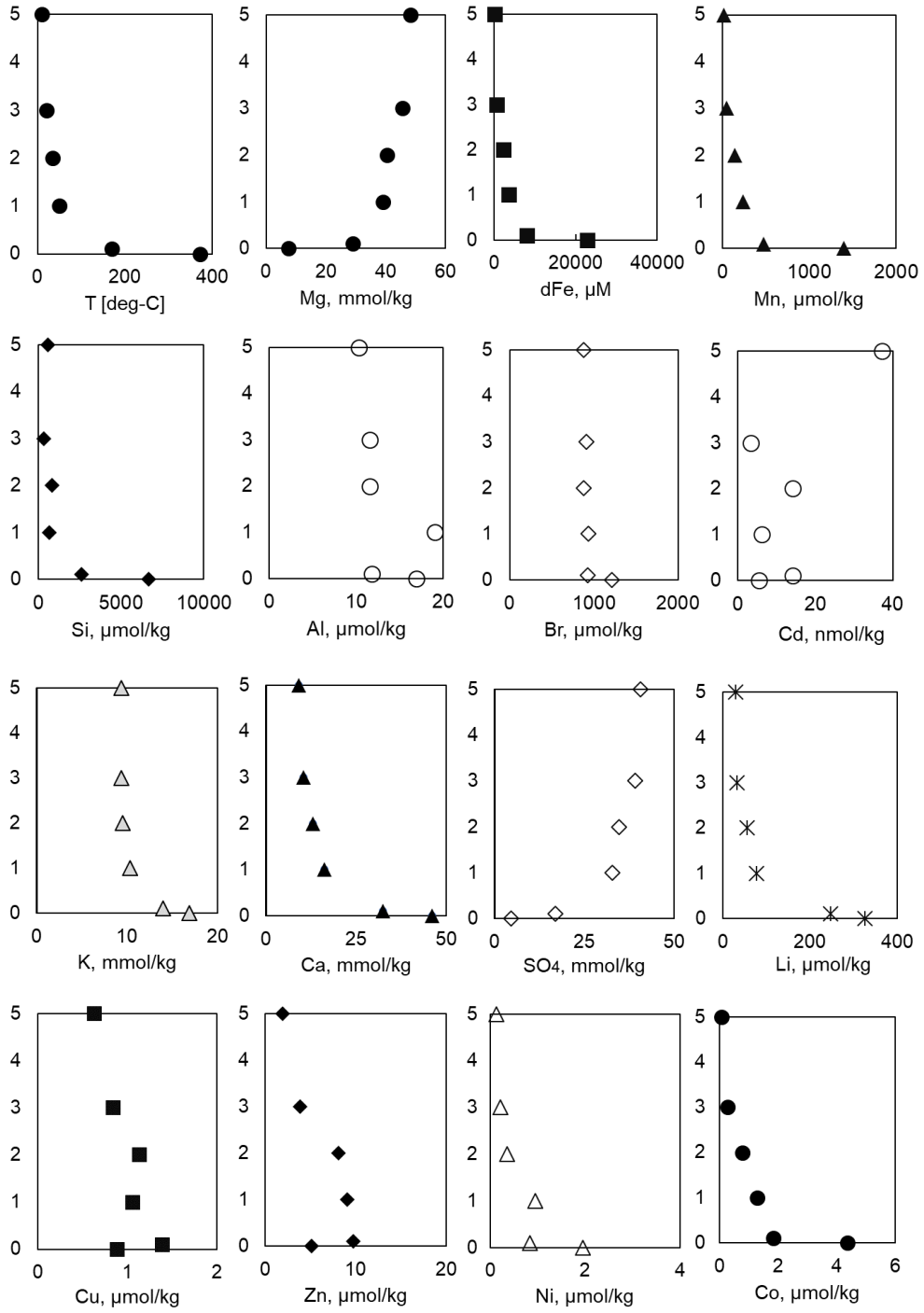

Figure 3.4. Evolution of temperature, Mg, Fe, Mn, Si, Al, Br, Cd, K, Ca, SO_4, Li, Cu, Zn, Ni, and Co in Magali rising plume, Rainbow hydrothermal vent field. Vertical axes represent distance from the orifice in meter

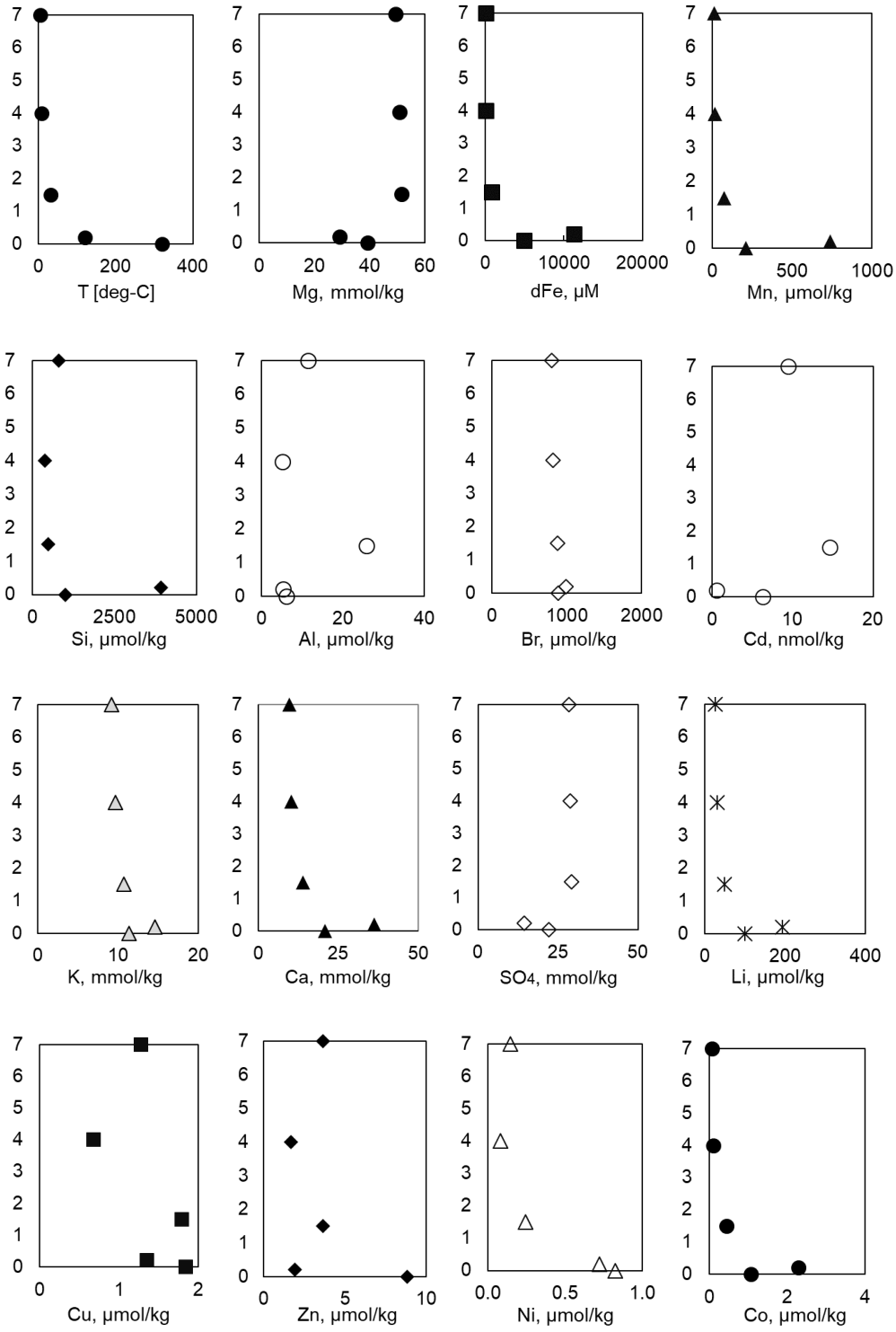

Figure 3.5. Evolution of temperature, Mg, Fe, Mn, Si, Al, Br, Cd, K, Ca, SO_4, Li, Cu, Zn, Ni, and Co in Fumeur Nouveau rising plume, Rainbow hydrothermal vent field. Vertical axes represent distance from the orifice in meter

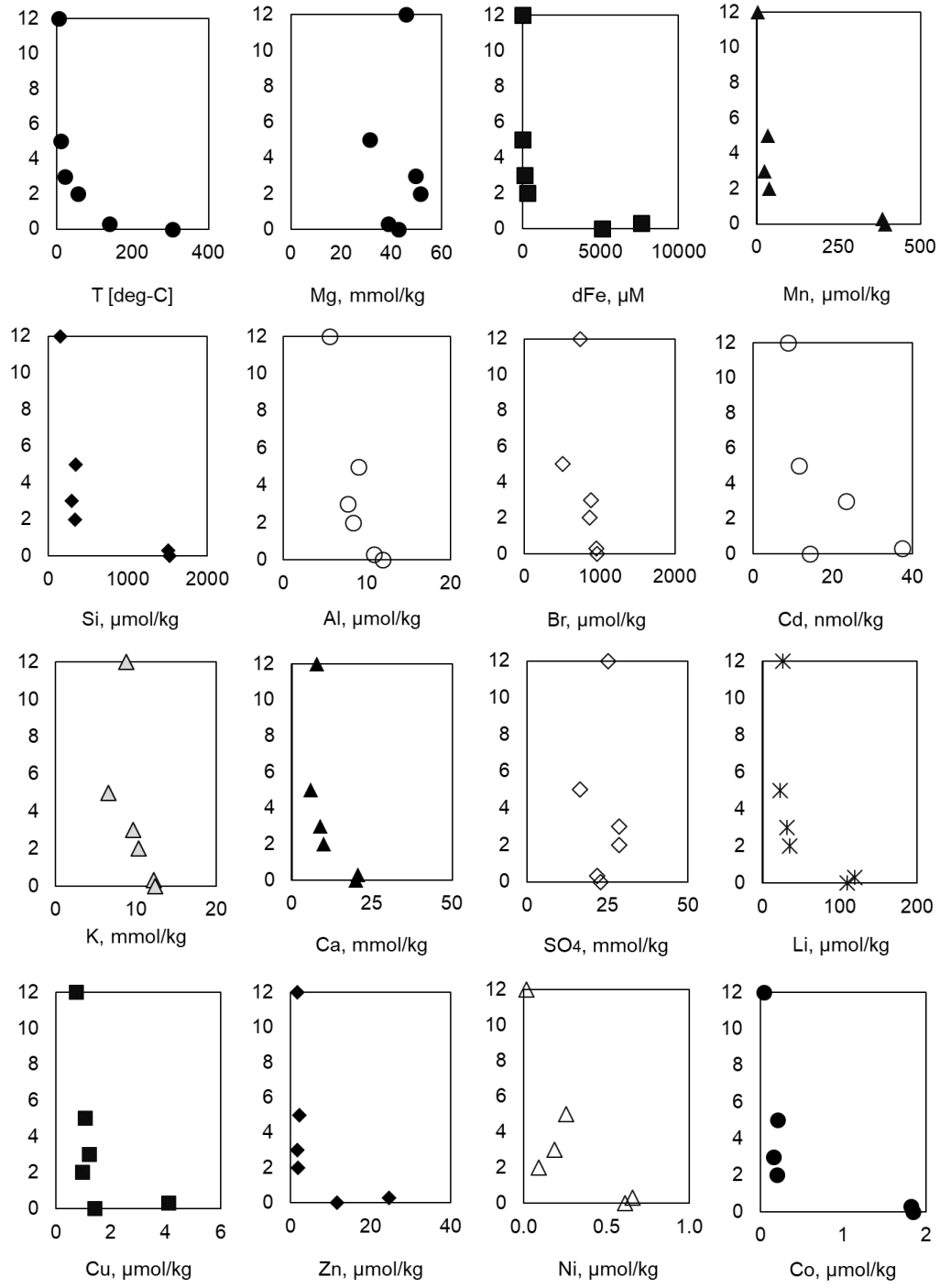

Figure 3.6. Evolution of temperature, Mg, Fe, Mn, Si, Al, Br, Cd, K, Ca, SO_4, Li, Cu, Zn, Ni, and Co in Fumeur Tres Dense rising plume, Rainbow hydrothermal vent field. Vertical axes represent distance from the orifice in meter

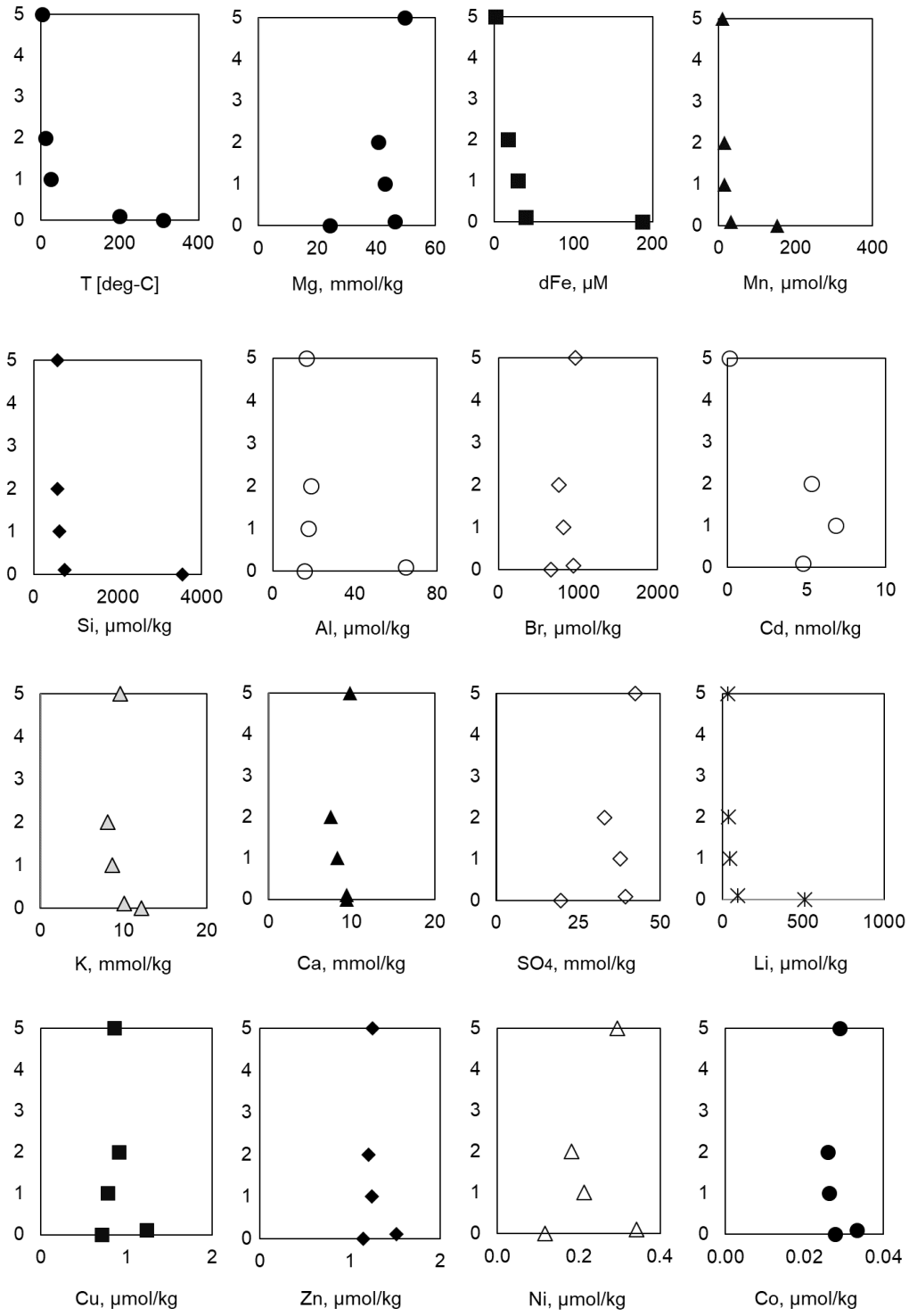

Figure 3.7. Evolution of temperature, Mg, Fe, Mn, Si, Al, Br, Cd, K, Ca, SO_4, Li, Cu, Zn, Ni, and Co in Spire rising plume, Broken Spur hydrothermal vent field. Vertical axes represent distance from the orifice in meter

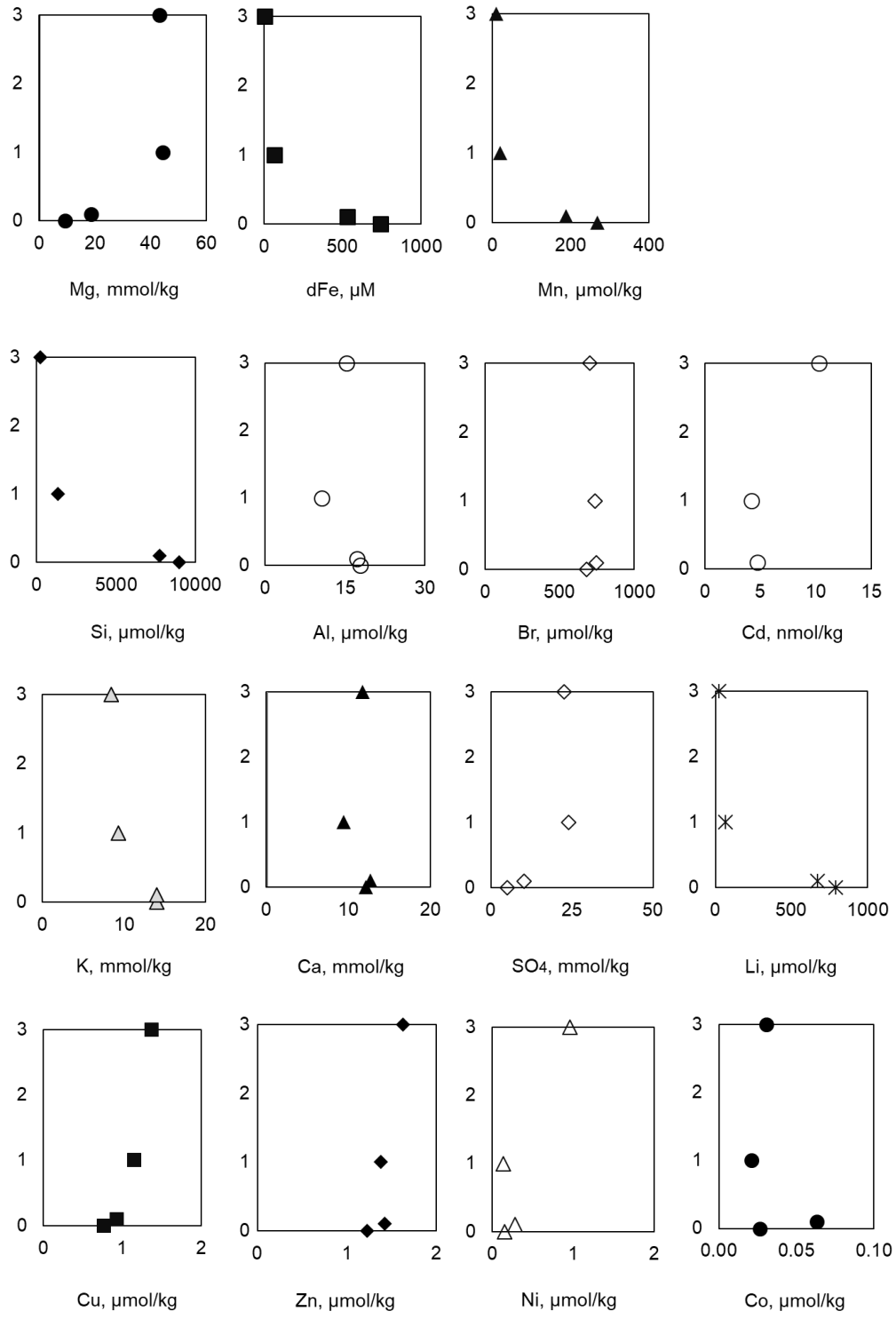

Figure 3.8. Evolution of Mg, Fe, Mn, Si, Al, Br, Cd, K, Ca, SO_4, Li, Cu, Zn, Ni, and Co in Chandelier rising plume, Broken Spur hydrothermal vent field. Vertical axes represent distance from the orifice in meter

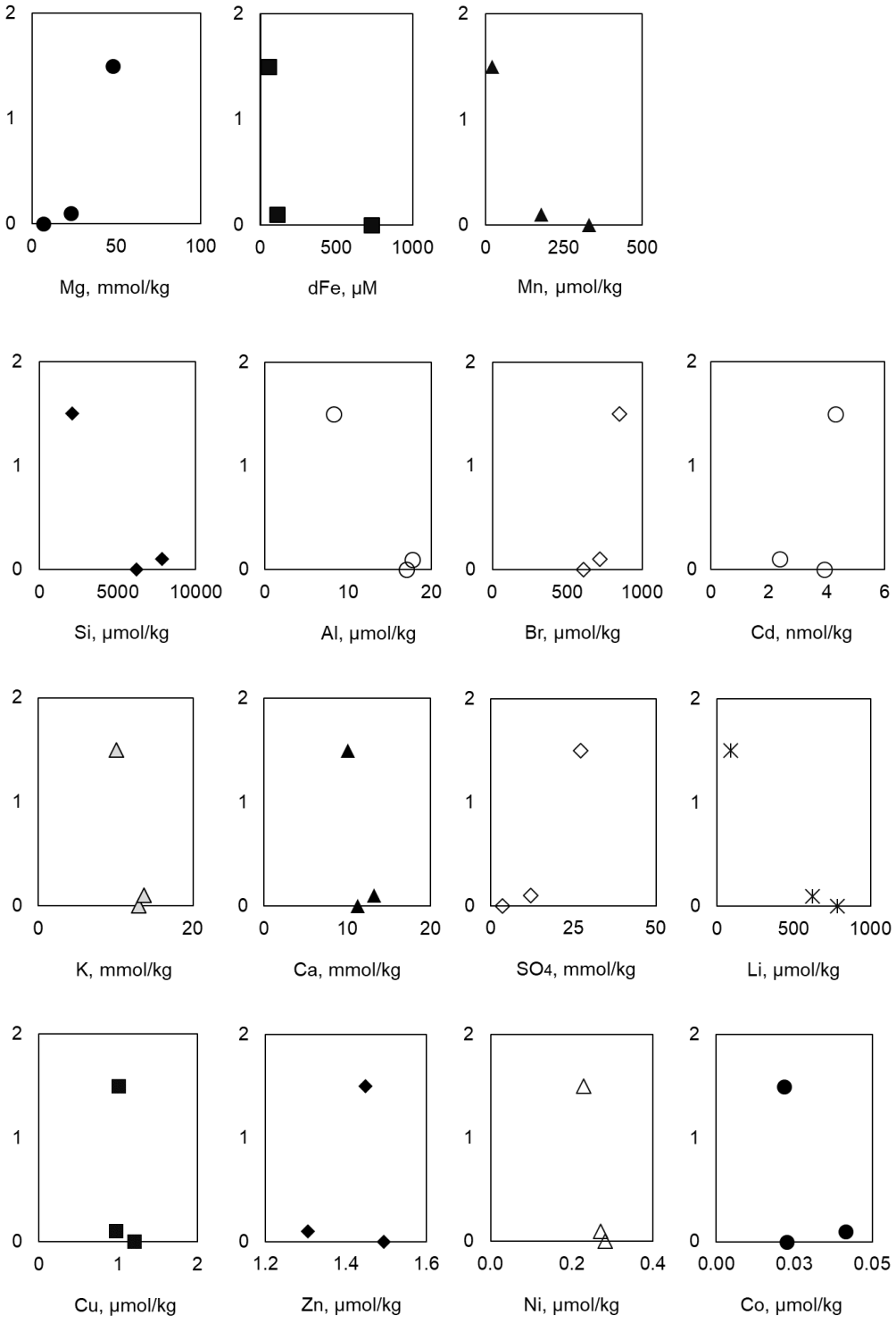

Figure 3.9. Evolution of Mg, Fe, Mn, Si, Al, Br, Cd, K, Ca, SO_4, Li, Cu, Zn, Ni, and Co in Dragon rising plume, Broken Spur hydrothermal vent field. Vertical axes represent distance from the orifice in meter

For example, maximum dissolved Mn was measured as 330 μmol/kg at the orifice of Dragon chimney at Broken Spur (Figure 3.8) while Spire and Chandelier chimneys still emited Mn levels around 200 μmol/kg. Profiles showed that approximately 15 μmol/kg level of Mn in average was still present in the plume of Broken Spur vents and it reached ~1.2 μmol/kg at 5 meters height above the Spire orifice. Silica released from the Broken Spur vents was high (maximum of 8991 μmol/kg of dissolved Si was measured in Chandelier) with a decreasing trend as fluid mix with seawater over the plume height. Additionally, several hundred μmol/kg dissolved Si was still present in the upper parts of the rising plume (e.g. 565 μmol/kg at 5 meters from Spire orifice and 262 μmol/kg at 3 meters from Chandelier orifice) and entered the deep ocean from Broken Spur vents. High temperature samples obtained from Broken Spur vent orifices showed a wide range of dissolved Fe concentrations as 187-744 μmol/kg by following the similar decreasing trend as fluids mix with seawater. However, minimum ~1.2 μmol/kg of dissolved Fe was still retained in the upper part of the Spire plume. Rainbow vents, on the other hand, had higher concentrations of Mn with respect to Broken Spur, however Mn concentrations in the upper part of the rising plumes resembled to Broken Spur (Figure 3.3-3.5). Maximum silica concentration at the high temperature fluids at the orifice was measured as 6670 μmol/kg and a maximum of 807 μmol/kg Si was still present at the 5-m height from the orifice. Mirroring the Si profiles in the Magali and Fumeur Nouveau plumes exhibited a continuous decrease as plume rises while extensive seawater mixing was present at Fumeur Tres Dense plume. Dissolved Fe concentration of Rainbow fluids were much higher than Broken Spur at high temperature samples at orifice, and they had a concentration range between around 5000- 8000 μmol/kg. However, variable amount of dissolved Fe was transported up in the buoyant plume in Rainbow vents. For example, we still had 80-100 μmol/kg of dissolved iron at 5 and 7 meters from the orifice for Magali and Fumeur Nouveau plumes, respectively while after around 3 meters from the orifice, no dissolved iron was persisted in the rising plume in Fumeur Tres Dense (Figure 3.5). Also, temperature profiles exhibited similar “mirror image” like trend when compared to

Mg and SO_4. Abrupt decrease of temperature can be seen in each vent profile due to the mixing of very high temperature hydrothermal fluids (305-372 °C) with cold ambient seawater (Figure 3.3-3.8)

Furthermore, in the case of other dissolved ions rather than Mg and SO_4 such as Br, K, Ca and Li, we observed slight or intense decreases in the upper part of the plume. For example, the most intense concentration decrease was seen in Li among these ions. It was maximum at Chandelier orifice (790 μmol/kg) and minimum at Spire orifice (510 μmol/kg) in Broken Spur vents and, for example, 32 μmol/kg of Li persist at 5 meters in the Spire plume. Rainbow vents had similar trend but much less Li concentrations. It was in between 100-326 μmol/kg at the orifice and around 26 μmol/kg in the upper part of the plume. Additionally, Br showed slightly conservative trends with small increases as the plume rises (Figure 3.3-3.8). Also, both Ca and K profiles generally showed decreasing trends. Both vent fields had similar K concentrations both in orifice and different plume heights, however, Rainbow fluids consisted much higher Ca at the orifice although Ca concentrations converged to ambient seawater values in higher part of the plume in both vent fields (Figure 3.3-3.5). For example, it was 46 mmol/kg at Magali orifice while 9.4 mmol/kg at Spire orifice however Ca concentrations were around 9.8 mmol/kg at the 5 meters of corresponding plumes.

It is hard to obtain accuratedissolved concentrations of transition metals other than Fe and Mn such as Cu, Ni, Zn, Co etc. since they readily tend to form precipitates in the samplers until their recovery (Trefry et al., 1994). Although recovered samples do not represent accurate dissolved fractions of these metals, still the measurements at least provide information about their minimum dissolved concentrations. Therefore, corresponding results were presented here to provide a general framework regarding behavior of these metals in the rising plume. Ni and Co profiles represented similar profiles with Fe and Mn in Rainbow vents. Maximum Ni and Co concentrations were measured as ~2.2 μmol/kg at Magali and Fumeur Nouveau orifices, respectively, and they both continuously decreased as plume rises and converging 0 μmol/kg for both species (Figure 3.3-3.5). On the other hand,

concentrations of Co and Ni were much less in Broken Spur fluids. Approximately 0.03 μmol/kg of Co and 0.3 μmol/kg of Ni were measured near the orifice in Broken Spur vents (Figure 3.6-3.8). Additionally, Cu and Zn profiles for both Rainbow and Broken Spur vents had commonalities regarding their trends, which indicated Cu and Zn might have similar behaviors in the plume. Both metals exhibited slight concentration decreases as fluids mix with ambient seawater (Figure 3.3-3.8). Finally, Cd did not show observable trends like other metals. Nano-molar level of Cd was measured in each vent. Rainbow had higher Cd concentrations than Broken Spur. For example, maximum Cd was detected as 37 nmol/kg in Fumeur Tres Dense orifice in Rainbow while it was 4 nmol/kg in Dragon orifice in Broken Spur.

CHAPTER 4

DISCUSSION

4.1 Processes Controlling Formation of Endmember Fluid Geochemistry

4.1.1 Phase separation and Cl variability

Rainbow and Broken Spur hydrothermal fluids exhibit relative enrichments and depletions of endmember Cl concentrations with respect to ambient seawater value (Table 3.3). Different processes have been thought to control Cl variation in hydrothermal fluids including hydration of igneous crust, dissolution or precipitation of Cl-bearing minerals during the water-rock reactions and phase separation. It was already showed in different studies that the phase separation has the most substantial effects on Cl concentrations among these processes in hydrothermal fluids in different settings existing in ultrafast, fast, slow spreading ridges and back-arc systems (Bischoff and Rosenbauer, 1985; Bischoff and Pitzer, 1989; Von Damm, 1988; Von Damm, 1990; Butterfield and Massoth, 1994; Butterfield et al., 1994; German and Von Damm, 2003; Foustoukos and Seyfried, 2007b). Phase separation depends on temperature and pressure conditions and it occurs when these conditions are proper during seawater circulation down through the oceanic crust. These two physical conditions are directly proportional to each other, meaning that greater depths need higher temperatures for phase separation of seawater. For example, seawater undergo phase separation at 389 °C at a typical intermediate to fast spreading mid-ocean ridge system at around 2500 meters while it requires 450°C for phase separation at around 4200 meters (see Figure 4.1) (Bischoff, 1991; Bischoff and Rosenbauer, 1985). Phase separation occurs when the temperature and pressure conditions of a solution crosses the vapor-liquid boundary (i.e. two-phase curve) of the NaCl–H_2O system (Bischoff and Rosenbauer, 1985). It will then separate into

two different phases with different chlorinities; (1) one with higher chlorinity, and (2) other with lower chlorinity relative to ambient seawater. For example, at Rainbow seafloor conditions (~227 bars), the vapor-liquid boundary of seawater is at around 385 °C, which is the minimum temperature at which fluids must have to initiate the phase separation below the seafloor (Figure 4.1). Likewise, measured exit temperatures of Broken Spur fluids lie well below the two-phase curve at seafloor pressures (~305 bars). Subseafloor conditions of Broken Spur need to have a temperature at least 405 °C to induce phase separation. Both of these calculations indicate that Rainbow and Broken Spur fluids are not actively phase separating at the seafloor with their current physical conditions.

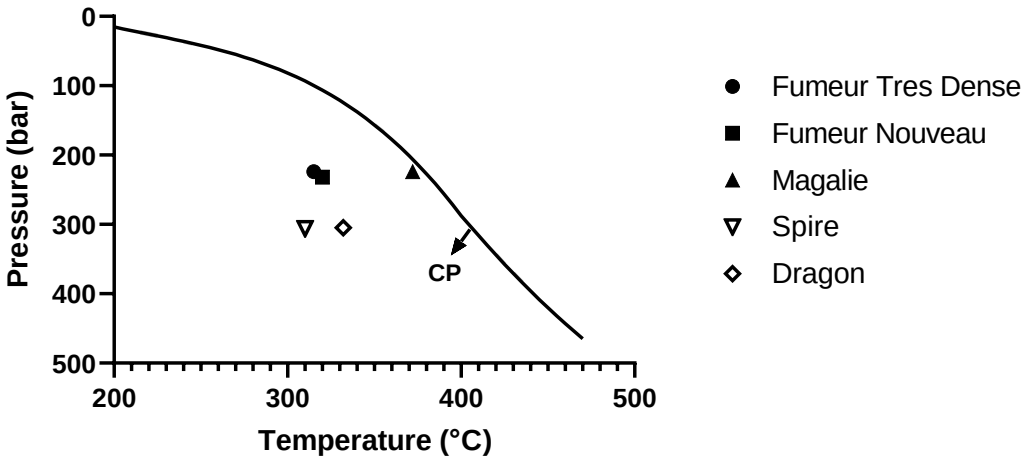

Figure 4.1. Temperature and Pressure properties of seawater with two-phase curve (solid line) (from Bischoff and Rosenbauer, 1985). CP indicates critical point of seawater at 407 °C and 298 bars. Seafloor P-T conditions for each individual Rainbow and Broken Spur vents are represented in the plot as well

Accordingly, it is possible to infer that both hydrothermal fluids might circulate to deeper portions (e.g. several kilometers) in the oceanic crust, and might have phase separations at even much higher temperatures discussed above. In that respect, endmember Cl concentrations of hydrothermal fluids and the character of phase separation are being used to determine the depth and temperature conditions of phase

separation in the subseafloor (e.g. Von Damm, 1995; Charlou et al., 2002; Gallant and Von Damm, 2006; Charlou et al.., 2010; Reeves et al., 2011; McDermott et al., 2018). Mainly, there are two different types of phase separation occurring in hydrothermal system and character of the phase separation is determined where fluid crosses the two-phase curve (German and Von Damm, 2003; Charlou et al., 2010). For example, if it crosses at pressure and temperature conditions higher than the critical point of a 3.2-wt % NaCl-H_2O solution (407°C, 298 bars) then supercritical phase separation (also called as condensation) occurs, where a liquid phase with relatively higher chlorinity condenses out of the fluid (Bischoff and Rosenbauer, 1984; (German and Von Damm, 2003; Charlou et al., 2010). On the other hand, if fluid crosses two-phase curve at conditions less than the critical point of seawater, it results in subcritical phase separation (or boiling), which creates low chlorinity vapor phase and this fraction can be emitted separately in hydrothermal vents.

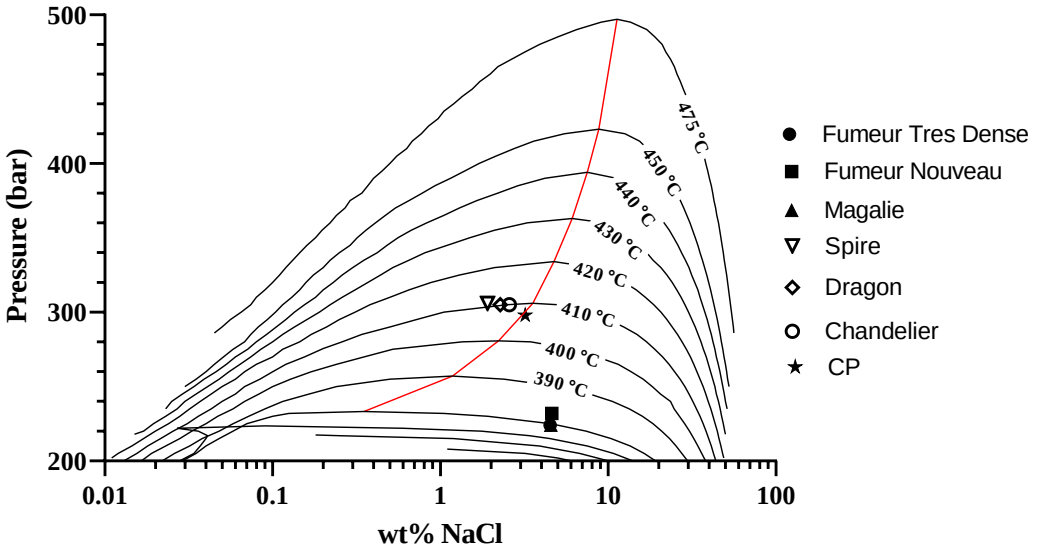

Figure 4.2. Isotherms of the vapor-liquid region and two-phase curve (red) of NaCl-H_2O from 390 °C to 475°C (modified from Bischoff and Pitzer (1989)). CP indicates critical point of 3.2 wt % seawater at 298 bars. Individual vent fields in Rainbow and Broken Spur are represented in the plot as well

This vapor phase can contain salt with varying amount depending on the point of intersection on the two-phase curve (Bischoff and Rosenbauer, 1988). On the basis of this approach, for example, chlorinity of Rainbow fluids (4.51- 4.62 wt% NaCl) can be produced if supercritical phase separation of seawater occurs at ~420 °C and ~340 bars (Figure 4.2). Considering the seafloor physical conditions for Rainbow fluids (~225 bars and 315-372°C), this calculation shows that phase separation might occur at a pressure which is ~115 bars greater than the seafloor pressure, approximately 1150 meters deep within the crust. These results for Rainbow are consistent with what Charlou et al. (2010) reported. Considering the exit temperature of Rainbow fluids from the orifice, phase separation temperature show that Rainbow fluids experience intense cooling (as much as 105 °C) in the up-flow zone. Furthermore, depth of phase separation can be calculated in the same manner for Broken Spur as well. Chlorinity of Broken Spur fluids is changing between 1.91 and 2.58 wt% NaCl. Therefore, in this condition, Broken Spur experiences a subcritical phase separation at 400-405 °C and 280-290 bars in the subseafloor. Considering the seafloor depth of Broken Spur vents (i.e. ~3050 meters), phase separation occurs approximately 150-300 meters above the seafloor level. This might not be a problem considering the geomorphology of Mid-Atlantic Ridge (see Introduction chapter). Charlou et al. (2010) reported a similar case for Logatchev 2 vent fluids, and stated that upper part of the ridge segment in MAR might be at 2450 meters in depth. Additionally, temperature condition during the phase separation imply that Broken Spur fluids have cooled up to 95 °C during the rising in the up-flow zone since exit temperature measured at the orifice are varying between 310-332 °C in Broken Spur. On the other hand, a similar frame is not drawn for Lost City since it does not exhibit intense phase separation like Broken Spur and Rainbow rather Lost City fluids contain slightly lower endmember Cl concentration (~10 mmol/kg) when compared to ambient seawater (Table 3.3). One of the main possible mechanisms creates this shift might be Cl removal as a result of serpentinization since some of the minerals such as serpentine group minerals and iowaite ($Mg_6Fe^{3+}_2(OH)_{16}Cl_2 \cdot 4H_2O$) exhibit Cl enrichments in their structures (Früh-Green et al., 2004; Bach et al., 2004; Sharp

and Barnes, 2004). Additionally, a second plausible mechanism responsible in Cl depletion in Lost City fluids might be dehydration of brucite and resultant dilution of Cl by releasing water (Seyfried et al., 2015). Lack of brucite in serpentinites from southern wall of the Atlantis Massif (Boschi et al., 2008) is a supporting the idea for brucite dehydration.

4.1.2 Geochemical Evolution of Other Non-Volatile Dissolved Species

Figure 4.3 states that there is a strong positive correlation between dissolved Mg and SO_4 concentrations and therefore subsurface geochemical behavior of these two-chemical species resembles with each other during hydrothermal circulation. Additionally, in normal conditions, quantitative removal of Mg and SO_4 is expected under high temperature water/rock reactions however we have measured variable concentrations of these species in high temperature hydrothermal fluids (Table 3.2). This might be due to entrainment of seawater into major samplers during the sampling procedure and/or filling of dead volume of the sampler prior to deployment (Von Damm et al., 1985; Von Damm, 2000).

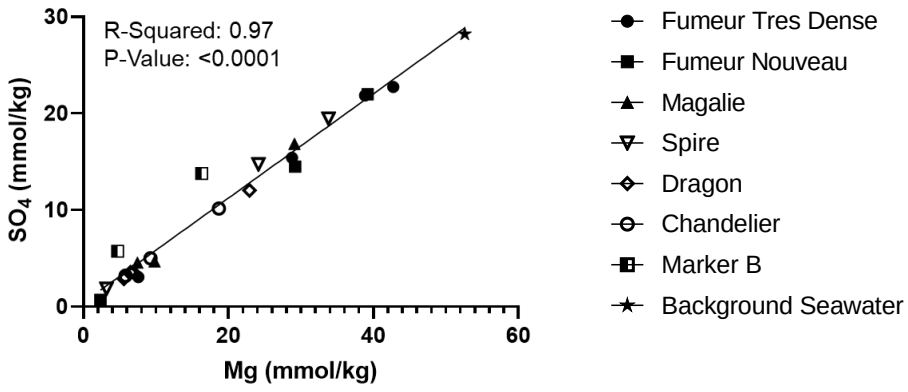

Figure 4.3. High positive correlation between Mg and SO_4 for samples from each individual vent in Rainbow, Broken Spur and Lost City hydrothermal fields. Statistical parameters are represented on the plot

Von Damm et al. (1985) showed that major samplers have a dead volume of ~4 ml and Seewald et al. (2002) calculated Mg contribution coming from same amount of dead volume (~ 4 ml) for another type of sampler (IGT) as 1.6 mmol/kg. Therefore, if we apply this calculation, major sampler dead volume can only explain roughly 1.6 mmol/kg of the measured Mg concentration. However, concentrations from all major samplers collected from Rainbow, Broken Spur and Lost City are greater than this value (Table 3.2). Moreover, such high Mg and SO_4 concentrations can also be explained by (1) hydrothermal fluids themselves might have high concentration of these two-chemical species under the control of specific set of geochemical reactions in the subsurface (e.g. Kleint et al., 2019) and/or (2) seawater might mix with hydrothermal fluids in the subsurface before releasing into seafloor (e.g. Gallant and Von Damm, 2006). In the first case, consistently high and similar Mg concentrations should have been obtained in replicate samples from same vent orifice but our dataset does not exhibit such a trend. In the second case, along with variable Mg and SO_4 concentrations, there might be a trend in decreasing temperature among individual vents due to mixing of ambient seawater (2 °C) with hydrothermal fluids (370-382 °C) in the subsurface (Gallant and Von Damm, 2006). Since our dataset represents such trends among individual Rainbow vents, the second case cannot be ruled out. Accordingly, negative endmember concentrations of SO_4 in Fumeur Tres Dense (-0.7 mmol/kg) and Fumeur Nouveau (-0.7 mmol/kg) indicate sulfate precipitation as anhydrite in the subsurface as a result of mixing between hydrothermal fluids and seawater in the up-flow zone (Von Damm, 2000) (Reaction 3).

$$Ca^{2+} (+ \text{ minor } Sr^{2+}) + SO_4{}^{2-} \Rightarrow (Ca, Sr)SO_{4\ \text{anhydrite}} \qquad \text{(Reaction 3)}$$

For example, Gallant and Von Damm (2006) observed both significantly negative (-6.72 mmol/kg) and slightly negative (-0.385 mmol/kg) endmember SO_4 concentrations for Marker 2 and Marker 10 hydrothermal vents in Edmond vent field in Central Indian Ridge, respectively. Since Marker 2 had more negative endmember sulfate, it faced with more substantial seawater mixing than Marker 10. Additionally, anhydrite precipitation causes decreasing Ca and Sr concentrations along with vent fluid temperature with respect to the mixing intensity (Reaction 3). Gallant and Von

Damm (2006) calculated ~6 mmol/kg depletion of Ca for Marker 2 compared to other vents in Edmond field, however, slightly less negative Marker 10 endmember sulfate concentrations did not result in substantial Ca depletion. Since Fumeur Tres Dense and Fumeur Nouveau fluids have endmember sulfate concentrations closer to Marker 10 fluids, we might expect not to have major Ca depletions by anhydrite precipitation but still corresponding amount of temperature decrease. Our results are consistent with this analogy although Fumeur Tres Dense and Fumeur Nouveau represent slightly less (~60 ˚C) temperature decrease when compared to Marker 10 (75-90 ˚C) (Gallant and Von Damm (2006). Also, Magali can be considered as a good reference for other Rainbow vents since the calculated endmember sulfate concentration is not negative, indicating no or very minor precipitation of anhydrite as a result of mixing of seawater with hydrothermal fluids in the subsurface. Likewise, Broken Spur vents can be considered as the same due to having zero or positive endmember sulfate concentrations. Lost City fluids, on the other hand, have very high endmember sulfate concentrations (Table 3.3), and this result is consistent with previously reported data. That is, overall endmember SO_4 concentration in Lost City fluids was reported as in between 1 and 4 mmol/kg (Kelley et al., 2005; Lang et al., 2012; Seyfried et al., 2015). As a result, we can confidently say that variability in Mg and SO_4 concentrations in Rainbow, Broken Spur and Lost City hydrothermal fluids is due to seawater entrainment to major samplers during the sampling procedure along with small dead volume contribution and an additional fraction from subseafloor mixing for Fumeur Tres Dense and Fumeur Nouveau vents.

Furthermore, Cl normalized cation values provide a comprehensive comparison chance of cation concentrations between hydrothermal vents since mainly phase separation-controlled Cl is the dominant anion and show positive correlations with cations in hydrothermal fluids (Figure 4.4). Na/Cl and Ca/Cl ratios in Rainbow, Broken Spur and Lost City fluids show both enrichments and depletions relative to background seawater, however, they are well within the range of sampled fluids in other hydrothermal fields present on Earth (Figure 4.4). Changing in endmember Na and Ca concentrations in hydrothermal fluids are net results of different water-rock

reactions. Studies showed that their concentrations are controlled by equilibrium reactions involving plagioclase (e.g. albitization) and pyroxene minerals and some of their alteration products with exchange of seawater Ca and Mg (Berndt et al., 1989; Allen and Seyfried, 2004; Seyfried et al., 2007; Seyfried et al., 2011). In albitization, Ca is released by anorthite destruction but Na is depleted since its incorporated into albite (see Reaction 2). Therefore, identical Na/Cl ratios with ambient seawater in Broken Spur against the idea of substantial albitization (Table 3.4). However, Low Na/Cl values with respect to seawater in Rainbow indicate albitization reaction is mainly responsible for the removal of Na from the hydrothermal fluids. In conjunction with Na loss, absolute very high Ca/Cl ratio observed in Rainbow fluids relative to ambient seawater supports substantial albitization. The comparison of Rainbow and Broken Spur fluids with other vents in global hydrothermal system also indicates that albitization reactions have a primary control on Rainbow fluids whereas it is not the case for Broken Spur (Figure 4.4F). Additionally, although Lost City has similar Na/Cl ratios with Rainbow fluids, albitization is not as significant as the one in Rainbow in Lost City. However, still Lost City fluids have clearly higher amount of Ca when compared to seawater (Table 3.3). This data is consistent with previously reported data (Kelley et al., 2001; Seyfried et al., 2015), and Seyfried et al. (2015) indicated that enrichments of Ca observed in Lost City fluids might be sustained by Ca in clinopyroxene minerals, which are one of the major components of mantle peridotites (Seyfried et al., 2008). Moreover, K is considered as a soluble element in both mafic and ultramafic systems therefore depletions and enrichments of potassium in hydrothermal fluids might be used to understand the general alteration degree of the rock reacting with water during the hydrothermal circulation. K concentration of Rainbow, Broken Spur and Lost City fluids are all well within the concentration range of other hydrothermal systems (Figure 4.4B) however K/Cl ratio of Broken Spur represents comparable amount of enrichments with respect to some other basalt hosted hydrothermal vents (e.g. TAG in MAR and Kairei hydrothermal vents in Central Indian Ridge).

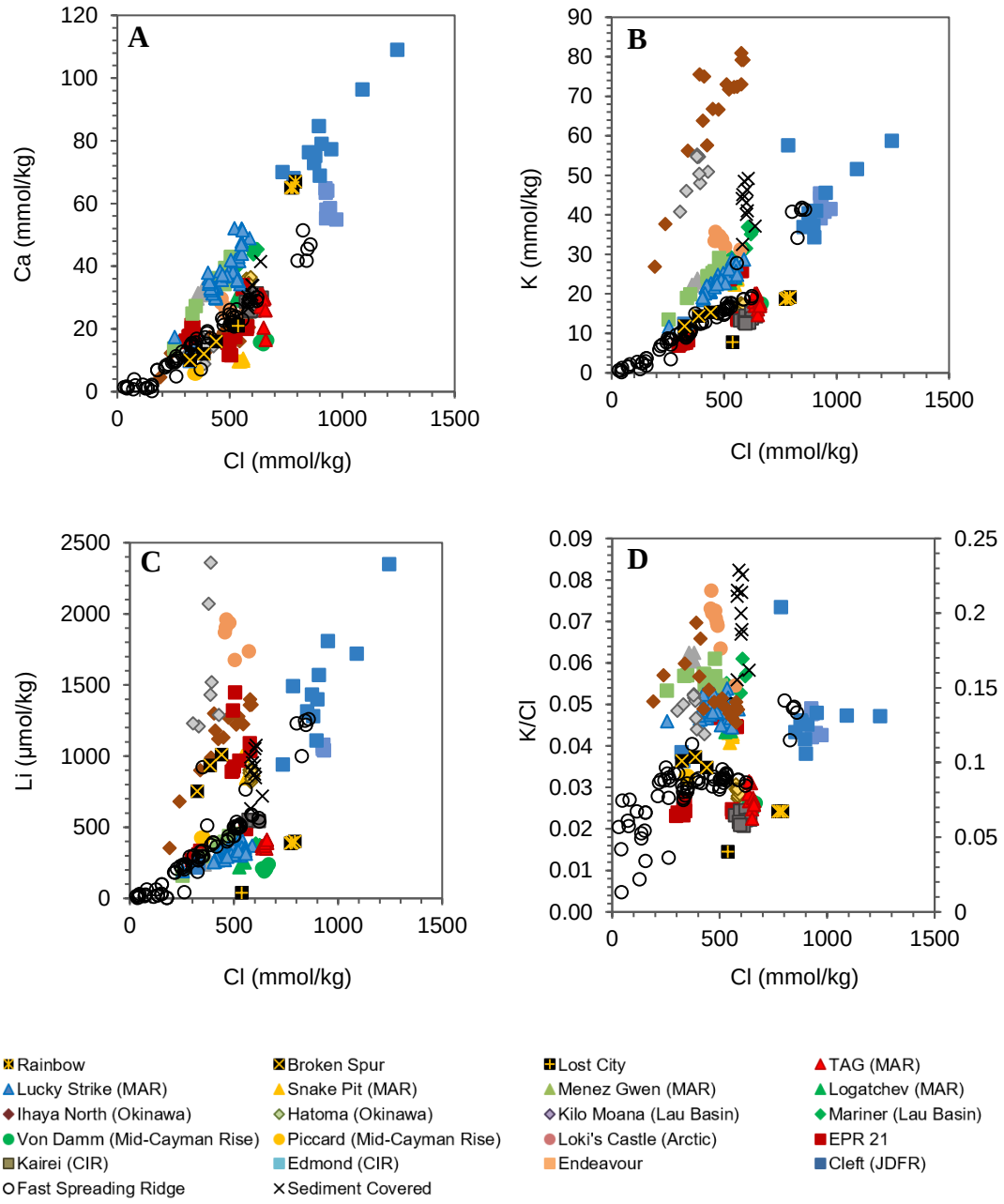

Figure 4.4. Cl versus Ca (A), K (B), Li (C), K/Cl (D), Na/Cl (E), Ca/Cl (G), Fe (I), Mn (K), H_2S (L); Na/Cl versus Ca/Cl (F), K/Na (H); pH versus Temperature (J) for different vent fields around world's oceans. Rainbow, Broken Spur and Lost City hydrothermal fields are indicated in each plot. Rainbow and Logatchev are ultramafic hosted systems in MAR. Vent fluid geochemistry database are used from Diehl and Bach (2020). (Right y-axes are for Okinawa vents when appropriate)

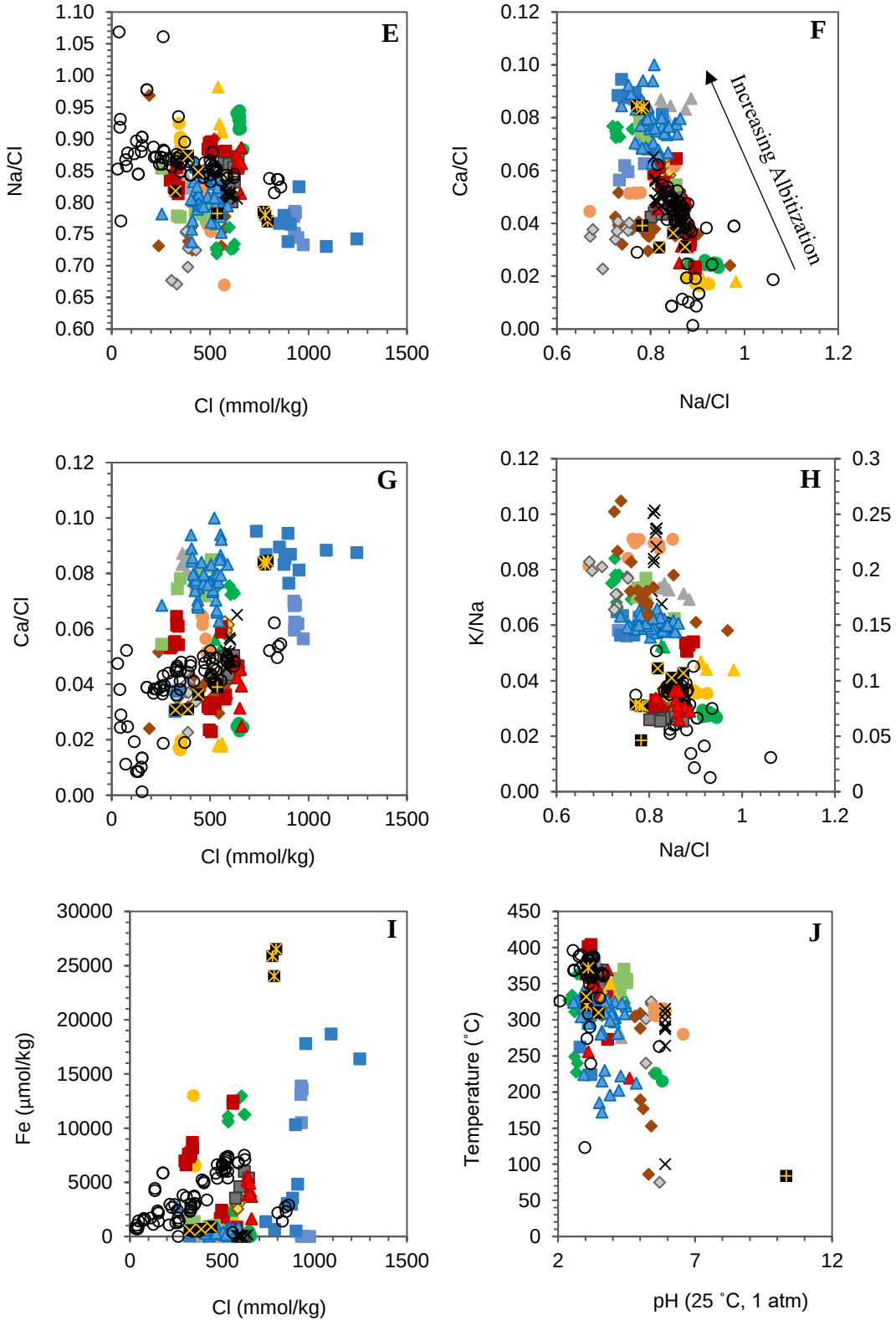

Figure 4.4. (continued)

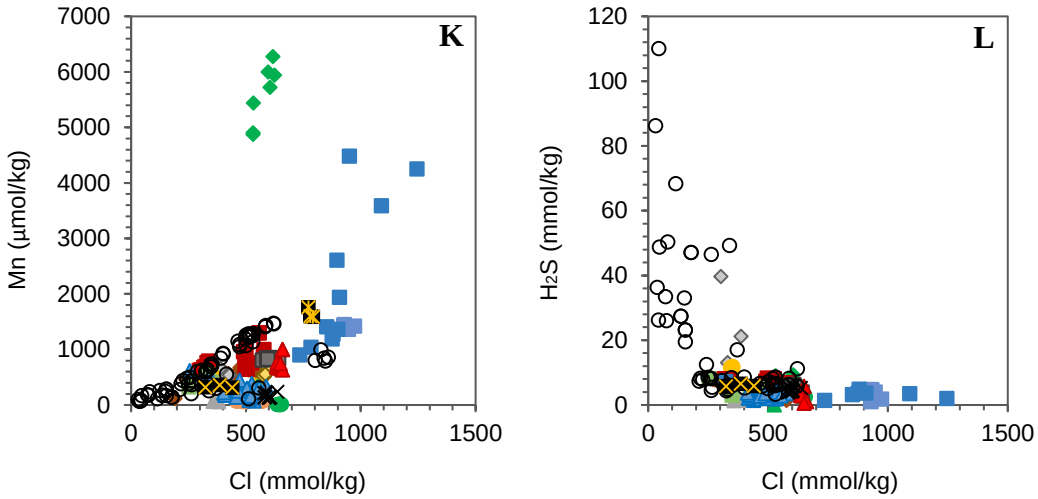

Figure 4.4. (continued)

Based on depletion of K and low K/Na signature, Gallant and Von Damm (2006) stated that reactions of water with altered basalts control the formation and evolution of fluids in Kairei and TAG hydrothermal fields (see Gallant and Von Damm (2006)). Accordingly, since Broken Spur shows enrichments of K and relatively higher K/Na signature (Figure 4.4H), it is expected to have relatively more fresh basalts reacting in Broken Spur hydrothermal field.

The endmember dissolved silica concentration is another important geochemical indicator since it has been used to determine subsurface temperature and pressure conditions of mafic hydrothermal hosted systems (Von Damm, 1991; Bischoff and Rosenbauer, 1985; Foustoukos et al., 2007b). Because temperature and pressure conditions are two main fundamental controlling factors on quartz solubility, it is possible to calculate one parameter by knowing the other one (Figure 4.5) by assuming fluid equilibration with quartz in the reaction zone and no further equilibration in the up-flow zone (e.g. Gallant and Von Damm, 2006; McDermott et al., 2018). Calculated endmember dissolved silica concentrations for Broken Spur vents (7-8.9 mmol/kg) are well below other basalt hosted hydrothermal vents in Mid-Atlantic Ridge (Charlou et al., 2010). Since low endmember Si concentrations are out of quartz stability field under the corresponding T-P conditions (Figure 4.5), fluid-mineral equilibria approach (Von Damm, 1991) on quartz solubility cannot be

applied to Broken Spur fluids directly. However, corresponding endmember Si plots does not exhibit high linear correlation with Mg in Broken Spur. Linear correlation, hence conservative behavior, can be interrupted when a chemical species precipitate in the subseafloor. Therefore, low Si content of Broken Spur fluids might be due to precipitation of some fraction of dissolved Si under the surface as silicate phases. Accordingly, subsurface reaction conditions calculated by Cl concentrations can be used to check this hypothesis because Gallant and Von Damm (2006) stated that conditions obtained from phase separation and quartz solubility should be consisted with each other. By using the methodology provided by (Von Damm, 1991), Broken Spur should have approximately 14 mmol/kg dissolved silica in its fluids in the given P-T conditions (Figure 4.5).

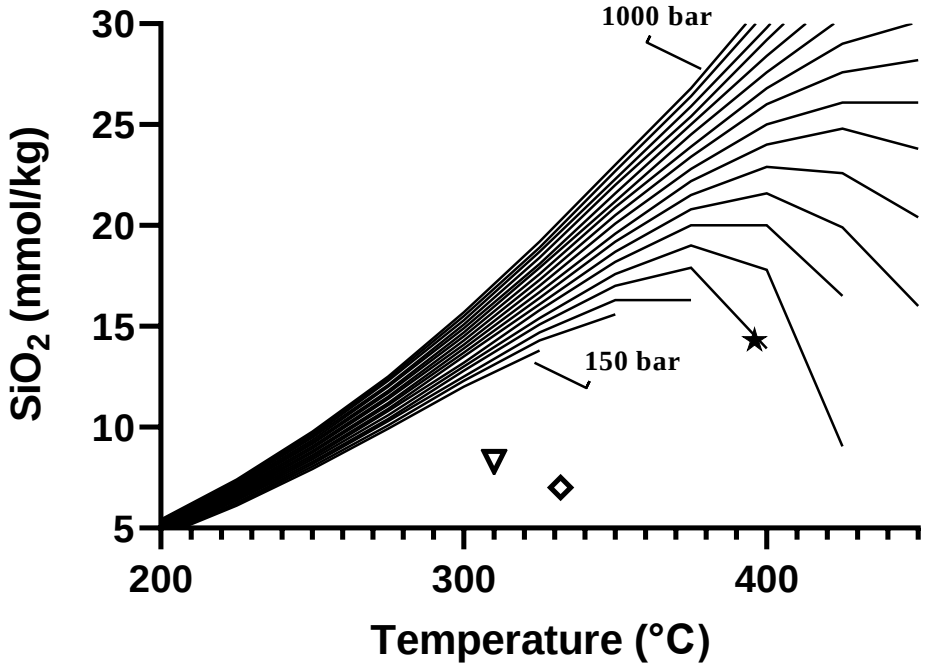

Figure 4.5. Plot of dissolved SiO_2 concentration as a function of temperature and pressure (Von Damm et al., 1991). Pressure values are as noted on the plot and increases incrementally between 150- 1000 bar. Broken Spur vent fluids (inverted triangle: Spire; diamond: Dragon) are indicated on the plot. Star denotes inferred Broken Spur silica concentration based on subsurface phase separation conditions

This states that up to 50% of dissolved silica is precipitated in the subsurface considering calculated endmember Si concentration of Broken Spur (Table 3.4). Silica precipitation in the up-flow zone with cooling (~95 °C in Broken Spur) is not unexpected since solubility of quartz is highly dependent on temperature (Gallant and Von Damm, 2006). This approach, however, is not applied for Rainbow since it is mainly a peridotite dominated and serpentinization controlled system. It is normally expected to have very low dissolved silica concentrations out of quartz saturation level in such a system but Rainbow fluids show an exception since they contain good amount of dissolved Si. This contrasts to the findings of computational models by Allen and Seyfried (2004) and McCollom and Bach (2009) showing peridotite hosted systems generate fluids with very low concentration of dissolved SiO_2 when compared to basalt hosted systems. Therefore, in Rainbow, another source for extra dissolve Si component should be present. Seyfried et al. (2011) suggested that interaction of gabbroic bodies in addition to peridotites is likely in Rainbow hydrothermal fluids. Additionally, same situation is present for peridotite hosted Logatchev vent field in MAR since Logatchev fluids exhibits similar elevated dissolved silica concentrations (see Charlou et al., 2010). Also, gabbroic outcrops present around the hydrothermal vent fields supports the idea of gabbroic interaction in Rainbow hydrothermal field (Douville et al., 2002; Schmidt et al., 2007). Therefore, emplacement of gabbroic intrusions is inferred as the main driving factor of silica enrichments in hydrothermal fluids in peridotite hosted systems. Additionally, McDermott et al. (2015) stated a similar case for Von Damm vent field in Mid- Cayman Rise. Although Rainbow contains more metal rich, acidic and higher temperature fluids with respect to Von Damm vent field, they both share similar dissolved silica concentrations.

4.1.3 Lithium Concentration and Water/Rock Ratios

Broken Spur fluids contain higher amount of Li concentration when compared to most of the basalt hosted hydrothermal systems in different settings while Rainbow

has comparable amount of Li with respect to other peridotite hosted systems e.g. (Logatchev) (Figure 4.4C). However, Lost City is an exception. Although its fluids show enrichments with respect to ambient seawater, Lost City has one of the lowest ever measured Li concentration among other vents (Figure 4.4C). Different studies demonstrated that Li has been used to calculate water/rock mass (w/r) ratios in hydrothermal systems due to its highly mobile character during water/rock reactions (Von Damm et al., 1985; James et al., 1995; Seyfried et al., 1998; Foustoukos and Seyfried, 2005; Gallant and Von Damm, 2006; Pester et al., 2012; Seyfried et al., 2015). Von Damm et al. (1985) stated that it is possible to calculate w/r ratios after knowing the concentration of alkali elements present in the rock, and assuming both quantitative leaching of alkali elements from rocks and no precipitation by partitioning of corresponding element into any secondary minerals. Different rock types contain different proportion of alkali elements. For example, Tomascak et al. (2008) calculated Li concentration of different basalts dredged from 23-39 ˚N in MAR in between 3.82 ppm and 7.11 ppm (average 5.37 ppm) and Wilson et al. (2013) calculated very similar concentration as 5.11 ppm in average (n=109) for axial basalts from 13-14 ˚N in Mid-Atlantic Ridge. Considering the endmember Li concentration of Broken Spur, w/r is calculated in between 0.73- 0.98. However, this calculation has been done by assuming total leaching of Li from rocks but different studies showed that Li is leached up to ~70% from rocks during high temperature water/rock reactions (Mottl and Holland, 1978; Seyfried et al., 1984; Von Damm et al., 1985; Seyfried et al., 1998). Therefore, w/r of Broken Spur becomes 0.5-0.7 after applying 70% extracting efficiency. This w/r ratio is same with what James et al. (1995) calculated for Broken Spur. Moreover, Früh-Green et al. (2018) reported different peridotite lithologies with different Li concentrations from IODP Expedition 357 in Atlantis Massif. They recovered cores containing harzburgites and dunites from drill holes in Atlantis Massif. In order to have the best representation, however, some of the drill cores directly on top of the Lost City field have been chosen in this study. Li concentrations of these lithologies are changing between 0.22 ppm and 8.73 ppm (mean: 2.57 ppm) (Früh-Green et al., 2018). Relatively wide

range seen in Li concentration in Lost City peridotites might be due to the degree of serpentinization. Decitre et al. (2002) showed that Li concentration is sensitive to alteration state of peridotites; a general increasing concentration trend with increasing degree of serpentinization. For example, Li concentrations were reported in between 0.6 ppm and 8.2 ppm for samples with serpentinization degrees 67-94% from southwest Indian Ridge (SWIR) (Decitre et al., 2002). W/R ratio for Lost City was tried to be calculated in the same manner however, within this wide concentration range (i.e. 0.22-8.73 ppm) it does not provide a comprehensive information since calculation gives w/r in between 0.81 and 32.2. Therefore, in order to get a general understanding about the system, mean Li concentration was preferred to be used in w/r calculation. As a result, it was calculated as ~9.5, which is a very similar value suggested by Allen and Seyfried (2004). They created a computational model in order to understand the fluid evolution in Lost City hydrothermal field and concluded as w/r in Lost City should be ≥ 10. However, a more recent study by Seyfried et al. (2015) calculated w/r of 5 for Lost City system. This value can be reached by eliminating the outlier from the dataset reported by Früh-Green et al. (2018). Since Li concentrations of peridotites on top of Lost City field do not exhibit uniform or normal distribution, 8.73 ppm turns out to be an outlier in the given dataset. If a new average is calculated as 1.34 ppm by excluding the outlier, w/r ratio for Lost City becomes 4.96, which is very close to what Seyfried et al. (2015) was reported. Additionally, Li content for mantle is reported in different studies as approximately 1.6 ppm (McDonough and Sun, 1995; Ottolini et al., 2004). By considering mantle Li concentration, w/r ratio for Lost City might also be calculated very close to all these values as well. Also, Foustoukos et al. (2008) calculated w/r ratio of Lost City in between 2 and 4 by using Sr concentration and its isotopes. This is smaller than what is calculated by using Li concentrations however applying 70% extraction efficiency put w/r (i.e. 3.5) into this interval as also stated in Seyfried et al. (2015). Further, Rainbow has an average Li concentration of 6.7 ppm in serpentinites dredged on top of Rainbow vent field according to results by Andreani et al. (2014). Additionally, by considering Li concentration in mantle (McDonough

and Sun, 1995; Ottolini et al., 2004) and %70 of extraction efficiency, w/r ratio for Rainbow might be calculated in a range between 0.42 and 1.74. However, calculation of w/r in Rainbow by considering only peridotites may not reflect absolute values since interaction with gabbroic bodies in addition to peridotites are indicated by other geochemical tracers as well (e.g. endmember Si concentrations). Therefore, it is hard to make a direct calculation for Rainbow w/r ratio.

Water/rock ratios are important to understand general feature of reaction dynamics in the subsurface. For example, low w/r ratios state that reaction happens between high volume of rock and relatively low volume of water. This means that reacting rock has not been subjected to intense alteration before the hydrothermal activity (Von Damm et al., 1985). On the other hand, it might be concluded that a small amount of rock reacts with relatively large volumes of water in large w/r ratios, which means the reacting rock has already been subjected to intense alteration and some mobile elements like Li have already been leached (Von Damm et al., 1985). Therefore, low w/r ratio calculated for Broken Spur hydrothermal vent field might indicate that water/rock reactions during the hydrothermal circulation in Broken Spur happen in between relatively fresh basalts and water. This finding is consistent with the inference based on K/Na ratio. However, it is not the case for Lost City since its w/r is very high. Also, it is hard to make an ultimate conclusion for Rainbow system by using w/r ratio but still considering only peridotites for the simplicity gives relatively low w/r ratios when compared to Lost City. Additionally, Rainbow fluids contain relatively larger amount of Li concentrations when compared to Logatchev hydrothermal vent field, which is in same character with Rainbow according to classification by Kelley and Shank (2010). Augustin et al. (2012) indicated that water/rock reactions in Logatchev occur under variable w/r ratios therefore a relatively large interval seen in Rainbow even considering only peridotites might imply that a similar case seen in Logatchev might be applicable for Rainbow as well.

4.1.4 Effects of Fluid/Rock Reactions on Metal Mobility and H_2S Composition

Except Fe and Mn, endmember concentration of transition metals could not be calculated for Rainbow and Broken Spur fluids. Sample recovery generally takes variables hours in vent fluid studies, therefore initial temperature of samples cools down to background ocean temperature (see Findlay et al., 2015). Most of the transition metals are sensitive to sharp temperature decreases during sample recovery therefore they might precipitate inside the samplers (e.g. Seewald et al., 2015; McDermott et al., 2018; Seewald et al., 2019). For example, Trefry et al. (1994) showed that in their collected hydrothermal samples, variable amounts of Zn, Cd, Pb (up to 20%), Cu (up to 50%) and Co (up to 5%) precipitated in the major samplers. Therefore, it is hard to obtain true dissolved fraction of such metals present in hydrothermal fluids. However, Fe and Mn do not follow this trend and none or insignificant proportions of these species are precipitated in the major samplers. For example, Yucel et al. (2011) calculated that less than 2% of FeS_2 fraction comes from cooling-induced precipitation in the major samplers. Additionally, pressure release during the sample recovery might result in dissolution of precipitated metal sulfides however effect of pressure might not balance the loss from cooling since temperature has much more substantial effects on solubility of these phases when compared to effects of pressure (Reed and Palandri, 2006).

Calculated endmember Fe and Mn concentrations showed that Rainbow has one of the highest Fe and Mn containing fluids among other hydrothermal systems while Broken Spur Fe and Mn concentrations are well within the range seen in other basalt hosted systems (Figure 4.4K-I). However, Lost City fluids are metal-free in character under the control of low temperature serpentinization reactions since all concentrations regarding transition metals in Lost City fluids are below limit of detection as also reported in previous studies (Allen and Seyfried, 2004; Charlou et al., 2010). Different geochemical parameters affect overall metal concentrations in hydrothermal vent fluids including pH, temperature, as well as dissolved sulfide and

chloride concentrations (Janecky and Seyfried, 1984; Von Damm et al., 1985; Seyfried and Ding, 1993, 1995). For example, Seyfried and Ding (1993) showed that it is possible to have substantial increases in Fe (159%) concentration by lowering pH only from 5 to 4.8. This is consistent with our dataset and Figure 4.6 indicates that there is an increasing trend in dissolved iron concentration with decreasing pH in both Rainbow and Broken Spur vent fluids. Additionally, the minimum pH (e.g. 3.04-3.10) in samples containing low Mg concentrations in Rainbow fluids are consistent with the pH range reported by Seyfried et al. (2011). Accordingly, low pH character of Rainbow fluids might have some contributions in generating very high concentration of Fe in Rainbow fluids (Douville et al., 2002). Janecky and Seyfried (1986) showed that low pH conditions can be sustained as a result of serpentinization reactions. H^+ is produced during Mg precipitation as serpentine group minerals as a result of hydration of olivine and pyroxene in peridotites. Fe content might increase since extra H^+ could trigger further magnetite (Fe_3O_4) dissolution, which is one of the main products of serpentinization (Janecky and Seyfried, 1986).

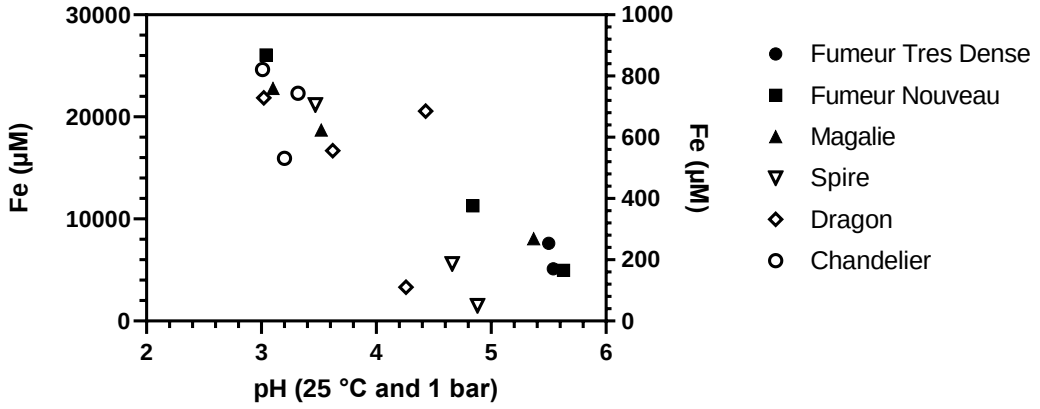

Figure 4.6. Negative correlation between pH and endmember Fe concentrations for both Rainbow (left y-axis) and Broken Spur (right y-axis) hydrothermal fluids. R-squared and p-value for Rainbow are calculated as 0.98 and <0.0001, respectively while R-squared is 0.64 and p-value is 0.0055 for Broken Spur fluids

Additionally, high Cl concentrations leads to increase metal content in the solutions since most of the metals are transported as chloro-complexes in the fluids (e.g. $FeCl_2$, $ZnCl_2$, $CoCl_4^{2-}$ etc) (Ding and Seyfried, 1992; Seyfried and Ding, 1993; Von Damm, 1990; Trefry et al., 1994; German and Von Damm, 2003). Our data demonstrates that very large endmember Cl concentrations calculated for Rainbow fluids result in formation of very high dissolved Fe and Mn concentrations in hydrothermal vent fluids (Table 3.3). As an example, a similar case was reported by Von Damm and Bischoff (1987) for Southern Juan de Fuca Ridge vents, which contain very high Cl concentrations up to 1090 mmol/kg with one of the highest Fe (18.7 mmol/kg) observed in hydrothermal vent fluids. On the other hand, since Cl tends to partition into brine phase after the phase separation, vapor phases is depleted in the case of Cl content. Therefore, subcritical phase separation-controlled vapor-rich fluids lead Broken Spur to have much lower endmember Fe concentrations (571-894 μmol/kg) in its fluids. Also, cross comparison in individual Broken Spur vents, Spire, Dragon and Chandelier, exhibit a consistent trend supporting increasing Cl content with increasing dissolved Fe concentrations (see Table 3.3 and Table 3.5). Another factor controlling Fe depletion in Broken Spur might be related with dissolved H_2S concentration in the fluids. Broken Spur fluids contain high amount of endmember hydrogen sulfide (5.72- 6.56 mM) while measurements showed that it was all below the limit of detection for Rainbow and Lost City hydrothermal fluids. Previous studies reported endmember H_2S concentrations as around 8.5- 11 mM for Broken Spur (see Charlou et al., 2010), 1.2 mM and 2.9 mM for Rainbow (Douville et al., 2002; Seyfried et al., 2011), and 0.25–2.9 mmol/kg for Lost City (Lang et al., 2012). The endmember H_2S concentrations for Broken Spur should be considered as minimum values, but still it has relatively comparable amount of H_2S with respect to other hydrothermal vent fields (Figure 4.4L). Therefore, considering both previously reported data for Rainbow and endmember calculations for Broken Spur fluids, these two fields can be classified as high Fe:H_2S and low Fe:H_2S settings, respectively. Low sulfide bearing fluids of Rainbow might be due to its brine rich character since H_2S mostly partitions into vapor phase after the phase separation. Since most of the

metals (e.g., Fe, Cu, Zn, Cd) likely to form minerals with sulfide species, high concentration of H_2S in Broken Spur prone to deplete some of the Fe content as a result of precipitation in the subseafloor. In that regard, pH of fluids provides indirect evidence to understand the dynamics of iron sulfide precipitation in the subsurface. German and Seyfried (2014) indicated that if hydrothermal fluid pH is lower than 3.3±0.5, it might indicate metal sulfide precipitation occurring in the subsurface. Considering the minimum measured pH values is in 3.01-3.47 range, it is expected to lower Fe and H_2S concentration with metal-sulfide precipitation (e.g. FeS_2, $CuFeS_2$ etc.) in Broken Spur fluids. Additionally, relatively low degree of correlation seen in Fe endmember plots in Broken Spur fluids when compared to Rainbow is consistent with subseafloor precipitation since precipitation disrupts conservative nature of elements, hence degree of correlation with Mg in endmember plots (Figure 3.2). Therefore, it can be concluded that interplay of high sulfide and low Cl content of Broken Spur fluids are consistent with relatively low dissolved Fe concentrations observed in the field. Furthermore, temperature is another key geochemical component that control solubility of phases in the subsurface. Seewald and Seyfried (1990) showed that Cu is very sensitive to temperature changes, followed by Fe, Zn and Mn regarding their temperature dependent reaction kinetics. For example, previous works demonstrate that $CuFeS_2$ (chalcopyrite) is one of the most common Cu minerals seen in hydrothermal vent environments and it precipitates easily at temperatures lower than 300-350 ˚C while solubility of ZnS (sphalerite) is less sensitive to temperature decrease and it might not precipitate until temperature reaches 200-250 ˚C (Janecky and Seyfried, 1984; Seyfried and Ding, 1995; Seyfried et al., 2011). Therefore, hydrothermal fluids lose their Cu and Fe content as temperature decreases in the up-flow zone prior to Zn and Mn. In that case, Fe/Mn ratios of the fluids from Rainbow and Broken Spur demonstrate that the ratio increases with increasing vent fluid temperature (Table 3.4). This relationship supports the idea that temperature controls the solubility of Fe and Mn and as the temperature decreases, hydrothermal fluids loss their Fe content much easily than Mn due to precipitation of Fe in the subsurface. As different studies, including this

one, showed that cooling of hydrothermal fluids after releasing from very high temperature reaction zone is a common phenomenon, therefore, substantial amount of transition metals is expected to precipitate under Broken Spur and Rainbow hydrothermal fields as hydrothermal vent deposits (e.g. Metz and Trefry, 2000; Gallant and Von Damm, 2006, Tivey, 2007).

Furthermore, Fe/Mn ratio is used as a geothermometer in vent fluid studies to estimate subsurface reaction temperature that controls Fe and Mn solubility (e.g. Pester et al., 2012; McDermott et al., 2018). This method developed experimentally by Pester et al. (2011) for basalt hosted hydrothermal systems up to 450 ˚C. Since inferred subsurface temperatures for Broken Spur (400-405 ˚C) and Rainbow (420 ˚C) by using Cl concentrations are within the calibration range of Fe/Mn geothermometer, subsurface reaction conditions might also be checked accordingly by using the Equation 1:

$$T\ (^{\circ}C) = 331.24+112.41*\log\ [Fe/Mn] \qquad \text{(Equation 1)}$$

Fe/Mn ratio for Broken Spur (1.78-2.86) gives a temperature range as 359-382 ˚C. Although this range is higher than the measured temperature in the orifice, it is well below the inferred temperature by phase separation. This is consistent with the idea supporting subseafloor precipitation of these metals due to cooling, and therefore depletion of Fe in the fluids. On the other hand, by using Fe/Mn ratio for Rainbow (12.71-12.87), subseafloor temperature condition is calculated as ~455 ˚C. This is a higher value when compared to temperature indicated by phase relation calculation with Cl concentration. There might be different reasons for this discrepancy; (1) the inferred temperature by geothermometer is slightly beyond the calibration range of the method although prediction range of Equation 1 is ±10 ˚C, and (2) this method is developed for basalt hosted systems however reactions in Rainbow are sustained with peridotite and gabbro as the other geochemical indicator stated as well.

4.2 Spatial and Temporal Variations of Broken Spur, Rainbow and Lost City Fluids

Different studies indicated that Mid-Atlantic Ridge hydrothermal vents exhibit both spatial and temporal stability over short to medium timescales (Charlou et al., 2010; Kelley and Shank et al., 2010; Koschinsky et al., 2020). Based on the sampling efforts in vent fields at MAR, there are vent fluid geochemistry records over time for different vent fluids. For example, samples were taken between 1993 and 2013 for Logatchev-1, 1997 and 2010 for Menez Gwen, 1986 and 1998 for TAG, 1996 and 2016 for Lucky Strike, 1997 and 2008 for Rainbow and 2000 and 2008 for Lost City vent fields (see Koschinsky et al., 2020). On the other hand, there are scarcities in data for some vent fields as well such as Broken Spur since it was sampled only once in 1993 (James et al., 1995). In this study with the new dataset, we are now able to to understand 25 years of variation in Broken Spur. Also, sampling periods for Rainbow and Lost City were widened to 21 years and 18 years, respectively (Kelley et al., 2001; Douville et al., 2002; Seyfried et al., 2011; Seyfried et al., 2015; this study).

For Rainbow, Figure 4.7B indicates that all datasets from 1997, 2008 and 2018 are consistent with each other therefore Rainbow fluids show high temporal stability through 21 years of time span. A similar case is present also for Lost City fluids. All non-volatile dissolved species reported in between 2000 and 2018 indicate that Lost City fluids do not represents dramatic changes over time (Figure 4.7C). There seem some variations in SO_4 and Li concentrations in different years however they are more likely spatial variations rather than representing a temporal change (see Charlou et al., 2010 and Seyfried et al., 2015). The medium-term stability seen in both Rainbow and Lost City fields indicates no major change in physico-chemical conditions and heat supply have occurred in the reaction zone hence continuous serpentinization has been taking place over time for both fields. On the other hand, there are significant compositional transition in Broken Spur in 25 years between 1993 and 2018 as shown in the Figure 4.7A. That is, a net decrease in concentrations

of most of the non-volatile dissolved species including Cl, Br, Li, Na, K, Fe and H_2S is present in Broken Spur fluids over time. Both 1993 and 2018 datasets represent emitting vapor phase fluids therefore both of their Cl concentration are well below seawater Cl value (e.g. 546 mmol/kg). Considering logarithmical relationship between chlorinity and pressure/temperature conditions in phase separation (Figure 4.2), it is expected to obtain this Cl variation without having a dramatic change in subsurface reaction conditions. For example, average Cl concentration of Broken Spur vents is 382 mmol/kg in 2018 and it represent 2.25 % wt NaCl. However, Cl concentration was reported as 469 mmol/kg in 1993 and the chlorinity is calculated as 2.75 % wt NaCl. In that regard, by using the two-phase relation (Bischoff and Pitzer, 1989), 2018 and 1993 datasets represent very similar subsurface conditions as 400 ˚C, 285 bars and 405 ˚C, 290 bars, respectively. Also, it is possible to explain net decrease in concentration of other ions by considering their strong relationship with Cl concentration (Figure 4.7A). On the other hand, it is hard to explain the sharp decrease in dissolved Fe concentration in 25 years (Figure 4.7A). It is unexpected to have such a sharp concentration decrease without changing physico-chemical conditions in the reaction zone but the Cl data represents no such major change as indicated. However, our dataset for Broken Spur represents an extensive Si precipitation in the subsurface considering the lowest calculated endmember Si concentration of Broken Spur among other basalt hosted systems in MAR (Charlou et al., 2010). Therefore, we are proposing that some fraction of Fe might be incorporated in silicate minerals with conductive cooling in the up-flow zone over time. Additionally, medium to low linear correlation seen in Fe and Si endmember plots supports that Fe might be precipitating in the subsurface together with Si. Solubility of iron and quartz are highly dependent on temperature hence if ~100 ˚C conductive cooling in Broken Spur is considered, it is expected to have deposition of Si in the subsurface during fluid rise to seafloor by conductive cooling (Gallant and Von Damm, 2006). Additionally, no dissolved Si data was reported by James et al. (1993) hence further comparison cannot be conducted regarding Si composition in each year.

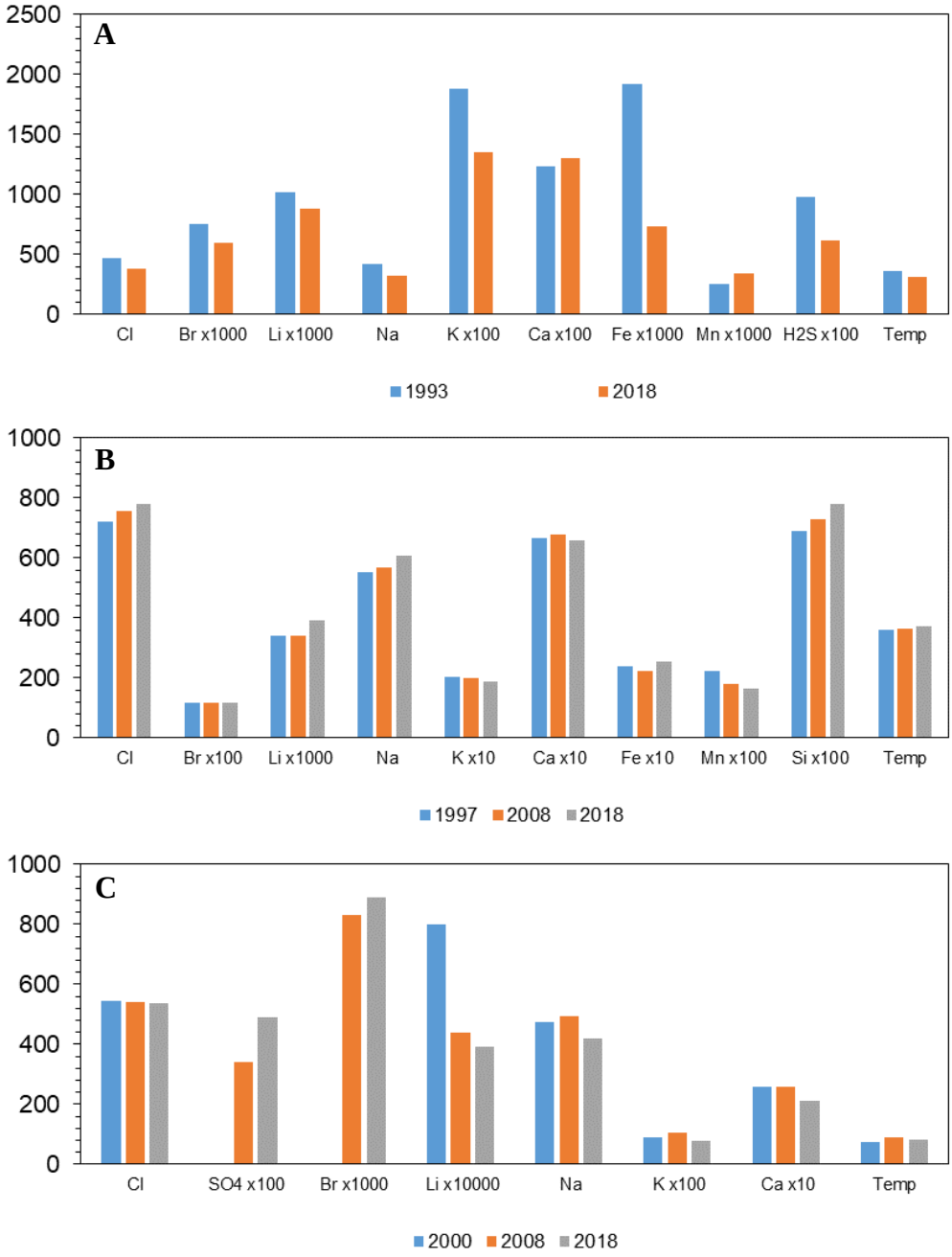

Figure 4.7. Temporal variations of Broken Spur (A), Rainbow (B) and Lost City (C) hydrothermal fields. Y-axes representing concentrations in mmol/kg and temperature in °C. Values have been multiplied as noted on the plot to have a plotting with a single y-axis. (Broken Spur: James et al. (1995); Rainbow: Douville et al. (2002); Seyfried et al. (2011); Lost City: Kelley et al. (2001); Seyfried et al. (2015))

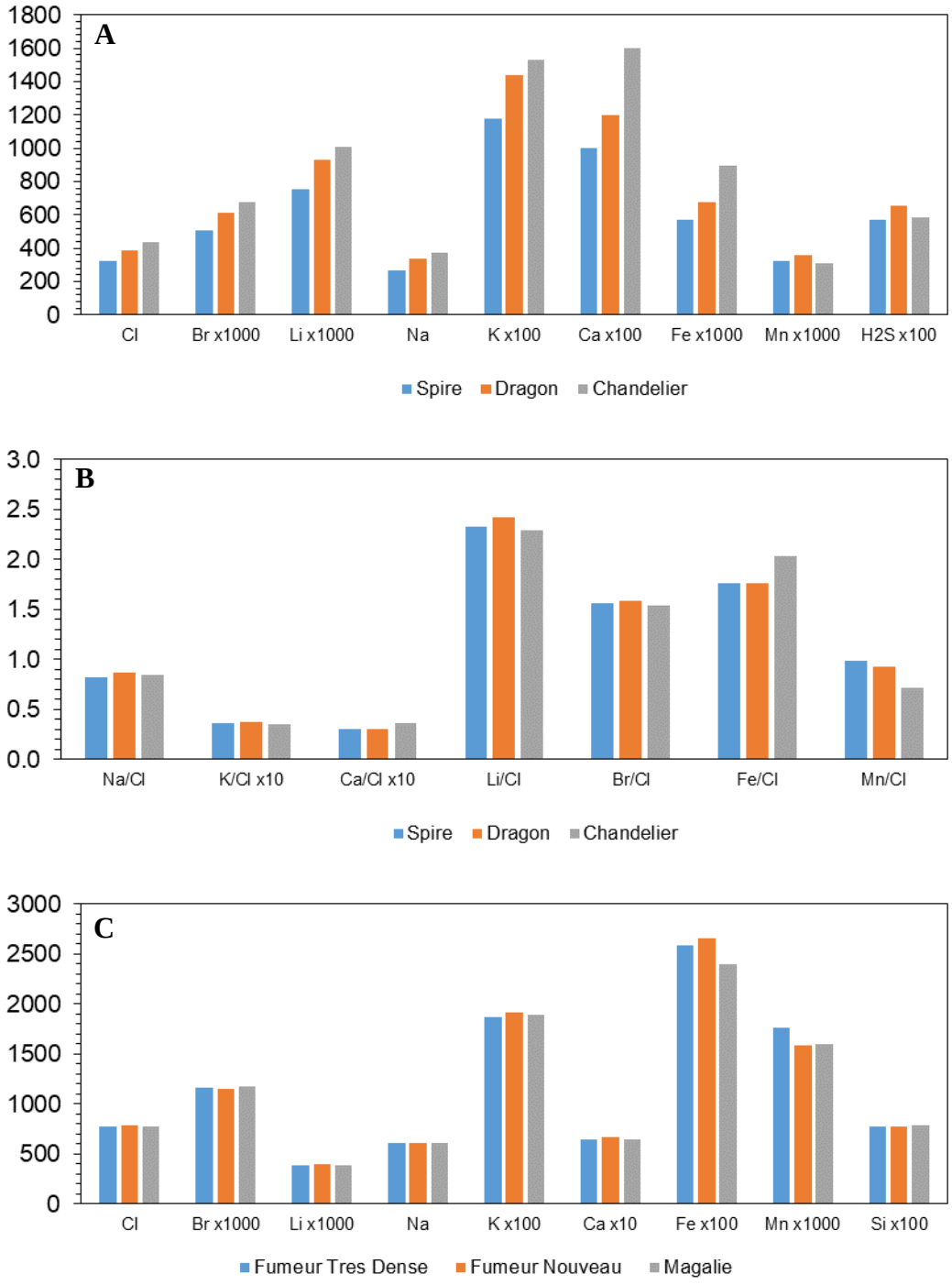

Figure 4.8. Spatial variations of different geochemical species in Broken Spur (A, B) and Rainbow (C, D) hydrothermal vent fields. Y-axes representing concentrations in mmol/kg. Values have been multiplied as noted on the plot to have a plotting with a single y-axis

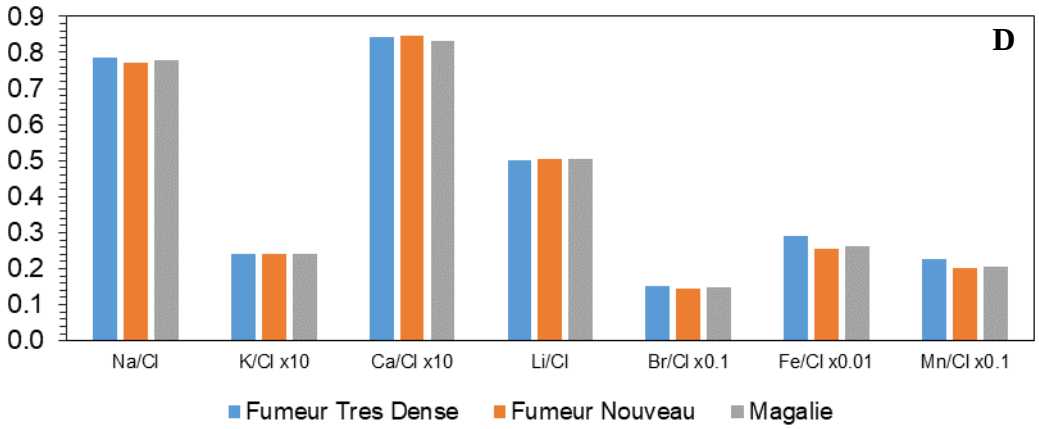

Figure 4.8. (continued)

However, vent fluid temperature data also shows that there is a decrease in exit temperature of fluids from the orifice (as much as 50 ˚C) in between 1993 and 2018 (Figure 4.7A), which is supporting the idea of extensive cooling through time and likely subsurface Si precipitation with Fe with cooling. Moreover, chalcophile character allows Fe to precipitate with sulfur in the subsurface and there is a net decrease in H_2S concentration over time as indicated in Figure 4.7A. However, as discussed earlier, it is hard to estimate the exact fraction joining Fe-S precipitation since measuring less H_2S might be a sampling artifact by considering the non-gas tight character of major samplers. However, still low pH of fluids in Broken Spur states that there occurs Fe-sulfide precipitation in the subsurface hence it is expected that some fraction of dissolved iron might be lowered with existing dissolved H_2S concentration considering decreasing sulfide trend over time. The further comparison cannot be conducted to understand the sulfide precipitation dynamics in comparison with 1993 since no pH data was reported previously (James et al., 1993). Also, there are some records in vent fluid geochemistry literature for describing sharp fluctuations in Fe, Cl and H_2S concentrations over time in East Pacific Rise (EPR) (e.g. Von Damm, 2000; Yucel and Luther, 2013, Yucel et al. in prep.). Geologically, EPR is a very active system therefore magmatic eruption cycle of EPR is very short unlike MAR. In other words, the first documented eruption happened in EPR 9º50’ N in 1991/ 1992 (Haymon et al., 1993; Rubin et al., 1994) and just

within ~15 years in late 2005 second eruption was detected (Tolstoy et al., 2006). Researchers including Von Damm (2000, 2004), Yucel and Luther (2013) stated that eruption events directly affect the chemical composition of the vent fluids and result in high concentration of H_2S and low concentration of Cl and Fe just after the eruption but increasing dissolved Fe with Cl and decreasing H_2S in time. Therefore, considering the location of Broken Spur on the spreading axis, a similar framework might be drawn to explain variations in Fe, Cl and H_2S concentration in Broken Spur fluids over time since the geochemical state of these species looks to represent an eruption stage. However, there are no signs (e.g. fresh pillow basalt outcrops etc.) regarding a recent eruption happened in Broken Spur field, therefore, this possibility cannot be accounted.

Furthermore, examining spatial variations of vent fields are important in order to estimate general flow path in the subsurface and state of the fluid source. Individual vents of Rainbow, Fumeur Tres Dense, Fumeur Nouveau and Magali, shows very similar geochemical compositions with each other (Figure 4.8C). The consistency between spatially distributed vent fluids is an important signature for the idea covering Rainbow fluids are fed by a single deep source as stated also in previous studies (Charlou et al., 2002; Seyfried et al., 2011). Also, Cl normalized values are almost same for all non-volatile dissolved species (Figure 4.8D), which also supports the single deep source idea for Rainbow (Gallant and Von Damm, 2006). However, it seems there are some variations for non-volatile dissolved species among individual Broken Spur vents, Spire, Dragon and Chandelier (Figure 4.8A). As stated in the previous sections, Cl is the dominant ion in hydrothermal vent fluids and behavior of other ions are highly tight to Cl. It is consistent with the trend in Figure 4.8A that increasing Cl with increasing concentration of other non-volatile dissolved species among individual vents. Therefore, solely examining differences in absolute endmember concentrations might not give correct explanation for state of deep fluid source for Broken Spur case. Accordingly, Cl normalize values exhibit very similar values among each vent (Figure 4.8B) in Broken Spur fluids, hence we suggest that Broken Spur fluids are fed by single deep source in the subsurface as well.

Additionally, a recent study by Chavagnac et al. (2018) can be used as a supporting remark on explaining differences in dissolved concentrations of chemical species among individual vents in the same field to show how such a situation does not rule out the possibility of sharing same source in the subsurface. Chavagnac et al. (2018) showed that Capelinhos vent fluids in Lucky Strike hydrothermal field has very different geochemical characteristics (e.g. Cl: 262.3 mM) when compared to other vents in Lucky Strike (e.g. Cl: 415-574 mM), however still they share a common fluid source in the subsurface.

4.3 Factors Controlling the Near-Field Export of Vent Products in the Rainbow and Broken Spur Rising Plumes

It is also important to understand how endmember fluid compositions evolve as hydrothermal fluids rise in the deep-water column and mix with ambient seawater after emitting from the vent orifice since some of the chemicals (e.g. Fe, Mn etc.) released from hydrothermal vents might have substantial implications on global ocean biogeochemistry (Resing et al., 2015; Fitzsimmons et al., 2017; Ardyna et al., 2019). Additionally, since the redox gradient is intense between highly reducing hydrothermal vent plume and oxidizing bottom seawater, examining plume geochemistry may provide opportunities to further study on some special geochemical reactions in hydrothermal plumes as well. For example, recent advancements show that naturally occurring nanoparticles are an important part of vent fluid geochemistry, and they might be responsible for near-field transport of previously unexpected fraction of hydrothermal chemicals in the deep ocean (Yucel et al., 2011; Findlay et al., 2015; Findlay et al., 2019). To this end, Rainbow and Broken Spur vent fields provide insights into not only on understanding how much dissolved chemical species are sustained in different vent settings but also how different geochemistry may affect compositional evolution of vent (nano)particles from the subseafloor throughout the rising plume.

It was already showed in the previous sections that Broken Spur has fluids rich in $\sum H_2S$ and comparable amount of Fe, which creates low Fe:H_2S dynamics. On the other hand, Rainbow controlling by high temperature serpentinization reactions produces fluids with much higher Fe:H_2S ratios.

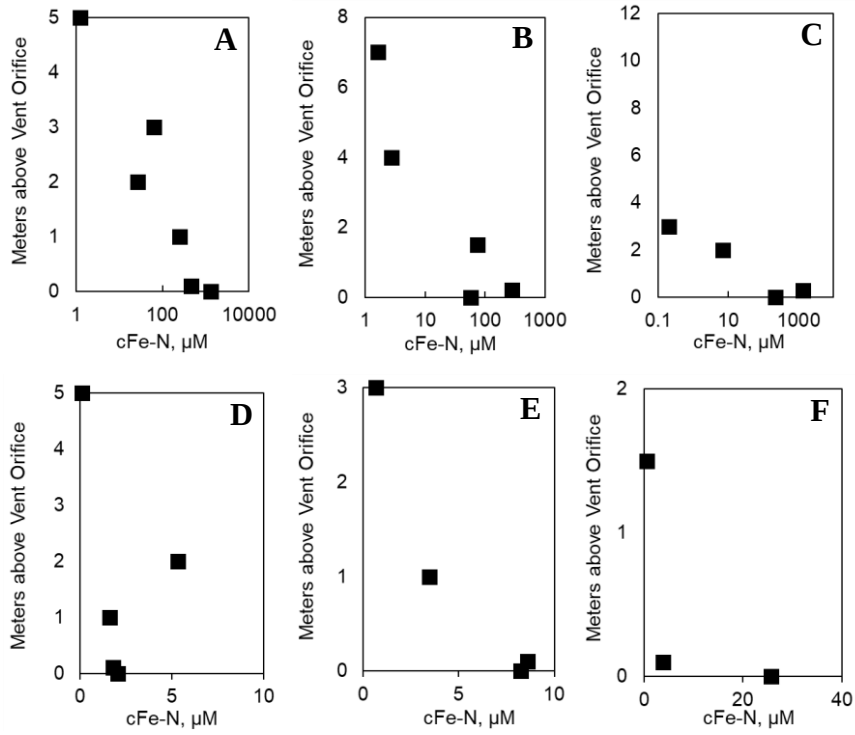

Figure 4.9. Nanoparticle iron (cFe-N) profiles for Magali (A), Fumeur Nouveau (B) and Fumeur Tres Dense (C) plumes in Rainbow and Spire (D), Chandelier (E) and Dragon (F) plumes in Broken Spur (regenerated from Yucel et al. (2021))

It is also important to notice that relatively high concentration of other transition metals such as Cu and Zn (e.g. Cu & Zn: ~260 µM) observed in Rainbow fluids (Seyfried et al., 2011) might have important implications on sulfide dynamics in Rainbow since they tend to precipitate with sulfide species with decreasing temperature and remove comparable amount of sulfide from the Rainbow fluids (Findlay et al., 2015). Therefore, interplay of these species determines the ultimate fate of (nano)particles in Rainbow and Broken Spur fluids. Yucel et al. (2021) conducted up-to-date nanoparticle iron (cFe-N) measurements and presented iron

size fractionation data for Rainbow and Broken Spur vent fields (Figure 4.9). It is obvious that the distinct geochemical systematics observed in both vent fields have substantial implications on quantitative production of cFe-N. For example, Yucel et al. (2021) indicated that one of the main reasons behind much higher concentration of cFe-N just next to the orifice and throughout the rising plume in Rainbow vents when compared to Broken Spur might be that Rainbow fluids have much higher endmember Fe concentration (24- 26.5 mM) relative to Broken Spur (570- 900 μM). Additionally, this quantitative shift also results in sustaining much more cFe-N in the upper parts of the buoyant plume in Rainbow fluids relative to Broken Spur rising plumes (Yucel et al., 2021). For example, they were measured 1.23 μM, 1.64 μM and 0.2 μM of cFe-N at coolest hydrothermal fluid samples from the Magali, Fumeur Nouveau and, Fumeur Tres Dense orifices, respectively. On the other hand, it was only 0.1 μM at five meters from Spire orifice, 0.67 μM at 3 meters from Chandelier orifice, and even there is a sharper decrease in Dragon, where cFe-N was measured 0.62 at 1.5 m from the orifice (Yucel et al., 2021). It seems, therefore, although Rainbow fluids creates much more cFe-N at the immediate exist from the orifice, a higher fraction of cFe-N pool is being lost in the rising Rainbow plumes while cFe-N in Broken Spur fluids seems more conservative during the fluids ascend.

In that respect, in order to understand the plume dilution and evolution mechanisms that controls geochemical shift observed in Yucel et al. (2021) for Rainbow and Broken Spur rising plumes, intercorrelations of Fe, Si, Mn, Li, Ca, K and Al were examined for each vent fluids. Additionally, since Mg exhibits a conservative behavior during mixing of endmember hydrothermal fluids with seawater, we preferred to use Mg as a mixing tracer (Figure 4.12 and Figure 4.13). Seawater is rich in Mg while hydrothermal fluid endmembers have near zero Mg concentrations due to reactions of fluids with basalt, gabbro and peridotite at high temperatures and low water/rock ratios (Bischoff and Dickson, 1975; Moitl and Holland, 1978; Seyfried and Bischoff, 1981; Janecky and Seyfried, 1986; Seyfried et al., 2007).

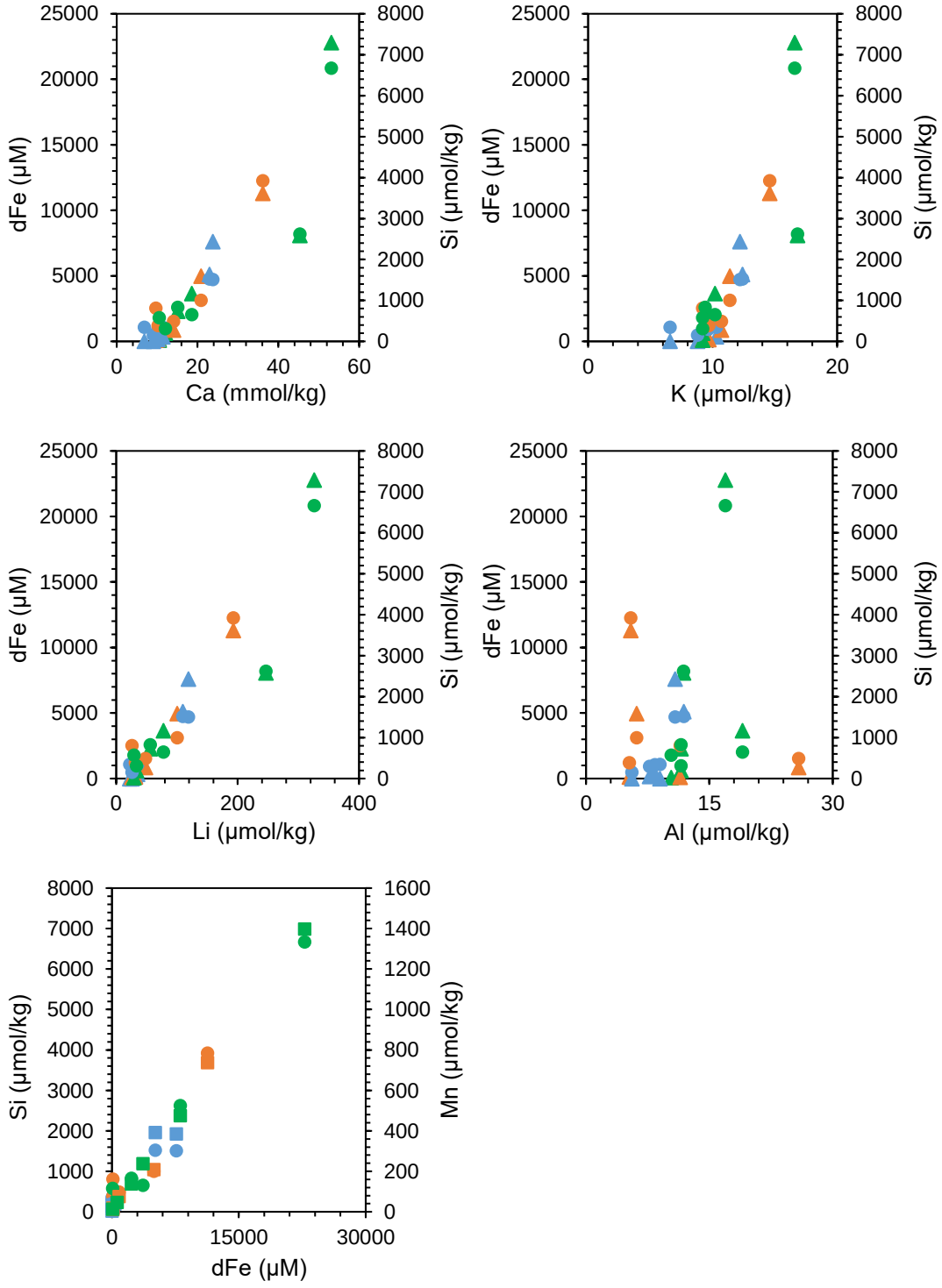

Figure 4.10. Relationship between measured concentration of Fe, Ca, Si, K, Li, Al and Mn in Rainbow hydrothermal plume (Green: Magali; Blue: Fumeur Tres Dense; Orange: Fumeur Nouveau; Triangle: Fe; Circle: Si; Square: Mn)

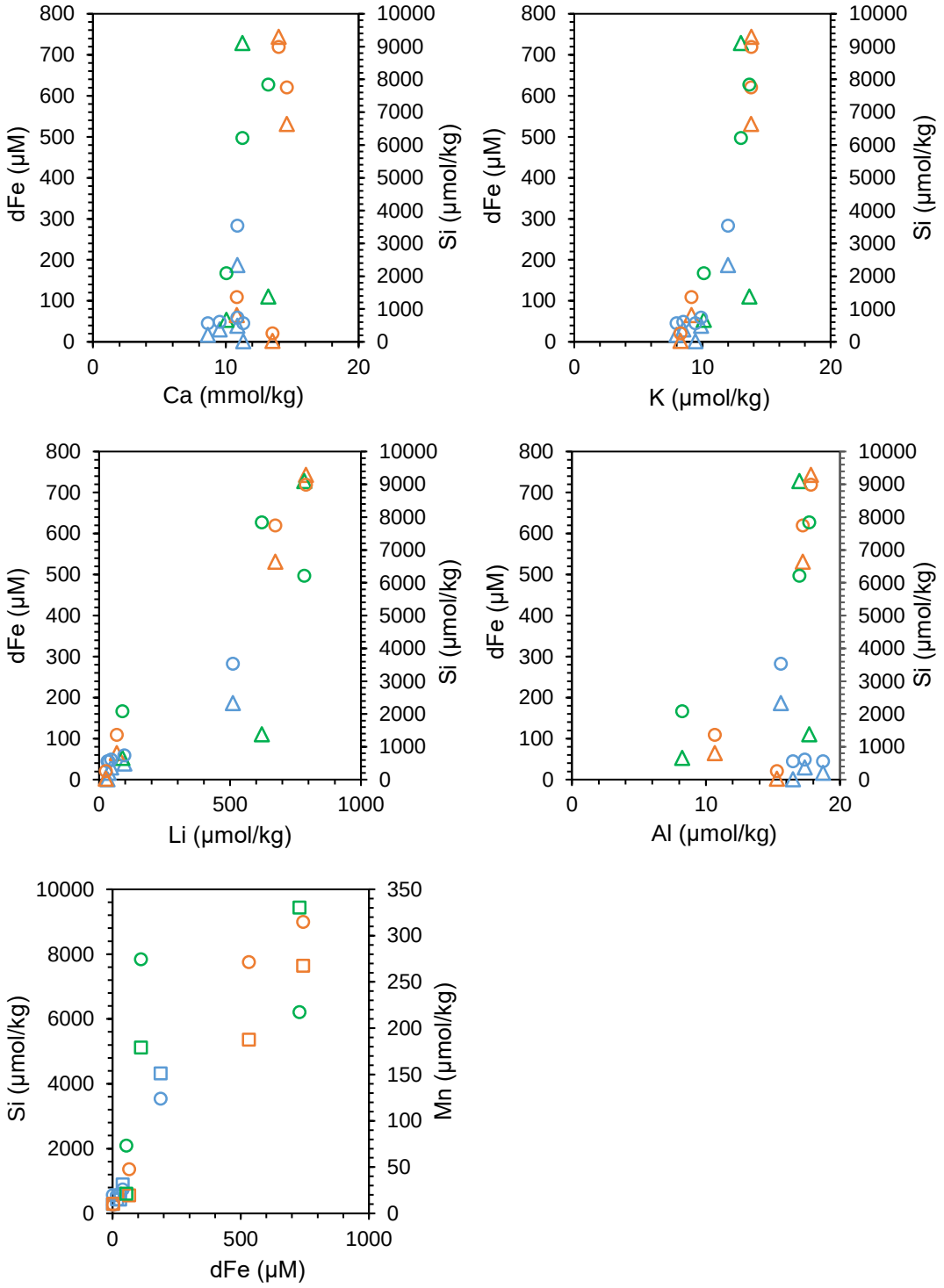

Figure 4.11. Relationship between measured concentration of Fe, Ca, Si, K, Li, Al and Mn in Broken Spur hydrothermal plume (Green: Dragon; Blue: Spire; Orange: Chandelier; Triangle: Fe; Circle: Si; Square: Mn)

Therefore, a mixing line is created between the average endmember fluid compositions of corresponding vent fluid and background seawater composition (e.g. McDermott et al., 2020). Comparison with the mixing line indicates removal and/or enrichment of corresponding element in the fluid.

Table 4.1 Correlation matrix representing R^2 values for some non-volatile dissolved species in Rainbow and Broken Spur hydrothermal plumes (FTD: Fumeur Tres Dense and FN: Fumeur Nouveau)

FTD	**Li**	**K**	**Ca**	**Fe**	**Mn**	**Si**	**Al**
Li	1.00	0.75	0.99	0.97	0.98	0.98	0.70
K		1.00	0.84	0.65	0.67	0.65	0.39
Ca			1.00	0.93	0.95	0.95	0.65
Fe				1.00	0.94	0.93	0.63
Mn					1.00	1.00	0.77
Si						1.00	0.81
Al							1.00
FN	**Li**	**K**	**Ca**	**Fe**	**Mn**	**Si**	**Al**
Li	1.00	0.97	1.00	1.00	0.97	0.88	0.15
K		1.00	0.98	0.95	0.96	0.86	0.07
Ca			1.00	0.99	0.98	0.89	0.12
Fe				1.00	0.97	0.90	0.18
Mn					1.00	0.96	0.13
Si						1.00	0.15
Al							1.00
Magali	**Li**	**K**	**Ca**	**Fe**	**Mn**	**Si**	**Al**
Li	1.00	0.95	1.00	0.87	0.85	0.87	0.14
K		1.00	0.97	0.68	0.67	0.70	0.07
Ca			1.00	0.82	0.80	0.82	0.13
Fe				1.00	1.00	0.98	0.26
Mn					1.00	0.98	0.27
Si						1.00	0.16
Al							1.00

Table 4.1 (continued)

Spire	**Li**	**K**	**Ca**	**Fe**	**Mn**	**Si**	**Al**
Li	1.00	0.88	0.17	0.99	1.00	1.00	0.52
K		1.00	0.49	0.81	0.86	0.88	0.83
Ca			1.00	0.11	0.15	0.17	0.81
Fe				1.00	0.99	0.98	0.46
Mn					1.00	1.00	0.50
Si						1.00	0.53
Al							1.00
Dragon	**Li**	**K**	**Ca**	**Fe**	**Mn**	**Si**	**Al**
Li	1.00	0.85	0.40	0.54	0.92	0.77	0.92
K		1.00	0.78	0.17	0.60	0.99	0.99
Ca			1.00	0.00	0.15	0.86	0.69
Fe				1.00	0.80	0.10	0.26
Mn					1.00	0.50	0.70
Si						1.00	0.96
Al							1.00
Chandelier	**Li**	**K**	**Ca**	**Fe**	**Mn**	**Si**	**Al**
Li	1.00	0.98	0.47	0.98	0.98	1.00	0.62
K		1.00	0.43	0.94	0.93	0.99	0.54
Ca			1.00	0.40	0.43	0.41	0.94
Fe				1.00	1.00	0.98	0.58
Mn					1.00	0.97	0.61
Si						1.00	0.56
Al							1.00

Dissolved Fe in Rainbow and Broken Spur fluids exhibits strong positive correlation with Si and Mn (Figure 4.10 and Figure 4.11) except for Dragon fluids. These strong correlations show that Si is an important actor in iron and manganese geochemistry both in Rainbow and Broken Spur fluids and therefore its geochemical tendency in the plume might resemble to Fe and Mn. Moreover, Figure 12-13 indicates that there is a prominent removal trend nearly for all dissolved species measured from all vents as their fluids mix with ambient seawater. The intense positive correlation between Si and Fe and similar removal trend they both exhibits might be a good evidence supporting Fe and Si possibly precipitate together in the rising plume. Findlay et al.

(2015) indicated that a good amount of Fe (in mM level) would stay in the buoyant plume and might precipitate in, and/or be adsorbed by silicate forms. Additionally, different studies have shown that Si-containing particles are present in hydrothermal vent plumes such as amorphous silica and kaolinite (Feely et al., 1990; Gartman et al. 2014), however, silicate phases are not restricted to only these forms, and Fe containing silicate (nano)particles such as Fe-rich micas, talc and lizardite have been suggested as an important fraction of the plume geochemistry as well (Gartman et al., 2014; Estes et al., 2018; Luther et al., 2020). Similar strong correlations can be seen for different cations in Rainbow and Broken Spur hydrothermal plumes in addition to Si, Mn, and Fe (Figure 4.10 and Figure 4.11). The similar behavior they exhibit altogether supports the idea that a very special set of geochemical reaction, known as reverse weathering, might be responsible for depletion of these species and formation of silicate (nano)particles in the plume. Reverse weathering is defined as authigenic clay formation where metal precipitation in silicate phases occur as a result of reactions between silica and dissolved cations (Reaction 4) (Rahman et al., 2019). Reverse weathering has been mostly studied under the concepts of sediment biogeochemistry however recent advancements put reverse weathering into hydrothermal vent research framework as well (Estes et al., 2018; Luther et al., 2020). Different reverse weathering reactions and their resultant authigenic minerals including Greenalite (Fe-silicate), Minnesotaite (Fe-silicate), Berthierine (Fe-silicate), Glauconite (K, Fe-silicate), Saponite (Ca, Fe-silicate), Corrensite (Ca, K, Fe- silicate) have been proposed previously based on the studies conducted in sedimentary environments (Isson and Planavsky, 2018). Although removal trend of some dissolved cations especially in Rainbow plume along with dissolved Fe and Si is consistent with reverse weathering minerals, further integrative works are required to prove the existence of these minerals in hydrothermal vent plumes. Additionally, unlike most of the cations, Al exhibits no or variable degree of correlation with Fe and Si. Endmember Al concentrations cannot be calculated and formation of Al-bearing silicate minerals in the subsurface might destruct the relationship in the plume. Also, it is not easy to understand the ultimate process in Broken Spur plume

considering the complex character of its removal trends. Therefore, we state that reverse weathering might be an important process in order to generate silicate (nano)particles especially in Rainbow plume and possibly in Broken Spur plume.

(Dissolved silica) + (degraded/ cation-poor aluminosilicates) + (dissolved Fe and/or Al) + (organic C) + (dissolved cations) + (HCO_3^-) ⇒ cation- rich authigenic clay + CO_2 + H_2O (Reaction 4)

Further, oxidation rate of iron in hydrothermal plumes in deep Atlantic waters is very high compared to other basins (e.g. oxidation half-lives of iron are ~17 minutes and ~27 minutes for Rainbow and TAG plumes at MAR, respectively) (Field and Sharel, 2000; Gartman and Findlay, 2020). Different studies already indicated that oxidation products of dissolved iron (Fe-Ox) are important actors of the plume geochemistry since they form a considerable fraction of the Fe pool and act as strong scavengers for different elements (Mottl and McConachy, 1990; Rudnicki and Elderfield, 1993; Field and Sharel, 2000; Feely et al., 1996; Breier et al., 2012; Fitzsimmons et al., 2017; Waeles et al., 2017; Hoffman et al., 2018). Therefore, in addition to Fe-Si forms, Fe-Ox might be responsible for sustaining an important amount of dissolved iron in the rising plume as well. Additionally, Mn assumed to exhibit a conservative behavior during the plume development since its oxidation rate is very slow and it does not tend to precipitate in sulfide phases (Feely et al., 1994b; Breier et al., 2012; Resing et al., 2015). However, our data demonstrates that Rainbow and Broken Spur fluids show Mn depletions with respect to Mg (Figure 4.12 and Figure 4.13). In Rainbow fluids, Findlay et al. (2015) observed similar Mn removal trend within the first 1-meter from vent orifice. It is already showed that Mn removal rate can differ basin to basin and different processes such as microbial oxidation of Mn and scavenging of Mn with particles like Fe-Ox might responsible in Mn removal in the plume (Campbell et al., 1988; Cowen et al., 1990; Dick and Tebo, 2010; Dick et al., 2013). Additionally, Findlay et al. (2015) indicated that Rainbow has much more particulate Mn when compared to other low Fe:H_2S vent fluids (e.g. TAG), and since Mn oxidation is not expected within the first couple of meters from the orifice, major portion of particulate Mn might come from incorporation of Mn into silicate phases

and/or scavenging of Mn by other particles. Strong positive correlation between Mn and Si at Figure 4.10 and similar removal trend they both show at Figure 4.12 might support the idea that Mn and Si are closely related with each other in the rising plume. As a result, relatively higher Mn removal trend starting at shallower heights from the orifice in Rainbow fluids might indicate that oxides and silicates might have pivotal roles in compositional evolution of Rainbow plumes when compared to Broken Spur, where Mn removal is relatively more conservative (Figure 4.11 and 4.13). Moreover, different studies indicated sulfide species with the presence of high concentration of sulfide (i.e. low Fe:H_2S) observing in the vent plumes are responsible in partitioning of Fe into mainly sulfide forms and formation of an important fraction of dissolved iron as Fe-sulfide precipitates in vent fluids (Mottl and McConachy, 1990; Field and Sherrell, 2000). Main controlling mechanism on the formation of Fe bearing sulfide (nano)particles is attributed to Fe:H_2S ratio of the vent fluids (Field and Sherrell, 2000). For example, German et al. (2002) calculated that precipitation of iron with sulfides encompasses 80-90% of dissolved iron removal in low Fe:H_2S 13°N EPR fluids while formation of Fe-Ox particles is responsible for 10-20% of dissolved iron removal. However, Edmonds and German (2004) indicated that high Fe:H_2S character of Rainbow fluids causes only 4% of total Fe precipitate as sulfide minerals. A more recent study conducted by Waeles et al. (2017) showed that relatively smaller fraction of hydrothermal Fe (<10%) is precipitated as sulfide minerals, and Fe oxidation is a major process in removal of hydrothermal iron in vent systems. Nevertheless, different studies agree that Fe-sulfide and Fe-Ox phases are important parts of the plume geochemistry in varying proportions depending on the setting.

As a result, we suggest that Fe-Si and Fe-Ox (nano)particle forms might become an important part of the colloidal pool during the fluid rise for both vent fields. However, still an important fraction of sulfide in Broken Spur might have a primary control on compositional evolution of (nano)particles in the rising plume.

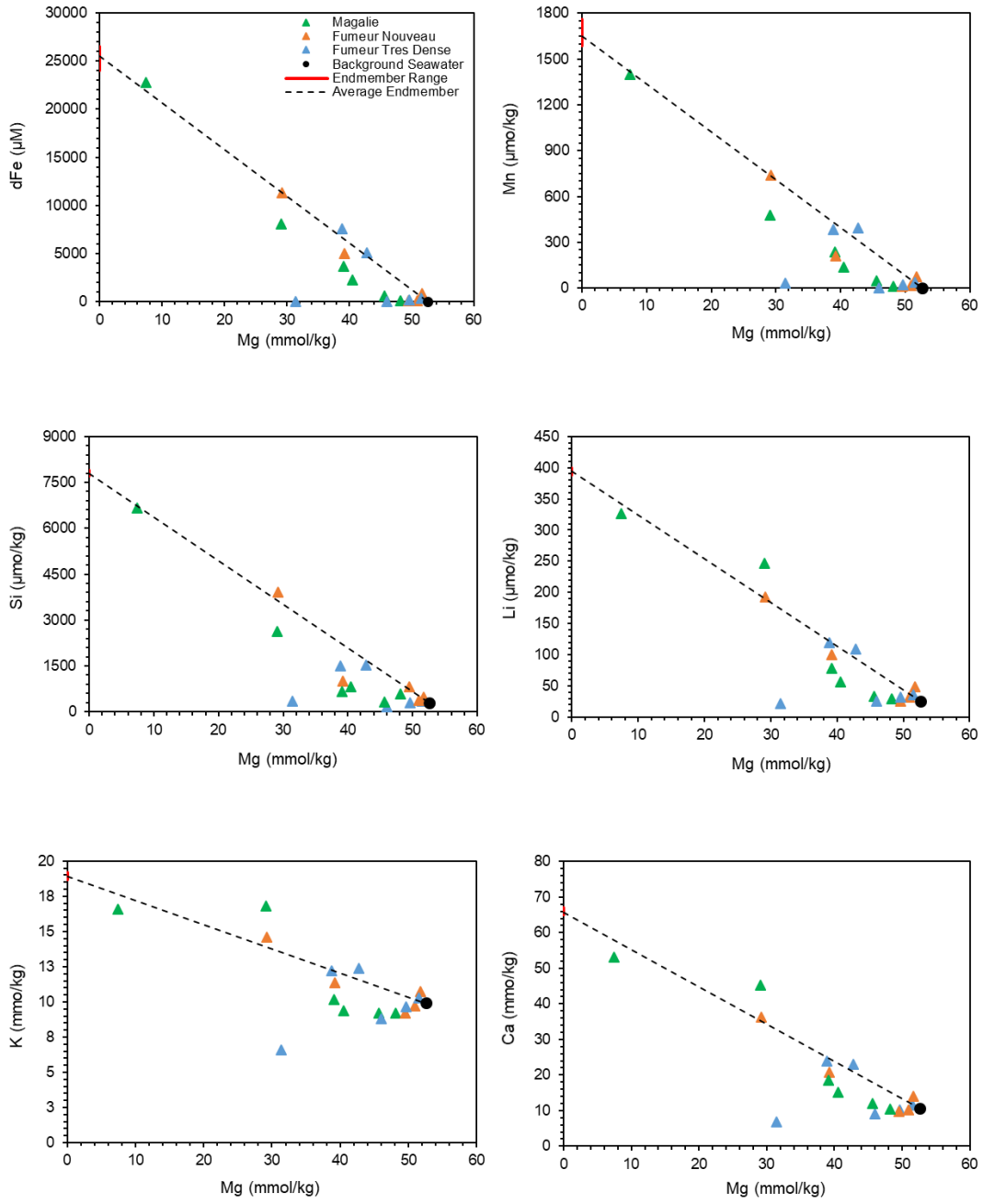

Figure 4.12. Removal plots for Rainbow hydrothermal plume. For each species, the range in extrapolated zero-Mg high temperature endmember composition is shown with the red bar, and the average is shown with a black line projected from seawater composition. Species that exhibit conservative behavior during mixing plot on the line while species that behave non-conservatively plot above or below the line

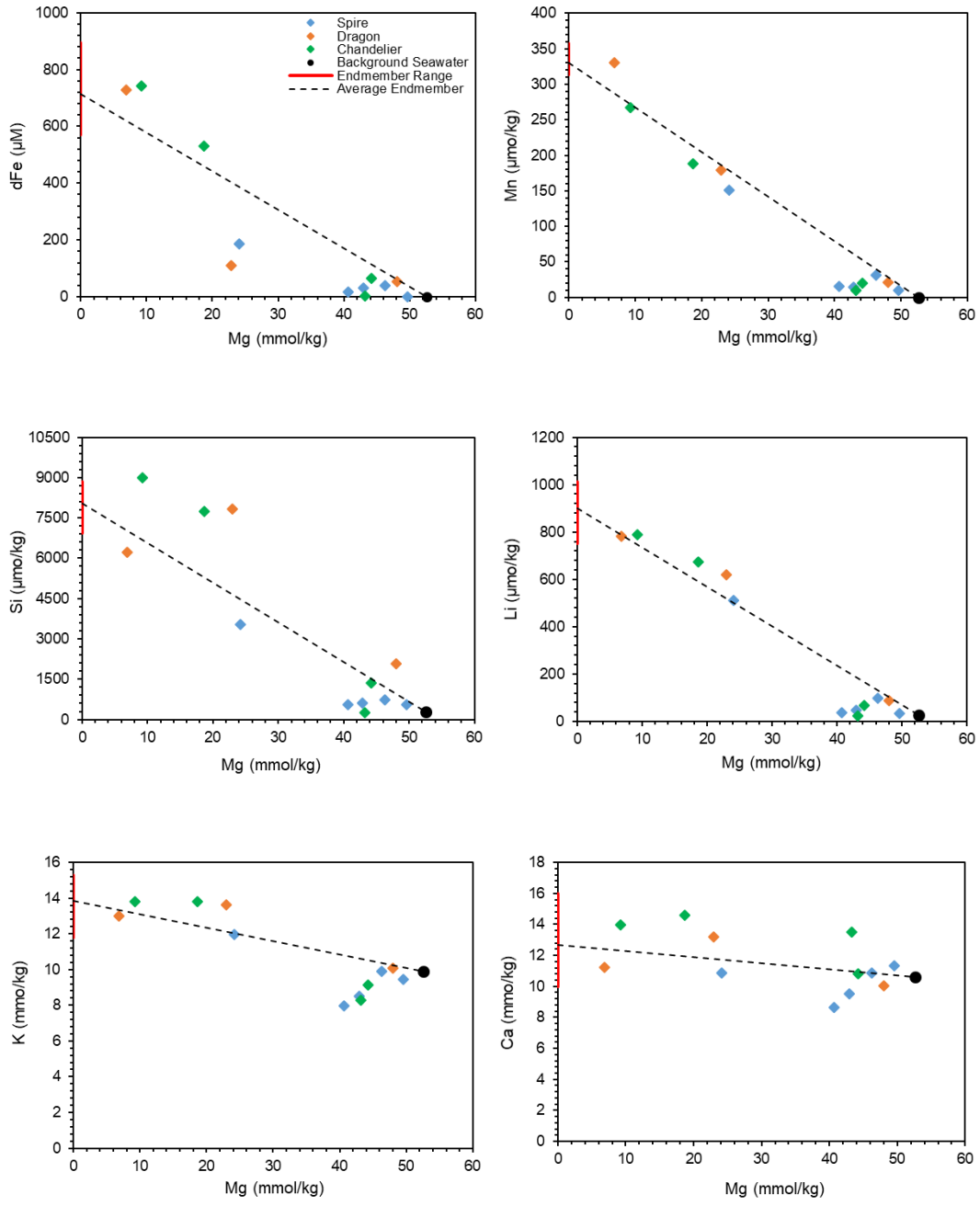

Figure 4.13. Removal plots for Broken Spur plume. For each species, the range in extrapolated zero-Mg high temperature endmember composition is shown with the red bar, and the average is shown with a black line projected from seawater composition. Species that exhibit conservative behavior during mixing plot on the line while species that behave non-conservatively plot above or below the line

We also suggest that Rainbow fluids has much more dynamic environment in the case of cFe-N formation as a result of silicates and oxides forming in the plume while immediate formation and domination of sulfide forms in Broken Spur fluids creates more stable environment for cFe-N. Therefore, a dynamical colloidal pool existing in Rainbow might responsible on creating the shift between observation of very high concentration of cFe-N in the orifice but removal of very large fraction up in the buoyant plume (Figure 4.9). Additionally, metal silicate phases are thought to be not extractable with HCl and HNO_3 treatments (Huerta-Diaz and Morse, 1992), therefore quantitative understanding of cFe-N silicate pool in the rising plume is needed in future studies.

Furthermore, Rainbow vent field is fed by a single deep source in the subsurface as stated in the previous sections. Therefore, comparison of (nano)particle production potential of individual vents in Rainbow will provide valuable information on understanding the main driving factors controlling the formation of these particles. In other words, having similar endmember Fe concentrations and feeding by a single deep source make Rainbow field a perfect analog system to understand contributions of subsurface in comparison with plume processes to examine the formation dynamics of cFe-N. For example, Fumeur Tres Dense and Magali fluids have comparable amounts of cFe-N at immediate exist from the orifice (Figure 4.9), however, it is observed that Fumeur Tres Dense fluids have more intense cFe-N removal as opposed to Magali. Relatively sharper removal of Fe, Mn, Si and cations from Fumeur Tres Dense fluids show that removal rate of cFe-N by creating larger particles in Fumeur Tres Dense is more prominent while Magali fluids have relatively gradual removal trend during fluid mixing (Figure 4.10). This indicates that although starting with a similar concentration of cFe-N, plume processes might create substantial implications on evolution of nanoparticles throughout the plume rising. On the other hand, Fumeur Nouveau seems producing lower concentrations of cFe-N at the orifice relative to other vents in Rainbow field although all three vents are connected in the subsurface. Interestingly, seawater mixing plots of Fumeur Nouveau shows relatively higher conservative behavior unlike Fumeur Tres Dense

and Magali fluids (Figure 4.12). Higher conservative mixing indicates relatively lower particle formation in the rising plume and it is consistent with the data that Fumeur Nouveau fluids can maintain a higher fraction of its cFe-N up in the buoyant plume relative to other vent sites at Rainbow (Figure 4.9).

4.4 Possible Major Implications of Hydrothermal Vent Products in Major Geological Events in the Earth's History

Recent advancements showed that hydrothermal vents are part of the global ocean biogeochemical system and their Fe products, for example, can be transported thousands of kilometers away from hydrothermal vent sources in contrast to old ideas covering immediate precipitation (Resing et al., 2015; Fitzsimmons et al., 2017). Naturally occurring nanoparticles are proposed as one of the fundamental mechanisms which put hydrothermal vent products into the global picture (Yucel et al., 2011; Gartman et al., 2014; Findlay et al., 2015; Findlay et al., 2019; Yucel et al., 2020). Further, Gartman et al. (2019) reported detection of Cu and Zn bearing nanoparticles in addition to Fe in hydrothermal vents as well. By considering major roles of transition metals in biogeochemistry of ocean system -for example, most of the metals participates in the structure of enzymes as a cofactor or iron cycle in the global ocean system is coupled with nitrogen, carbon and phosphorus cycles and play a major role with Zn, Cu and Ni in primary production in different periods of Earth's history (Twining et al., 2013; Rickaby et al., 2015; Moore et al., 2017)- we are proposing hydrothermal vents and their products might have played much more essential roles in major geological events in Earth's history than previously thought. In this final section of this Thesis' discussion, we discuss this concept in two different periods of Earth's history: The Last Glacial Maximum and The Cenomanian-Turonian Anoxic Event.

4.4.1 Last Glacial Maximum (LGM)

There is a net decrease in CO_2 concentration in the atmosphere during the last glacial maximum (LGM), however the main mechanism behind this event is still debated. Nearly all hypotheses in this topic rely on mechanisms of oceanic origin, such as changes in ocean temperature and salinity, reorganization of the thermohaline circulation, changes in carbonate chemistry, enhanced biological pump due to dust fertilization, and effects of sea ice changes however still there is no widely accepted scenario to provide an integrated explanation for the event (Sigman and Boyle, 2000; Sigman et al, 2010, Martínez-García et al, 2014, Lambert et al, 2015). Enhanced biological pump with hydrothermal activity might be another important mechanism but its interplay in global scale has not been considered widely and it might be a much more important controlling mechanism than previously thought. In order to answer this question, variations of hydrothermal activity in glacial/interglacial periods and response of hydrothermal activity to sea level change should be considered. It was stated that mainly lowering the global sea level would reduce hydrostatic pressure on mid-ocean ridge melt centers during the glacial periods and results in increasing melt production which may generate intense hydrothermal venting and thicker oceanic crust during LGM (Lund and Asimov, 2011). On the other hand, Coogan et al. (2019) indicated increasing sea level might result in increasing reaction temperatures and pressures in the subsurface and water/rock reactions and phase separation in that conditions might affect hydrothermal fluxes positively. Nevertheless, there is a direct relationship between global sea level chance and hydrothermal activity in glacial/interglacial transition as indicated in different studies as well (Lund et al, 2016; Middleton et al, 2016; Costa et al, 2017). In these studies, main attention was given to deposits of hydrothermal vent sediments in deep ocean. Geochemical metals proxies (Fe, Mn, Cu etc.) in these deposits gave clues about evolution of hydrothermal activity especially during LGM with respect to changing sea level, and studies clearly demonstrate that hydrothermal activity respond to sea level changes during glacial-interglacial times (Figure 4.14). During

LGM, increasing concentrations of (nano)particle iron could be transported to surface ocean and trigger biological pump with iron fertilization during the period of intense hydrothermal activity. Recent studies by Ardyna et al. (2019) and Schine et al. (2021) supported this idea and indicated that hydrothermal Fe could trigger primary production in the surface waters and cause phytoplankton blooms in Southern Ocean. In that case, biogeochemical oceanographic and climate models should be established in order to understand the transport of biologically important metals in the oceans during glacial periods.

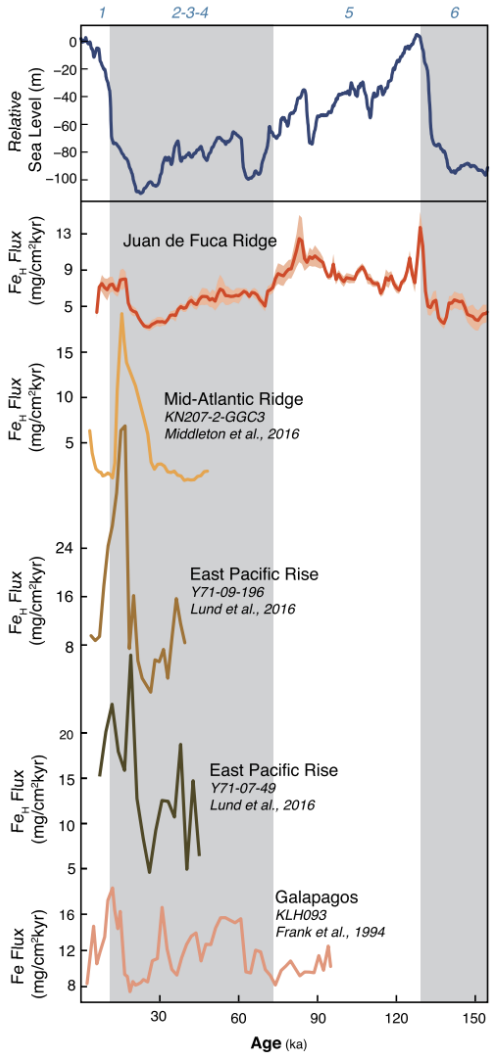

Figure 4.14. Hydrothermal iron flux change across the last glacial maximum (for further details check Costa et al. (2017) and references therein)

It is important to understand this phenomenon because former state of oceans in LGM might be totally different. For example, ocean water temperature is lower approximately 3-5 ˚C than current state (Sigman and Boyle, 2000), which would reduce the density stratification throughout the entire water column. However, formation of ice-caps would reduce the sea level and increase the salinity since most of the surface fresh water content would participate in ice formation. Therefore, it might generate an opposing effect on lowering density stratification. Also, it is proposed that during LGM, entire ocean was 3% saltier than it is today (Sigman and Boyle, 2000). Colder and saltier ocean increase the net ocean density and in a denser medium, deep ocean buoyant hydrothermal plume injection would be transported much more easily. However, in order to understand net effects of each individual parameters, oceanographic models that establish how hydrothermal plumes in ancient LGM oceans are transported should be carried out. Accordingly, new climate models would be established and old models would be revisited since it will help to solve the missing parts of natural events by establishing effects on hydrothermal activity in global scale.

4.4.2 The Cenomanian- Turonian Anoxic Event

The Cenomanian- Turonian boundary event (OAE2) nearly 94 million years ago is one of the significant extinction events in geological history that results in global extinction of 7% of families and 26% of genera in Cretaceous oceans (Twitchett, 2013). Due to intense accumulation of black shales in oceanic, epicontinental and shelf sediments all around the world, bottom water anoxia in global scale was attributed as the main driving factor for the extinction event. Enhanced primary production in the surface waters is the most accepted explanation for OAE2 but reasons behind the global scale eutrophism are still debated. Erba (2004) stated that although local upwelling and coastal nutrification might provide some explanations, they are not capable of describing high productivity in global scale. Therefore, it was proposed that primary production rate could be increased under the control of iron

fertilization by hydrothermal activity. Intense submarine volcanism in Large Igneous Provinces (LIPs) such as Caribbean and Ontong-Java oceanic plateaus and the Madagascar flood basalt, which roughly coincide with C/T boundary were proposed as the main driving factors for the event (Sinton and Duncan, 1997; Kerr, 1998, Leckie et al., 2002). Injection of hydrothermal Fe into water column as a bio-limiting nutrient could increase the rate of primary production, and caused drawdown of O_2 in seawater. Sudden decrease in $^{87}Sr/\ ^{86}Sr$ ratio from the Cenomanian-Turonian boundary through the upper Turonian (Bralower et al., 1997; Jones and Jenkyns, 2001) and relative increase in concentrations of trace elements including Sc, Ti, V, Cr, Mn, Co, Ni, Ir, Pt, and Au in both black shales and carbonates at the C/T boundary (Orth et al., 1993) are some evidences that indicate the effect of submarine hydrothermalism.

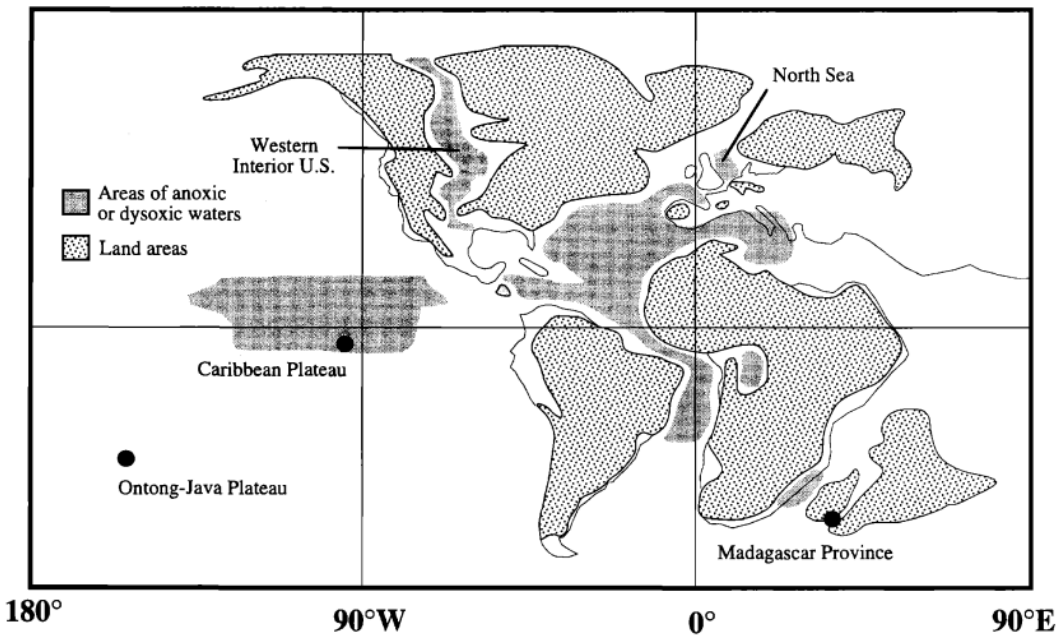

Figure 4.15. Paleogeographic map of Earth ~90 million years ago. Areas representing anoxic conditions were indicated in shaded gray color (Sinton and Duncan, 1997)

Jones and Jenkyns (2001) discussed different possible sources of Sr isotopes and effects of riverine input and seafloor hydrothermalism, and they decided that effects

of hydrothermal Sr isotopes was more dominant at C/T boundary. Moreover, Cenomanian-Turonian boundary exhibit signatures regarding global sea surface temperature rise by 6 to 14 ^{o}C higher than today. Such conditions could create relatively low equator to pole temperature gradient and resultant weaker water column density stratification in the oceans at that time (Leckie et al., 2002). Under these conditions, considering general existence and long-distance transport capability of (nano)particles, hydrothermal vents might have played substantial roles in increasing the rate of primary production in C/T boundary event. That is, due to increasing rates of vertical advection, hydrothermal (nano)particles might be more easily injected to euphotic zone and make significant contributions to surface productivity, hence to the global anoxic event.

CHAPTER 5

CONCLUSION

This thesis aims to understand formation and evolution of hydrothermal vent fluids from Rainbow, Broken Spur and Lost City hydrothermal vent fields. For this goal, vent fluid samples were collected during the TRANSECT research cruise to Mid-Atlantic Ridge with N/O L'Atalante and ROV Victor in 2018. Measurements regarding concentrations of major ions, transition metals and hydrogen sulfide were conducted and a multi elemental dataset were generated for each hydrothermal field. By using measurement results, endmember fluid compositions were calculated accordingly.

Calculations showed that Rainbow, Broken Spur and Lost City hydrothermal vent fields contain compositionally distinct vent fluids. For example, Rainbow exhibits great enrichments of Cl with respect to ambient seawater while Broken Spur contains Cl- depleted fluids. Super-critical and sub-critical phase separations that Rainbow and Broken Spur fields experience, respectively are the main reason for the Cl variations. Cl in the hydrothermal fluids has been used to estimate subsurface reaction conditions (e.g. Gallant and Von Damm, 2006; Charlou et al.,2010; Reeves et al., 2011; McDermott et al., 2018). Accordingly, we calculated subsurface reaction temperature and pressure conditions ~420 °C and ~340 bars for Rainbow and 400-405 °C and 280-290 bars in Broken Spur. Both calculated temperatures are higher than what was measured in the orifice therefore we inferred extensive cooling (105 °C for Rainbow and 95°C for Broken Spur) during the fluid rise in the up-flow zone. Moreover, negative endmember SO_4 concentrations for Fumeur Tres Dense (FTD) and Fumeur Nouveau (FN) fluids in Rainbow indicate that these vents experience seawater mixing in the subsurface. Mixing of cold (~4 °C) seawater with hot hydrothermal fluids explains why FTD and FN have lower exit temperatures (315-320 °C) when compared to Magali (372 °C). Additionally, Na/Cl and Ca/Cl

dynamics claim that intense albitization is responsible for Ca enrichments in Rainbow fluids while Broken Spur and Lost City do not exhibit substantial albitization although Lost City contains Ca-enriched fluids. Seyfried et al. (2008) indicated that this Ca enrichment in Lost City might be sustained by dissolution of clinopyroxene minerals. Furthermore, alkali element enrichments (e.g. K and Li) and low water/rock ratio dynamics show that reactions between water and fresh basalts control the formation and evolution of hydrothermal fluids in Broken Spur vent field however it is not the case for Lost City since its water/rock ratio is high. On the other hand, Rainbow has a more complex system and water/rock reactions are controlled by variable water/rock ratios in Rainbow field. Moreover, both Rainbow and Broken Spur fluids exhibit great enrichments of Si with respect to ambient seawater while Lost City has similar concentrations. In a normal case, it is not expected to have high concentration of silica in a peridotite hosted system (Allen and Seyfried, 2003) therefore we propose, in conjunction with previous studies, interaction with gabbroic intrusions provide extra dissolved Si for Rainbow fluids. Most importantly, Rainbow contains metal rich and sulfide poor fluids whereas it is the opposite case for Broken Spur. Cl is the dominant ion in the hydrothermal fluids and it controls metal transportation with chloro-complexes. Therefore, sulfide and Cl dynamics seen in both vent field control the ultimate fate of metal transport in hydrothermal fluids. As a result, Broken Spur fluids have a concentration range observed in most of the basalt hosted systems in the case of Fe while Rainbow contains the highest endmember Fe concentration in global scale (Figure 4.4). Furthermore, comparison of time series data show that Rainbow and Lost City fluids are stable in ~20 years' time span, which indicates there are no major changes in subsurface physico-chemical conditions in Rainbow and Lost City vent fields. On the other hand, Broken Spur fluids experience substantial fluctuations, especially in Fe concentration, over time. Calculation showed that reaction depth and temperature did not change substantially between 1993 and 2018 however there is temperature decreasing trend over time. Therefore, we are proposing that substantial removal of Fe can be sustained by extensive conductive cooling that Broken Spur have been experienced over time.

Additionally, the lowest calculated endmember Si concentrations of Broken Spur when compared to other basalt hosted systems in MAR (Charlou et al., 2010) indicate that Si might be precipitating in the subsurface along with Fe considering highly sensitive character of its solubility to temperature change. By using method proposed by Von Damm (1991), we calculated that up to 50% of Si is removed during fluid rise in the up-flow zone as a result of cooling. Finally, intercomparison between individual vent sites showed that Rainbow and Broken Spur fields exhibit low spatial variations. That is why both Rainbow and Broken Spur vents are fed by a single deep source in the subsurface.

In order to link subsurface conditions to impact to the deep-sea, samples were taken from different heights in Rainbow and Broken Spur hydrothermal plumes starting from the orifice in order to understand geochemical dynamics of hydrothermal plumes. High correlation of Fe, Mn, Si and cations indicate that these species are interconnected with each other in Rainbow and Broken Spur rising plumes. Therefore, the fate of most of the species in the plume such as Fe, Mn and Si are controlled by some special set of geochemical reactions (e.g. reverse weathering, oxidation etc.) and their resultant mineral formations. For example, considering the removal trend of Fe, predominance of sulfide species is expected in the Broken Spur plume due to the low Fe:H_2S character while oxidation products might be common in high Fe:H_2S Rainbow fluids. Additionally, relatively higher removal Mn trend in Rainbow when compared to Broken Spur indicates that oxides and silicates might have a prominent role in Rainbow plume. As a result, we propose that oxides and silicate bearing (nano)particles might be an important fraction of Rainbow fluids while evolution of Broken Spur fluids are mainly controlled by formation and domination of sulfide bearing species. Moreover, recent studies showed that hydrothermal products might be much more important for global ocean biogeochemistry than previously thought (Resing et al., 2015; Fitzsimmons et al., 2017). Therefore, by putting the biologically important hydrothermal (nano)particles at the center, we are proposing that hydrothermal vents might have played very important roles in Earth's history. For example, we suggest hydrothermally induced

primary production enhancement in the ocean during las glacial maximum might be an alternative mechanism to explain the CO_2 depletion in that time in conjunction with other proposed mechanisms. Findings covering hydrothermal flux change with changing seawater level in the geological time (Lund et al, 2016; Middleton et al, 2016; Costa et al, 2017) and increasing primary production in the surface waters in Southern Ocean by hydrothermal activity (Ardyna et al., 2019; Schine et al., 2021) are two important supporting that statement for this idea. Another important event that might be triggered by hydrothermalism might be The Cenomanian- Turonian Anoxic Event in ~94 million years ago. During that time, Cretaceous oceans faced with global extinction of 7% of families and 26% of genera as a result of global anoxia (Twitchett, 2013). That is why we are proposing that biologically important hydrothermal (nano)particles transported to surface waters of Cretaceous oceans might have triggered this event. Enrichments of trace elements and Sr isotope dynamics support the enhancement of hydrothermal flux during Cenomanian-Turonian time span (Orth et al., 1993; Bralower et al., 1997; Jones and Jenkyns, 2001). However, roles and contributions of hydrothermal products both in modern and ancient systems should be quantitatively understood in further studies in the future.

REFERENCES

Allen, D. E., and Seyfried, W. E. (2004). Serpentinization and heat generation: Constraints from Lost City and Rainbow hydrothermal systems, Geochim. Cosmochim. Acta, 68(6), 1347–1354.

Alt J. C. (1995). Subseafloor processes in mid-ocean ridge hydrothermal systems. Geophys. Monogr. (AGU) 91, 85–114.

Andreani M., Escartin J., Delacour A., Ildefonse B., Godard M., Dyment J., Fallick A. E. and Fouquet Y. (2014). Tectonic structure, lithology, and hydrothermal signature of the Rainbow massif (Mid-Atlantic Ridge 36°14'N). Geochem. Geophys. Geosyst. 15, 3543–3571.

Ardyna, M., Lacour, L., Sergi, S., d'Ovidio, F., Sallée, J.B., Rembauville, et al. (2019). Hydrothermal vents trigger massive phytoplankton blooms in the Southern Ocean. Nat. Commun. 10:2451. doi: 10.1038/s41467-019-09973-6.

Augustin, N., Paulick, H., Lackschewitz, K. S., Eisenhauer, A., Garbe Schonberg, D., Kuhn, T., Botz, R. and Schmidt, M. (2012). Alteration at the ultramafic-hosted Logatchev hydrothermal field: constraints from trace element and Sr–O isotope data. Geochemistry, Geophysics, Geosystems 13, Q0AE07. doi: 10.1029/2011GC003903.

Bach, W., Garrido, C. J., Paulick, H., Harvey, J., and Rosner, M. (2004). Seawater-peridotite interactions: First insights from ODP Leg 209, MAR 15°N, Geochem. Geophys. Geosyst., 5, Q09F26, doi:10.1029/2004GC000744.

Ballard, R.D. and Grassle, J.F. (1979). Return to Oases of the Deep. National Geographic, 156(5): 684-703.

Baker, E.T., Chen, Y.J., Morgan, J.P. (1996). The relationship between near-axis hydrothermal cooling and the spreading rate of mid-ocean ridges, Earth and Planetary Science Letters, 142, 1–2, 137-145, doi.org/10.1016/0012-821X(96)00097-0.

Baker E.T. and German C. (2004). On the global distribution of hydrothermal vent fields. In: German CR, Lin J, and Parson LM (eds.) Mid-Ocean Ridges: Hydrothermal Interactions between the Lithosphere and Ocean, Geophysical Monograph Series, vol. 148, pp. 245–266. Washington, DC: American Geophysical Union.

Baker E.T., Resing J.A, Walker S.L., Martinez F., Taylor B., and Nakamura K. (2006). Abundant hydrothermal venting along melt-rich and melt-free ridge segments in the Lau back-arc basin. Geophysical Research Letters 33: L07308.

Beaulieu, Stace E; Szafrański, Kamil M. (2020). InterRidge Global Database of Active Submarine Hydrothermal Vent Fields Version 3.4. PANGAEA, https://doi.org/10.1594/PANGAEA.917894.

Bennett S. A., Achterberg E. P., Connelly D. P., Statham P. J., Fones G. R. and German C. R. (2008). The distribution and stabilisation of dissolved Fe in deep-sea hydrothermal plumes. Earth Planet. Sci. Lett. 270, 157–167.

Berndt M. E., Seyfried, Jr., W. E. and Janecky D. R. (1989). Plagioclase and epidote buffering of cation ratios in mid-ocean ridge hydrothermal fluids: experimental results in and near the supercritical region. Geochim. Cosmochim. Acta 53, 2283–2300.

Berndt M.E. and Seyfried W.E. (1993). Calcium and sodium exchange during hydrothermal alteration of calcic plagioclase at 400 °C and 400 bars. Geochimica et Cosmochimica Acta 57: 4445–4451.

Bischoff, J.L. and Dickson, F. (1975). Seawater-basalt interaction at 200°C and 500 bars: implications for origin of sea-floor heavy-metal deposits and regulation of seawater chemistry. Earth and Planetary Science Letters 25, 385-397. doi: 10.1016/0012-821X(75)90257-5.

Bischoff J.L. and Seyfried W.E. (1978). Hydrothermal chemistry of seawater from 25 degrees to 350 degrees C. American Journal of Science 278: 838–860.

Bischoff J. L. and Rosenbauer R. J. (1985). An empirical equation of state for hydrothermal seawater (3.2% NaCl). Am. J. Sci. 285, 725–763.

Bischoff, J. L., and Rosenbauer, R. J. (1988). Liquid-vapor relations in the critical region of the system NaCl-H2O from 380 to 415°C: A refined determination of the critical point and two-phase boundary of seawater, Geochim. Cosmochim. Acta, 52, 2121 – 2126.

Bischoff J. L. and Pitzer K. S. (1989). Liquid-vapor relations for the system NaCl–H_2O: summary of the P–T–x surface from 300 deg to 500 deg C. Am. J. Sci. 289, 217–248.

Bischoff, J. L. (1991). Densities of liquids and vapors in boiling NaCl-H_2O solutions: A PVTX summary from 300 to 500°C, Am. J. Sci., 291, 309 – 338.

Breier, J.A., Toner, B.M., Fakra, S.C., Marcus, M.A., White, S.N., Thurnherr, A.M., et al. (2012). Sulfur, sulfides, oxides and organic matter aggregated in submarine hydrothermal plumes at 9°50′N East Pacific Rise. Geochem. Cosmochim. Acta 88, 216–236. doi: 10.1016/j.gca.2012.04.003.

Boschi C., Dini A., Fruh-Green G. L. and Kelley D. S. (2008). Isotopic and element exchange during serpentinization and metasomatism at the Atlantis Massif (MAR 30°N): insights from B and Sr isotope data. Geochim. Cosmochim. Acta 72, 1801–1823.

Bostrom K., Peterson M. N. A., Joensuu O., and Fisher D. E. (1969). Aluminium-poor ferromanganoan sediments on active ocean ridges. J. Geophys. Res. 74, 3261–3270.

Bralower, T. J., Fullagar, P. D., Paull, C. K., Dwyer, G. S., and Leckie, R. M. (1997). Mid-Cretaceous strontium-isotope stratigraphy of deep-sea sections, Geol. Soc. Am. Bull., 109, 1421–1442.

Butterfield, D. A., and G. J. Massoth (1994). Geochemistry of North Cleft Segment vent fluids: Temporal changes in chlorinity and their possible relation to recent volcanism, J. Geophys. Res., 99, 4951 – 4968.

Campbell, A. C., M. R. Palmer, G. P. Klinkhammer, T. S. Bowers, S. Humphris, P. Rona, and J. A. Karson (1988). Chemistry of hot springs on the Mid-Atlantic Ridge, Nature, 335, 514–519.

Carbotte, S. and Macdonald, K. (1992). East Pacific Rise 8°-10° 30'N: Evolution of ridge segments and discontinuities from SeaMARC II and three-dimensional magnetic studies, J. Geophys. Res., 97, 6959–6982, doi:10.1029/91JB03065.

Cave R. R., German C., Thonpson J. and Nesbitt R. W. (2002). Fluxes to sediments underlying the Rainbow hydrothermal plume at 36°14 N on the Mid-Atlantic Ridge. Geochim. Cosmochim. Acta 66, 1905–1923.

Charlou, J. L., et al. (1996a). Methane degassing, hydrothermal activity and serpentinization between the Fifteen-Twenty Fracture Zone area and the Azores Triple Junction area (Mid-Atlantic Ridge), Mid-Atlantic Ridge Symposium, June 19–22, 1996, Reykjavik, Iceland, J. Conf. Abs., 1, 771–772.

Charlou, J. L., Donval, J. P., Douville, E., Jean-Baptiste, P., Knoery, J., Fouquet, Y., Dapoigny, A., and Stievenard, M. (2000). Compared geochemical signature and evolution of Menez Gwen (37°50 N) and Lucky Strike (37°17 N) hydrothermal fluids, south of the Azores Triple Junction on the Mid-Atlantic Ridge, Chem. Geol., 171, 49–75.

Charlou J. L., Donval J. P., Fouquet Y., Jean-Baptiste P., Holm N. (2002). Geochemistry of high H_2 and CH_4 vent fluids issuing from ultramafic rocks at the Rainbow hydrothermal field (36°14′N, MAR). Chem. Geol. 191(4), 345–359. doi: 10.1016/S0009-2541(02)00134-1.

Charlou, J. L., Donval J. P., Konn, C., Ondréas, H., Fouquet, Y. (2010). High Production and Fluxes of H_2 and CH_4 and Evidence of Abiotic Hydrocarbon Synthesis by Serpentinization in Ultramafic-Hosted Hydrothermal Systems on the Mid-Atlantic Ridge, In: Rona PA, Devey CW, Dyment J, Murton BJ (eds). Diversity of Hydrothermal Systems on Slow Spreading Ocean Ridges. American Geophysical Union Monograph Series 188, pp 265-295, Washington, DC: AGU.

Chavagnac, V., Leleu, T., Fontaine, F., Cannat, M., Ceuleneer, G. (2018). Spatial variations in vent chemistry at the lucky strike hydrothermal Mid-Atlantic Ridge (37°N): updates for subseafloor flow geometry from the newly discovered capelinhos vent. Geochemistry, Geophys. Geosystems 19, 4444 4458 doi.org/10.1029/2018GC007765.

Clarke W. B., Beg M. A., and Craig H. (1969). Excess 3He in the sea: evidence for terrestrial primordial helium. Earth Planet. Sci. Lett. 6, 213–220.

Cline, J. D. (1969). Spectrophotometric determination of hydrogen sulfide in natural waters. Limnology & Oceanography, 14(3), 454–458.

Costa, K. M., McManus, J. F., Middleton, J. L., Langmuir, C. H., Huybers, P. J., Winckler, G., and Mukhopadhyay, S. (2017). Hydrothermal deposition on Juan de Fuca Ridge over multiple glacialinterglacial cycles. Earth and Planetary Science Letters, 479, 120-132.

Coogan, L. A., Seyfried, W. E. and Pester, N. J. (2019). Environmental controls on mid-ocean ridge hydrothermal fuxes. Chem. Geol. 528, 119285.

Corliss J. B., Dymond J., Gordon, K.I., Edmond, J.M., Herzen, R.P.V., Ballard, R.D., Green, K., Williams, D., Bainbridge, A., Crane, K. and Vanandel, T.H. (1979). Submarine Thermal Springs on the Galapagos Rift. Science, 203(4385): 1073-1083.

Costa, K. M., McManus, J. F., Middleton, J. L., Langmuir, C. H., Huybers, P. J., Winckler, G., and Mukhopadhyay, S. (2017). Hydrothermal deposition on the Juan de Fuca Ridge over multiple glacial-interglacial cycles. Earth and Planetary Science Letters, 479, 120-132.

Cowen J. P., Massoth G. J., Feely R. A. (1990). Scavenging rates of dissolved manganese in a hydrothermal vent plume. Deep-Sea Res. 37, 1619–1637. doi: 10.1016/0198-0149(90)90065-4.

Decitre, S. E., Deloule, E., Reisberg, L., James, R., Agrinier, P., and Mevel, C. (2002). Behavior of Li and its isotopes during serpentinization of oceanic peridotites, Geochem. Geophy. Geosy., 3, 1.

Denny, A.R., Kelley, D.S., and Früh-Green, G.L. (2015). Geologic evolution of the Lost City Hydrothermal Field: Geochemistry Geophysics Geosystems, v. 17, p. 375–394, https://doi .org/10.1002/2015GC005869.

Dick, G. J., and Tebo, B. M. (2010). Microbial diversity and biogeochemistry of the Guaymas deep-sea hydrothermal plume. Environ. Microbiol. 12, 1334–1347. doi: 10.1111/j.1462-2920.2010.02177.x.

Dick, G., Anantharaman, K., Baker, B.J., Li, M., Reed, D.C., Sheik, C.S. (2013). The microbiology of deep-sea hydrothermal vent plumes: ecological and biogeographic linkages to seafloor and water column habitats. Front. Microbiol. 4, 124. doi: 10.3389/fmicb.2013.00124.

Diehl, A. and Bach, W. (2020). MARHYS (MARine HYdrothermal Solutions) Database: A global compilation of marine hydrothermal vent fluid, end member, and seawater compositions. Geochemistry, Geophysics, Geosystems. 21, e2020GC009385. doi. org/10.1029/2020GC009385.

Ding, K., Seyfried Jr., W.E. (1992). Determination of Fe –Cl complexing in the low pressure supercritical region (NaCl fluid): iron solubility constraints on pH of subseafloor hydrothermal fluids. Geochim. Cosmochim. Acta 56, 3681 – 3692.

Douville, E., J. L. Charlou, J. P. Donval, J. Knoery, Y. Fouquet, P. Bienvenu, P. Appriou, and the FLORES scientific party (1997). Trace elements in fluids from the new Rainbow hydrothermal field (36°14 ’N, MAR): A comparison with other Mid-Atlantic Ridge fluids, Eos Trans. AGU, 78, 832.

Douville, E., Charlou, J.L., Oelkers, E.H., Bienvenu, P., Jove Colon, C.F., Donval, J.P., et al. (2002). The rainbow vent fluids (36°14’N, MAR): the influence of ultramafic rocks and phase separation on trace metal content in Mid-Atlantic Ridge hydrothermal fluids. Chem. Geol. 184, 37-48.

Edmond J. M., Measures C. I., McDuff R. E., Chan L. H., Collier R., Grant B., Gordon L. I., and Corliss J. B. (1979). Ridge crest hydrothermal activity and the balances of the major and minor elements in the ocean: the Galapagos data. Earth Planet. Sci. Lett. 46, 1–18.

Edmonds, H.N., German, C.R. (2004). Particle geochemistry in the Rainbow hydrothermal plume, Mid-Atlantic Ridge. Geochim. Cosmochim. Acta 68, 759–772. doi: 10.1016/S0016-7037(03)00498-8.

Elderfield, H., et al. (1993). Preliminary geochemical results from the Broken Spur hydrothermal field, 29°N, Mid-Atlantic Ridge, Eos Trans. AGU, 74, 99.

Erba, E. (2004). Calcareous nannofossils and Mesozoic oceanic anoxic events, Marine Micropaleontol., 52, 85–106.

Escartín, J., Mével, C., MacLeod, C. J., and McCaig. A. M. (2003). Constraints on deformation conditions and the origin of oceanic detachments: The Mid-Atlantic Ridge core complex at 15°45’N, Geochem. Geophys. Geosys., 4(8), 1067, doi:10.1029/2002GC000472.

Escartín, J., Smith, D. K., Cann, J., Schouten, J., Langmuir, C. H., and Escrig, S. (2008). Central role of detachment faults in accretion of slow-spreading oceanic lithosphere, Nature, 455, doi:10.1038/ nature07333.

Estes, E. R., Berti, D., Hochella, M. F., Jr., Findlay, A., Gartman, A., et al. (2018). Production and Transport of Fe- and Mg-bearing Silicate Nanoparticles in Hydrothermal Fluids at the East Pacific Rise (9°50' N). American Geophysical Union. 10-14 December 2018. Washington, D.C., USA. Abstract retrieved from SAO/NASA Astrophysics Data System.

Eason, D. E., Dunn, R. A., Canales, J. P. and Sohn, R. A. (2016). Segment-scale variations in seafloor volcanic and tectonic processes from multibeam sonar imaging, Mid-Atlantic Ridge Rainbow region, Geochem. Geophys. Geosyst.,17, 3560–3579, doi:10.1002/2016GC006433.

Feely R. A., Geiselman T. L., Baker E. T. and Massoth G. W. (1990). Distribution and Composition of Hydrothermal Plume Particles from the ASHES Vent Field at Axial Volcano, Juan de Fuca Ridge. J. Geophys. Res. 95, 12855–12873. doi: 10.1029/JB095iB08p12855.

Feely R. A., Massoth G. J., Trefry J. H., Baker E. T., Paulson A. J., and Lebon G. T. (1994b). Composition and sedimentation of hydrothermal plume particles from North Cleft segment, Juan de Fuca Ridge. J. Geophys. Res. 99, 4985–5006.

Feely, R.A., Baker, E.T., Marumo, K., Urabe, T., Ishibashi, J., Gendron, J., et al. (1996). Hydrothermal plume particles and dissolved phosphate over the superfast-spreading southern East Pacific Rise. Geochim. Cosmochim. Acta 60, 2297–2323. doi: 10.1016/0016-7037(96)00099-3.

Field, M.P. and Sherrell, R.M. (2000). Dissolved and particulate Fe in a hydrothermal plume at 9°45′N, East Pacific Rise: slow Fe (II) oxidation kinetics in Pacific plumes. Geochim. Cosmochim. Acta 64, 619-628. doi: 10.1016/S0016- 7037(99)00333-6.

Findlay, A.J., Gartman, A., Shaw, T.J., Luther, G.W. (2015). Trace metal concentration and partitioning in the first 1.5 m of hydrothermal vent plumes along the Mid-Atlantic Ridge: TAG, Snakepit, and Rainbow. Chem. Geol. 412, 117–131. doi: 10.1016/j.chemgeo.2015.07.021.

Findlay, A.J., Estes, E.R., Gartman, A., Yucel, M., Kamyshny, A., Luther III, G.W. (2019). Iron and sulfide nanoparticle formation and transport in nascent hydrothermal vent plumes. Nat Commun 10, 1597. doi: 10.1038/s41467-019-09580-5.

Fitzsimmons, J.N., John, S.G., Marsay, C.M., Hoffman, C.L., Nicholas, S.L., Toner, B.M., et al. (2017). Iron persistence in a distal hydrothermal plume supported by dissolved-particulate exchange. Nat. Geosci. 10, 195–201. doi: 10.1038/ngeo2900.

Foustoukos D. I. and Seyfried, Jr., W. E. (2005). Redox and pH constraints in the subseafloor root zone of the TAG hydrothermal system, 26°N Mid-Atlantic Ridge. Earth Planet. Sci. Lett. 235, 497–510.

Foustoukos D. I. and Seyfried, Jr., W. E. (2007b). Fluid phase separation processes in submarine hydrothermal systems. Rev. Mineral. Geochem. 65, 213–239.

Foustoukos D. I., Savov I. P. and Janecky D. R. (2008). Chemical and isotopic constraints on water/rock interactions at the Lost City hydrothermal field, 30°N Mid-Atlantic Ridge. Geochim. Cosmochim. Acta 72, 5457–5474.

Fouquet Y., Charlou J. L., Ondreas H., Radford-Knoery J., Donval J. P., Douville E., Appriou R., Cambon P., Pell H., Landure J. Y., Normand A., Ponsevera E., German C. R., Parson L. M., Barriga F. J. A. S., Costa I. M. A., Relvas J. M. R. S. and Ribeiro A. (1997). Discovery and first submersible investigations on the Rainbow hydrothermal field on the MAR (36140 N). Trans. Am. Geophys. Union (EOS) 78 (46, Suppl.), 832.

Früh-Green, G. L., Kelley, D. S., Bernasconi, S. M., Karson, J. A., Ludwig, K. A., Butterfield, D. A., Boschi, C., and Prokurowski, G. (2003). 30,000 years of hydrothermal activity at the Lost City vent field, Science, 301, 495–498.

Früh-Green, G. L., Connolly, J. A. D., Plas, A., Kelley, D. S., and Grobéty, B. (2004). Serpentinization of oceanic peridotites: Implications for geochemical cycles and biological activity, in The Subseafloor Biosphere at Mid-Ocean Ridges, Geophys. Monogr. Ser., vol. 144, edited by W. S. D. Wilcock et al., pp. 119–136, AGU, Washington, D. C.

Früh-Green, G.L., Orcutt, B.N., Rouméjon, S., et al. (2018). Magmatism, serpentinization and life: Insights through drilling the Atlantis Massif (IODP Expedition 357), Lithos, 323, 137-155.

Gallant R. M. and Von Damm K. L. (2006). Geochemical controls on hydrothermal fluids from the Kairei and Edmond Vent Fields, 23°–25°S, Central Indian Ridge. Geochem. Geophys. Geosys. 7. https://doi.org/10.1029/2005GC001067.

Gartman A., Findlay A. J. and Luther, III, G. W. (2014). Nanoparticulate pyrite and other nanoparticles are a widespread component of hydrothermal vent black smoker emissions. Chem. Geol. 366, 32–41. doi: 10.1016/j.chemgeo.2013.12.013.

Gartman, A., Findlay A. J., Hannington, M., Garbe-Schönberg, D., Jamieson, J.W., Kwasnitschka, T. (2019). The role of nanoparticles in mediating element deposition and transport at hydrothermal vents, Geochimica et Cosmochimica Acta, 261, 113-131, doi.org/10.1016/j.gca.2019.06.045.

Gartman, A., and Findlay, A.J. (2020). Impacts of hydrothermal plume processes on oceanic metal cycles and transport. Nature Geoscience 13, 396–402. doi: 10.1038/s41561-020-0579-0.

German C. R., Parson L. M. and Team H. S. (1996). Hydrothermal exploration near the Azores Triple Junction: tectonic control of venting at slow-spreading ridges? Earth. Planet. Sci. Lett. 138(1–4), 93–104.

German C. R., Baker E. T., Mevel C. A., Tamaki K., and the FUJI scientific team (1998). Hydrothermal activity along the south-west Indian ridge. Nature 395, 490–493.

German C. R., Livermore R. A., Baker E. T., Bruguier N. I., Connelly D. P., Cunningham A. P., Morris P., Rouse I. P., Statham P. J., Tyler P. A. (2000). Hydrothermal plumes above the East Scotia Ridge: an isolated high-latitude backarc spreading centre. Earth Planet. Sci. Lett. 184, 241–250.

German, C.R., Colley, S., Palmer, M.R., Khripounoff, A., Klinkhammer, G.P. (2002). Hydrothermal plume-particle fluxes at 13°N on the East Pacific Rise. Deep Sea Res. I 49 (11), 1921–1940. doi: 10.1016/S0967-0637(02)00086-9.

German, C. and Von Damm, K. (2003). Hydrothermal processes. In: Elderfield, H. (ed.), Treatise on Geochemistry: The Oceans and Marine Geochemistry. Elsevier/ Pergamon, Oxford, pp. 181–222.

German, C.R. and Lin, J. (2004). The thermal structure of the oceanic crust, ridge spreading and hydrothermal circulation: How well do we understand their interconnections? in German, C.R., et al. (eds.), Mid-ocean ridges: Hydrothermal interactions between the lithosphere and oceans: American Geophysical Union Geophysical Monograph 148, p. 1–18.

German C.R., Thurnherr A.M., Knoery J., Charlou J.L., Jean-Baptiste P., and Edmonds H.N. (2010). Heat, volume and chemical fluxes from submarine venting: A synthesis of results from the Rainbow hydrothermal field, 36° N MAR. Deep Sea Research Part I: Oceanographic Research Papers 57: 518–527.

German C. R. and Seyfried Jr, W. E. (2014) Hydrothermal Processes. In Treatise on Geochemistry (eds. H. D. Holland and K. K. Turekian), Second Edition. Elsevier, Oxford, pp. 191– 233.

Haymon, R. M., et al. (1993), Volcanic eruption of the mid-ocean ridge along the East Pacific Rise crest at 9°45-52' N: Direct submersible observations of seafloor phenomena associated with an eruption event in April 1991. Earth Planet. Sci. Lett., 119, 85–101.

Hoffman, C. L., Nicholas, S. L., Ohnemus, D. C., Fitzsimmons, J. N., Sherrell, R. M., German, C. R., et al. (2018). Near-field iron and carbon chemistry of nonbuoyant hydrothermal plume particles, southern east pacific rise 15°S. Mar. Chem. 201, 183–197. doi: 10.1016/j.marchem.2018.01.011.

Horning, G., Sohn, R. A., Canales, J. P. and Dunn, R. A. (2018). Local seismicity of the Rainbow massif on the Mid-Atlantic Ridge. Journal of Geophysical Research: Solid Earth, 123, 1615–1630. https://doi. org/10.1002/2017JB015288.

Huerta- Diaz, M.A., Morse, J.W. (1992). Pyritization of trace metals in anoxic marine sediments. Geochim. Cosmochim. Acta 56, 2681–2702.

Janecky, D. R., and Seyfded Jr., W. E. (1984). Formation of massive sulfide deposits on oceanic ridge crests: Incremental reaction models for mixing between hydrothermal solutions and seawater, Geochim. Cosmochim. Acta, 48, 2723-2738.

Janecky, D.R., and Seyfried Jr., W.E. (1986). Hydrothermal serpentinization of peridotite within the oceanic crust: experimental investigations of mineralogy and major element chemistry. Geochim. Cosmochim. Acta 50, 1357 – 1378.

James, R. H., Elderfield, H., Palmer, M. R. (1995). The chemistry of hydrothermal fluids from the Broken Spur site, 29°N Mid Atlantic Ridge. Geochim. Cosmochim. Acta, 59, 651–659. doi: 10.1016/0016-7037(95)00003-I.

Janecky, D.R., and Seyfried, W.E. (1986). Hydrothermal serpentinization of peridotite within the oceanic crust: Experimental investigations of mineralogy and major element chemistry. Geochimica et Cosmochimica Acta 50, 1357-1378. doi: 10.1016/0016-7037(86)90311-X.

Jean-Baptiste, P., J. L. Charlou, M. Stievenard, J. P. Donval, H. Bougault, and C. Mével (1991). Helium and methane measurements in hydrothermal fluids from the mid-Atlantic ridge: The Snake Pit at 23°N, Earth Planet. Sci. Lett., 106, 17–28.

Jean-Baptiste, P., Bougault, H., Vangriesheim, A., Charlou, J. L., Dapoigny, A., Knoery, J., Fouquet, Y., Needham, H. D., and German, C. R. (1998). Mantle

^{3}He in hydrothermal vents and plume of the Lucky Strike site (MAR, 37°17 N) and associated heat flux, Earth Planet. Sci. Lett., 157, 69–77.

Jones, C. E., and Jenkyns, H. C. (2001), Seawater strontium isotopes, oceanic anoxic events, and seafloor hydrothermal activity in the Jurassic and Cretaceous, Am. J. Sci., 301, 112–149.

Karson, A.J. (2002). Geologic Structure of the Uppermost Oceanic Crust Created at Fast- to Intermediate-Rate Spreading Centers. Annual Review of Earth and Planetary Sciences 2002 30:1, 347-384.

Kelley, D. S., et al. (2001). An off-axis hydrothermal field discovered near the Mid-Atlantic Ridge at 30°N, Nature, 412, 145–149.

Kelley, D. S., Baross, J. A. and J. R. Delaney (2002). Volcanoes, fluids, and life in submarine environments, Annu. Rev. Earth Planet. Sci., 30, 385–491.

Kelley, D. S., et al. (2005). A serpentinite-hosted ecosystem: The Lost City hydrothermal field, Science, 307, 1428–1434.

Kelley, D. S., and Shank, T.M. (2010). Hydrothermal systems: A decade of discovery in slow spreading environments, Diversity of Hydrothermal Systems on Slow Spreading Ocean Ridges. In: Rona PA, Devey CW, Dyment J, Murton BJ (eds). Diversity of Hydrothermal Systems on Slow Spreading Ocean Ridges. American Geophysical Union Monograph Series 188, 369-407, Washington, DC: AGU.

Kerr, C.A, (1998). Oceanic plateau formation: a cause of mass extinction and black shale deposition around the Cenomanian–Turonian boundary? Journal of the Geological Society, London, Vol. 155, pp. 619–62.

Kleint, C., Pichler, T., Kochisnky, A. (2017). Geochemical characteristics, speciation and size-fractionation of iron (Fe) in two marine shallow-water hydrothermal systems, Dominica, Lesser Antilles. Chemical Geology, 454, 44-53.

Kleint, C., Bach, W., Diehl, A., Fröhberg, N., Garbe-Schönberg, D., Hartmann, J.F., Ronde, C.E.J., Sander, S. G., Strauss, H., Stucker, V. K., Thal, J., Zitoun, R., Koschinsky, A. (2019). Geochemical characterization of highly diverse hydrothermal fluids from volcanic vent systems of the Kermadec intraoceanic arc, Chemical Geology, 528

Klinkhammer, G.P., Chin, C.S., Keller, R.A., Dahlmann, A., Sahling, H., Sarthou, G., Petersen, S., Smith, F., Wilson, C. (2001). Discovery of new hydrothermal vent sites in Bransfield Strait, Antarctica, Earth and Planetary Science Letters, 193, 3–4 395-407

Konn, C., Charlou, J. L., Donval, J. P., Holm, N. G., Dehairs, F., and Bouillon, S. (2009). Hydrocarbons and oxidized organic compounds in hydrothermal fluids from Rainbow and Lost City ultramafic-hosted vents, Chem. Geol., 258, 299–314.

Koschinsky, A., Schmidt, K., Garbe-Schönberg, D. (2020). Geochemical time series of hydrothermal fluids from the slow-spreading Mid-Atlantic Ridge: Implications of medium-term stability. Chemical Geology, 552,119760.

Lambert, F., Tagliabue, A., Shaffer, G., Lamy, F., Winckler, G., Farias, L., Gallardo, L., and De Pol-Holz, R. (2015). Dust fluxes and iron fertilization in Holocene and Last Glacial Maximum climates, Geophys. Res. Lett., 42, 6014–6023.

Langmuir, C. H., et al. (1993). Geological setting and characteristics of the Lucky Strike vent field at 37°17 N on the Mid-Atlantic Ridge (abstract), Eos Trans. AGU, 74, 99.

Lang S., Butterfield D., Schulte M., Kelley D. and Lilley M. (2010). Elevated concentrations of formate, acetate and dissolved organic carbon found at the Lost City hydrothermal field. Geochim. Cosmochim. Acta 74, 941–952.

Lang S. Q., Fruh-Green G. L., Bernasconi S. M., Lilley M. D., Proskurowski G., Mehay S. and Butterfield D. A. (2012). Microbial utilization of abiogenic carbon and hydrogen in a serpentinite-hosted system. Geochim. Cosmochim. Acta 92, 82– 99.

Larson, R.L. 1991. Latest pulse of Earth: Evidence for a mid-Cretaceous superplume. Geology, 19, 963–966.

Lartaud F. et al. (2010). Fossil clams from a serpentinite-hosted sedimented vent field near the active smoker complex Rainbow (MAR, 26°13N): insight into the biogeography of vent fauna. Geochem Geophys Geosyst 11: Q0AE01.

Lartaud, F., Little, C. T. S., de Rafelis, M., Bayon, G., Dyment, J., Ildefonse, B., et al. (2011). Fossil evidence for serpentinization fluids fueling chemosynthetic assemblages. Proc. Natl. Acad. Sci. U.S.A. 108, 7698–7703. doi: 10.1073/pnas. 1009383108.

Le Bris, N., Duperron, S. (2010). Chemosynthetic Communities and Biogeochemical Energy Pathways Along the Mid-Atlantic Ridge: The case of Bathymodiolusazoricus. In: Diversity of Hydrothermal Systems on Slow Spreading Ocean Ridges, Geophysica, American Geophysical Union, pp. 409–429.

Le Bris N. and the Science Party. (2018). Campagne TRANSECT TRANsfert d'Energie dans les 720 Ecosystèmes Chimiosynthétiques en contexte ulTramafique. doi.org/10.17600/18000513.

Le Bris N., Yücel M., Das A., Sievert S.M., LokaBharathi P., Girguis P.R. (2019). Hydrothermal Energy Transfer and Organic Carbon Production at the Deep Seafloor. Front. Mar. Sci. 5:531. doi: 10.3389/fmars.2018.00531.

Leckie, R. M., Bralower, T. J., and Cashman R. (2002). Oceanic anoxic events and plankton evolution: Biotic response to tectonic forcing during the mid-Cretaceous, Paleoceanography, 17(3), 1041.

Lough, A.J.M., Homoky, W.B., Connelly, D.P., Comer-Warner, S.A., Nakamura, K., Abyaneh, M.K., Kaulich, B., Mills, R.A. (2019). Soluble iron conservation and colloidal iron dynamics in a hydrothermal plume, Chemical Geology, 511, 225-237, doi.org/10.1016/j.chemgeo.2019.01.001.

Ludwig, K. A., Shen, C. C., Kelley, D. S., Cheng, H. and Edwards, R. L. (2011). U-Th systematics and 230Th ages of carbonate chimneys at the Lost City Hydrothermal Field, Geochim. Cosmochim. Acta, 75(7), 1869–1888, doi:10.1016/j.g ca.2011.01.008.

Lund, D. C., and Asimow, P. D. (2011). Does sea level influence mid-ocean ridge magmatism on Milankovitch timescales? Geochemistry, Geophysics, Geosystems, 12, Q12009. doi.org/10.1029/2011GC003693.

Lund, D.C., Asimow, P.D., Farley, K.A., Rooney, T.O., Seeley, E., Jackson, E.W., Durham, Z.M. (2016). Enhanced East Pacific Rise hydrothermal activity during the last two glacial terminations. Science 80 (351), 478–482.

Lupton, J.E. and Craig, H. (1983). A major ^{3}He source on the East Pacific Rise. Science, 214, 13- 18.

Lupton, J. E., Baker, E. T., Massoth, G. J., Thomson, R. E., Burd, B. J., Butterfield, D. A., Embley, R. W. and Cannon, G. A. (1995). Variation in water-column ^{3}He/heat ratios associated with the 1993 CoAxial event, Juan de Fuca Ridge. Geophys. Res. Lett. 22, 155-158.

Macdonald, K.C. (1982). Mid-Ocean Ridges: Fine Scale Tectonic, Volcanic and Hydrothermal Processes Within the Plate Boundary Zone. Annual Review of Earth and Planetary Sciences 1982 10:1, 155-190.

Martinez-Garcia, A., Sigman, D. M., Ren, H., Anderson, R. F., Straub, M., Hodell, D. A., Jaccard, S. L., Eglinton, T. I., and Haug, G. H. (2014). Iron Fertilization of the Subantarctic Ocean During the Last Ice Age, Science, 343, 1347–1350.

McCaig, A. M., Cliff, R. A., Escartin, J., Fallick, A. E., MacLeod, C. J. (2007). Oceanic detachment faults focus very large volumes of black smoker fluids. Geology 35 (10): 935–938. doi: https://doi.org/10.1130/G23657A.1.

McCollom, T.M. and Bach, W. (2009). Thermodynamic constraints on hydrogen generation during serpentinization of ultramafic rocks. Geochimica et Cosmochimica Acta 73, 856–875.

McCollom, TM., Seewald, J.S. (2013). Serpentinites, hydrogen, and life, Elements 9,129–134.

McDermott, J. M., Sylva, S. P., Ono, S., German, C. R., Seewald, S. (2018). Geochemistry of fluids from Earth's deepest ridge-crest hot-springs: Piccard

hydrothermal field, Mid-Cayman Rise. Geochim. Cosmochim. Acta 228, 95–118.

McDermott, J.M., Sylva, S.P., Ono, S., German, C.R., Seewald, J.S. (2020). Abiotic redox reactions in hydrothermal mixing zones: decreased energy availability for the subsurface biosphere. PNAS 117, 20453–20461. doi.org/10.1073/pnas.2003108117.

McDonough, W. F., and Sun, S.S. (1995). The composition of the Earth, Chem. Geol., 120, 223 – 253.

Metz, S., and Trefry, J.H. (2000). Chemical and mineralogical influences on concentrations of trace metals in hydrothermal fluids, Geochimica et Cosmochimica Acta, 64, 13, 2267-2279, doi.org/10.1016/S0016-7037(00)00354-9.

Middleton, J.L., Langmuir, C.H., Mukhopadhyay, S., McManus, J.F., Mitrovica, J.X., (2016). Hydrothermal iron flux variability following rapid sea level changes. Geophys. Res. Lett. 43, 1–9.

Mitchell, N.C., Allerton, S., Escarting, J. (1998). Sedimentation on young ocean floor at the Mid-Atlantic Ridge, 29 °N, Marine Geology, 148, 1–2, 1-8. doi.org/10.1016/S0025-3227(98)00018-8

Moore E.K. et al. (2017). Metal availability and the expanding network of microbial metabolisms in the 664 Archaean eon, Nature Geoscience 10, 629–636.

Mottl, M.J. and Holland, H.D. (1978). Chemical exchange during hydrothermal alteration of basalt by seawater - I. Experimental results for major and minor

components of seawater. Geochimica et Cosmochimica Acta 42, 1103-1115. doi: 10.1016/0016-7037(78)90107-2.

Mottl M. J. and McConachy T. F. (1990). Chemical processes in buoyant hydrothermal plumes on the East Pacific Rise near 21°N. Geochim. Cosmochim. Acta 54, 1911–1927. doi: 10.1016/0016-7037(90)90261-I.

Murton, B. J., et al. (1994). Direct evidence for the distribution and occurrence of hydrothermal activity between 27°N–30°N on the Mid-Atlantic Ridge, Earth Planet. Sci. Lett., 125, 119–128.

Murton, B.J., Van Dover C., Southward, E. (1995). Geological setting and ecology of the Broken Spur hydrothermal vent field: 29°10′N on the Mid-Atlantic Ridge. Geological Society, London, Special Publications, 87, 33-41. doi: 10.1144/GSL.SP.1995.087.01.04.

Orth, C.J., Attrep Jr, M., Quintana, L.R., Elder, W.P., Kauffman, E.G., Diner, R., and Villamil T. (1993). Elemental abundance anomalies in the late Cenomanian extinction interval: a search for the source(s). Earth and Planetary Science Letters, 117, 189–204.

Ottolini L., Le Fevre B., and Vanucci R. (2004). Direct assessment of mantle boron and lithium contents and distribution by SIMS analyses of peridotite minerals. Earth Planet. Sci. Lett. 228, 19– 36.

Pedersen R.B., Rapp H.T., Thorseth I.H. et al. (2010). Discovery of a black smoker vent field and vent fauna at the Arctic Mid-Ocean Ridge. Nature Communications 1: doi.org/10.1038/ncomms1124.

Reeves E.P., Seewald J.S., Saccocia P., et al. (2011). Geochemistry of hydrothermal fluids from the PACMANUS, Northeast Pual and Vienna Woods hydrothermal fields, Manus Basin, Papua New Guinea. Geochimica et Cosmochimica Acta 75: 1088–1123.

Pester N. J., Rough M., Ding K. and Seyfried, Jr., W. E. (2011). A new Fe/Mn geothermometer for hydrothermal systems: Implications for high-salinity fluids at 13°N on the East Pacific Rise. Geochim. Cosmochim. Acta 75, 7881–7892.

Pester, N. J., Reeves, E. P., Rough, M. E., Ding, K., Seewald, J. S., and Seyfried Jr., W. E. (2012). Subseafloor phase equilibria in high-temperature hydrothermal fluids of the Lucky Strike Seamount (Mid-Atlantic Ridge, 37°17′N). Geochimica et Cosmochimica Acta, 90, 303–322, doi:10.1016/j.gca.2012.05.018.

Prokurowski, G., Lilley, M. D., Kelley, D. S. and Olson, E. J. (2006). Low temperature volatile production at the Lost City Hydrothermal field, evidence from a hydrogen stable isotope geothermometer, Chem. Geol., 229, 331–343.

Proskurowski, G., Lilley, M. D., Olson, E. J., Früh-Green, G. L., Lupton, J. E., Seewald, J. S., Sylva, S. P., and Kelley, D. S. (2008). Abiogenic hydrocarbon production at Lost City hydrothermal field, Science, 319, 604–607.

Petersen, S., K. Kuhn, T. Kuhn, N. Augusting, R. Hekinian, L. Franz, and C. Borowski (2009), The geological setting of the ultramafic-hosted Logatchev hydrothermal field (14°45′N, Mid-Atlantic Ridge) and its influence on massive sulfide formation, Lithos, 112, 40–56.

Reed, M.H. and Palandri, J. (2006). Sulfide mineral precipitation from hydrothermal fluids. Rev. Mineral. Geochem. 61, 609–631.

Reeves E. P., Seewald J. S., Saccocia P., Bach W., Craddock P. R., Shanks, III, W. C., Sylva S. P., Walsh E., Pichler T. and Rosner M. (2011). Geochemistry of hydrothermal fluids from the PACMANUS, Northeast Pual and Vienna Woods hydrothermal fields, Manus Basin, Papua New Guinea. Geochim. Cosmochim. Acta 75, 1088–1123.

Resing, J. A., Sedwick, P. N., German, C. R., Jenkins, W. J., Moffett, J. W., Sohst, B. M., et al. (2015). Basin-scale transport of hydrothermal dissolved metals across the south Pacific Ocean. Nature 523, 200–203. doi: 10.1038/nature14577.

Rickaby R.E.M. (2015). Goldilocks and the three inorganic equilibria: how Earth's chemistry and life coevolve to be nearly in tune. Phil Trans R Soc A 373: 20140188.

Rogers AD, Tyler PA, Connelly DP, et al. (2012). The discovery of new deep-sea hydrothermal vent communities in the Southern Ocean and implications for biogeography. PLoS Biology 10: e1001234.

Rona, P. A., Klinkhammer, G., Nelsen, T. A., Trefry, J. H. and Elderfield, H. (1986). Black smokers, massive sulfides, and vent biota at the Mid-Atlantic Ridge, Nature 321, 33–37.

Rubin, K. H., Macdougall, J. D. and Perfit, M. R. (1994). ^{210}Po-^{210}Pb dating of recent volcanic eruptions on the sea floor, Nature, 368, 841– 844, doi:10.1038/368841a0.

Rudnicki M. D. and Elderfield H. (1993). A chemical model of the buoyant and neutrally buoyant plume above the TAG vent field, 26 degrees N, Mid-Atlantic Ridge. Geochim. Cosmochim. Acta 57, 2939–2957. doi: 10.1016/0016-7037(93)90285-5.

Sander S.G., and Koschinsky A. (2011). Metal flux from hydrothermal vents increased by organic complexation, Nature Geoscience 4: 45-150.

Sands, C.M., Connelly, D.P., Statham, P.J., German, C.R. (2012). Size fractionation of trace metals in the Edmond hydrothermal plume, Central Indian Ocean, Earth and Planetary Science Letters, 319–320, 15-22, doi.org/10.1016/j.epsl.2011.12.031.

Schine, C.M.S., Alderkamp, AC., van Dijken, G. et al. (2021). Massive Southern Ocean phytoplankton bloom fed by iron of possible hydrothermal origin. Nat Commun 12, 1211 doi.org/10.1038/s41467-021-21339-5.

Schmidt, K., Koschinsky, A., Garbe-Schönberg, D., de Carvalho, L.M., Seifert, R. (2007). Geochemistry of hydrothermal fluids from the ultramafic-hosted Logatchev hydrothermal field, 15°N on the Mid-Atlantic Ridge: Temporal and spatial investigation. Chem. Geol., 242, 1–21. doi: 10.1016/j.chemgeo.2007.01.023.

Schlitzer R, eGEOTRACES- Electronic Atlas of GEOTRACES Sections and Animated 3D Scenes, http://www.egeotraces.org, 2017.

Seewald J. S. and Seyfried, Jr., W. E. (1990). The effect of temperature on metal mobility in subseafloor hydrothermal systems: constraints from basalt alteration experiments. Earth Planet. Sci. Lett. 101, 388–403.

Seewald J. S., Doherty K. W., Hammar T. R. and Liberatore S. P. (2002). A new gas-tight isobaric sampler for hydrothermal fluids. Deep Sea Res. I: Oceanographic Res. Papers 49, 189–196.

Seewald, J.S., Reeves, E.P., Bach, W., Saccocia, P.J., Craddock, P.R., Shanks, W. C., Sylva, S.P., Pichler, T., Rosner, M., Walsh, E. (2015). Submarine venting of magmatic volatiles in the Eastern Manus Basin, Papua New Guinea, Geochimica et Cosmochimica Acta, 163,178-199, doi.org/10.1016/j.gca.2015.04.023.

Seewald, J. S., Reeves, E. P., Bach, W., Saccocia, P. J., Craddock, P. R., Walsh, E., Shanks, W. C., Sylva, S. P., Pichler, T., Rosner, M. (2019). Geochemistry of hot-springs at the SuSu Knolls hydrothermal field, Eastern Manus Basin: Advanced argillic alteration and vent fluid acidity. Geochim. Cosmochim. Acta 255, 25–48. doi.org/10.1016/j.gca.2019.03.034 0016-7037.

Seyfried JR, W.E., and Bischoff, J. (1981). Experimental seawater-basalt interaction at 300°C, 500 bars, chemical exchange, secondary mineral formation and implications for the transport of heavy metals. Geochimica et Cosmochimica Acta 45, 135-147. doi: 10.1016/0016-7037(81)90157-5.

Seyfried, Jr., W. E., Janecky D. R. and Mottl M. J. (1984). Alteration of the oceanic crust: implications for geochemical cycles of lithium and boron. Geochim. Cosmochim. Acta 48, 557–569.

Seyfried W. E. Jr. and Ding K. (1993). The effect of redox on the relative solubilities of copper and iron in Cl-bearing aqueous fluids at elevated temperatures and pressures: An experimental study with application to subseafloor hydrothermal systems. Geochim. Cosmochim. Acta 57, 1905–1917.

Seyfried W. E. Jr. and Ding K. (1995). Phase equilibria in subseafloor hydrothermal systems: A review of the role of redox, temperature, pH and dissolved Cl on the chemistry of hot spring fluids at midocean ridges. In Seafloor Hydrothermal Systems (ed. S. E. Humphris et al.), Geophysical Monograph 91, 248–272. American Geophysical Union.

Seyfried, W.E., Chen, X., Chan, L.H. (1998). Trace Element Mobility and Lithium Isotope Exchange During Hydrothermal Alteration of Seafloor Weathered Basalt: An Experimental Study at 350°C, 500 Bars, Geochimica et Cosmochimica Acta, 62, 6,949-960.

Seyfried JR, W.E., Foustoukos, D.I., Fu, Q. (2007). Redox evolution and mass transfer during serpentinization: An experimental and theoretical study at 200°C, 500 bars with implications for ultramafic-hosted hydrothermal systems at Mid-Ocean Ridges. Geochimica et Cosmochimica Acta 71, 3872-3886. doi: 10.1016/j.gca.2007.05.015.

Seyfried, W.E., Pester, N.J., Ding, K., Rough, M. (2011). Vent fluid chemistry of the Rainbow hydrothermal system (36°N, MAR): phase equilibria and in situ pH controls on subseafloor alteration processes. Geochim. Cosmochim. Acta 75, 1574–1593. doi: 10.1016/j.gca.2011.01.001.

Seyfried, W.E., Pester, N. J., Tutolo, B. M., Ding, K. (2015). The Lost City hydrothermal system: Constraints imposed by vent fluid chemistry and reaction path models on subseafloor heat and mass transfer processes. Geochimica et Cosmochimica Acta, 163, 59-79, doi.org/10.1016/j.gca.2015.04.040.

Sharp Z. D. and Barnes J. D. (2004) Water-soluble chlorides in massive sea-floor serpentinites: a source of chloride in subduction zones. Earth Planet. Sci. Lett. 226, 243–254.

Sigman, D. M. and Boyle, E. A. (2000). Glacial/interglacial variations in atmospheric carbon dioxide. Nature 407, 859–869.

Sigman, D. M., Hain, M.P., and Haug, G.H. (2010). The polar ocean and glacial cycles in atmospheric CO2 concentration. Nature 466, 47-55.

Sinton, J. M., and Detrick, R. S. (1992). Mid-ocean ridge magma chambers, J. Geophys. Res., 97, 197–216.

Sinton, C. W., and Duncan R. A. (1997). Potential links between ocean plateau volcanism and global ocean anoxia at the Cenomanian-Turonian boundary, Econ. Geol., 92, 836 – 842.

Stookey, L. L. (1970). Ferrozine-a new spectrophotometric reagent for iron. Anal. Chem. 42, 779-781. doi: 10.1021/ac60289a016.

Tao C., Lin J., Guo S.h, et al. (2012). First active hydrothermal vents on an ultraslow spreading center: SouthWest Indian Ridge. Geology 40(1): 47–50.

Tivey, K.M. (2007). Generation of Seafloor Hydrothermal Vent Fluids and Associated Mineral Deposits, Oceanography, Volume 20, Number 1.

Twining, B.S., and S.B. Baines. (2013). The trace metal composition of marine phytoplankton, Annual Review of Marine Science 5: 191-215.

Tolstoy, M., et al. (2006). A sea-floor spreading event captured by seismometers, Science, 314, 1920–1922, doi:10.1126/ science.1133950.

Tomascak, P. B., Langmuir, C. H., le Roux, P. J. and Shirey, S. B. (2008). Lithium isotopes in global mid-ocean ridge basalts. Geochimica et Cosmochimica Acta 72, 1626–1637.

Trefry, J.H., Butterfield, D.B., Metz, S., Massoth, G.J., Trocine, R.P., Feely, R.A., (1994). Trace metals in hydrothermal solutions from Cleft Segment on the southern Juan de Fuca Ridge. J. Geophys. Res. 99, 4925–4935.

Twitchett, R.J. (2013). Mass Extinctions, Notable Examples of, in: Simon A Levin (ed.), Encyclopedia of Biodiversity (Second Edition), Academic Press, 167-177, doi.org/10.1016/B978-0-12-384719-5.00092-7.

Von Damm, K.L., Edmond, J.M., Grant, B., Measures, C.I., Walden, B., Weiss, R.F. (1985). Chemistry of submarine hydrothermal solutions at 21 °N, East Pacific Rise, Geochimica et Cosmochimica Acta, 49, Issue 11, 2197-2220, doi.org/10.1016/0016-7037(85)90222-4.

Von Damm K. L. and Bischoff J. L. (1987). Chemistry of hydrothermal solutions from the southern Juan de Fuca Ridge. J. Geophys. Res. 92, 11334–11346.

Von Damm, K. L. (1988), Systematics of and postulated controls on submarine hydrothermal solution chemistry, J. Geophys. Res., 93, 4551 – 4561.

Von Damm, K.L. (1990). Seafloor Hydrothermal Activity: Black Smoker Chemistry and Chimneys. Annual Review of Earth and Planetary Sciences,18:1, 173-204.

Von Damm K. L., Bischoff J. and Rosenbauer R. (1991). Quartz solubility in hydrothermal seawater: an experimental study and equation describing quartz solubility for up to 0.5 M NaCl solutions. Am. J. Sci. 291, 977–1007.

Von Damm K. L. (1995). Controls on the chemistry and temporal variability of seafloor hydrothermal fluids. Geophys. Monogr. (AGU) 91, 222–247.

Von Damm, K. L., Bray, A. M., Buttermore, L. G. and Oosting, S. E. (1998). The geochemical controls on vent fluids from the Lucky Strike vent field, Mid-Atlantic Ridge, Earth Planet. Sci. Lett., 160, 521–536.

Von Damm, K.L. (2000). Chemistry of hydrothermal vent fluids from 9 degrees-10 degrees N, East Pacific Rise: "time zero," the immediate posteruptive period. J. Geophys. Res. Earth 105, 11203–11222. doi.org/10.1029/1999jb900414.

Von Damm, K. L. (2004). Evolution of the hydrothermal system at East Pacific Rise, 9^{o} 50'N: geochemical evidence for changes in the upper oceanic crust, in Mid-Ocean Ridges: Hydrothermal Interactions Between the Lithosphere and Oceans, Geophys. Monogr. Ser., 148, In: C. R. German, J. Lin, L. M. Parson (eds.), pp. 285–304, AGU, Washington, D.C., doi:10.1029/148GM12.

Waeles, M., Cotte, L., Pernet-Coudrier, B., Chavagnac, V., Cathalot, C., Leleu, T., et al. (2017). On the early fate of hydrothermal iron at deep-sea vents: a reassessment after in-situ filtration. Geophys. Res. Lett. 1–8. doi: 10.1002/2017GL073315.

Wilson S. C., Murton B. J. and Taylor R. N. (2013). Mantle composition controls the development of an Oceanic Core Complex. Geochem. Geophys. Geosys 14(4), 1–18. doi. org/10.1002/ggge.20046.

Yücel, M., Gartman, A., Chan, C.S., Luther III, G.W. (2011). Hydrothermal vents as a kinetically stable source of iron-sulphide-bearing nanoparticles to the ocean. Nat. Geosci. 4, 367–371. doi: 10.1038/ngeo1148.

Yucel, M., and Luther, G. W. (2013). Temporal trends in vent fluid iron and sulfide chemistry following the 2005/2006 eruption at East Pacific Rise, 9°50N: Fe-S, Geochem. Geophys. Geosyst., 14, 759–765, doi:10.1002/ggge.20088.

Yucel, M., Sevgen, S., Le Bris, N. (2021). Soluble, colloidal and particulate iron across the hydrothermal vent mixing zones in Broken Spur and Rainbow, Mid-Atlantic Ridge. Manuscript submitted for publication.